AD_____

Award Number:
W81XWH-05-1-0129

TITLE:
AUTOLOGOUS MARROW-DERIVED STEM CELL-SEEDED GENE-SUPPLEMENTED COLLAGEN SCAFFOLDS FOR SPINAL CORD REGENERATION AS A TREATMENT FOR PARALYSIS

PRINCIPAL INVESTIGATOR:
Myron Spector, Ph.D.

CONTRACTING ORGANIZATION:
Boston VA Research Institute
Boston, MA 02130

REPORT DATE:
November 2009

TYPE OF REPORT:
Final

PREPARED FOR: U.S. Army Medical Research and Materiel Command
Fort Detrick, Maryland 21702-5012

DISTRIBUTION STATEMENT:

√ Approved for public release; distribution unlimited

REPORT DOCUMENTATION PAGE

Form Approved
OMB No. 0704-0188

1. REPORT DATE *(DD-MM-YYYY)*	2. REPORT TYPE	3. DATES COVERED *(From - To)*
01-NOV-2009	Final	6 DEC 2004 - 31 OCT 2009

4. TITLE AND SUBTITLE

AUTOLOGOUS MARROW-DERIVED STEM CELL-SEEDED GENE-SUPPLEMENTED COLLAGEN SCAFFOLDS FOR SPINAL CORD REGENERATION AS A TREATMENT FOR PARALYSIS

5a. CONTRACT NUMBER
W81XWH-05-1-0129

5b. GRANT NUMBER
PR043168

5c. PROGRAM ELEMENT NUMBER

6. AUTHOR(S)
Myron Spector, Ph.D.

Email: mspector@rics.bwh.harvard.edu

5d. PROJECT NUMBER
W23RYX-4234-N617

5e. TASK NUMBER

5f. WORK UNIT NUMBER

7. PERFORMING ORGANIZATION NAME(S) AND ADDRESS(ES)

Boston VA Research Institute
150 S. Huntington Ave.
Boston, MA 02130

8. PERFORMING ORGANIZATION REPORT NUMBER

9. SPONSORING / MONITORING AGENCY NAME(S) AND ADDRESS(ES)

U.S. Army Medical Research and Materiel Command
Ft. Detrick, MD 21702

10. SPONSOR/MONITOR'S ACRONYM(S)

11. SPONSOR/MONITOR'S REPORT NUMBER(S)

12. DISTRIBUTION / AVAILABILITY STATEMENT

Unlimited

13. SUPPLEMENTARY NOTES

14. ABSTRACT

The long-term objective of this research is to develop a device for treating spinal cord injury. The specific aims of the proposed study are to test new types of collagen biomaterials. Moreover we will be investigating the effects of incorporating genes from nerve growth factors into the collagen scaffolds and seeding the scaffolds with neurogenic cells. The standardized defect site is a 5-mm gap in the rat thoracic spinal cord. Our principal method of evaluation is histomorphometry. During the past project year the following were accomplished, toward achieving the objectives of determining the effects of selected design variables on the reparative processes in spinal cord defects: 1) investigation of nanoparticles, as carriers of genes for neurotrophic factors, to be incorporated into collagen scaffolds for implantation into spinal cord defects; 2) development of an injectable collagen formulation as a carrier for plasmid DNA encoding for neurotrophic factors; 3) formulation of collagen scaffolds containing hyaluronic acid; and 4) investigation of the conditions *in vitro* for the neuro-differentiation of neural stem cells.

15. SUBJECT TERMS

Spinal cord, rat, collagen, tube, regeneration, axons

16. SECURITY CLASSIFICATION OF:			17. LIMITATION OF ABSTRACT	18. NUMBER OF PAGES	19a. NAME OF RESPONSIBLE PERSON
a. REPORT	b. ABSTRACT	c. THIS PAGE			USAMRMC
U	U	U	UU	81	19b. TELEPHONE NUMBER *(include area code)*

Table of Contents

Page

I. INTRODUCTION

The long-term objective of this research is to develop a device for treating spinal cord injury. The specific aims of the proposed study are to test new types of collagen tubes and porous collagen scaffolds. Moreover we will be investigating the effects of incorporating genes from nerve growth factors into the collagen scaffolds and seeding the scaffolds with marrow-derived mesenchymal stem cells. The standardized defect site is a 5-mm gap in the rat thoracic spinal cord. Our principal method of evaluation is histomorphometry.

Our supposition is that an appropriate synthetic substrate (*i.e.*, the collagen scaffold) will mimic or perhaps improve upon the documented ability of peripheral nerve grafts to promote the regrowth of injured spinal axons, and that the seeded stem cells will differentiate under the influence of the endogenous regulators to a support cell phenotype. Collagen-based materials are the bio-inspired biomaterials being used for the fabrication of the tube, covering film and porous scaffold.

The Technical Objectives (TOs) of this project were to investigate the effects of the following critical design variables on regeneration of the spinal cord in a rat model.

1) Degradation rate of a collagen tube.
2) Use of a collagen covering material to wrap around the ends of the stumps at the ends of a segmental defect in the spinal cord rather than insertion of the stumps into a tube.
3) Use of a chondroitin sulfate containing porous collagen scaffold within the tube or wrap.
4) Degradation rate of the porous collagen-GAG scaffold.
5) Pore diameter of the porous collagen-GAG scaffold.
6) Gene supplementation of the porous collagen-GAG scaffold.
7) Seeding of the porous collagen-GAG scaffold with undifferentiated marrow-derived mesenchymal stem cells (MSCs).
8) Seeding of the porous collagen-GAG scaffold with differentiated marrow-derived mesenchymal stem cells.
9) Seeding of the porous collagen-GAG scaffold with marrow-derived mesenchymal stem cells with have undergone gene transfer *ex vivo*.

II. BODY

The work accomplished related to the TOs addressed the following:

A) the fabrication of the devices (related to TOs 1, 3, 4-6);
B) the growth, differentiation and gene transfection of stem cells in vitro (related to TOs 7-9); and
C) the evaluation of select devices in a rat model (related to TOs 2, 3 and 5).

A. Collagen Device Fabrication

The following collagen-based devices were fabricated in the course of :

- collagen tubes
- porous cylindrical collagen scaffolds with axially oriented pores [1]
- porous collagen scaffolds containing hyaluronic acid [2,3]
- injectable collagen gels

In order to achieve TO 1, it was necessary to fabricate collagen tubes. The method for doing so was described in the 1st Annual Report. When the animal experiment related to TO 2 was initiated, it became clear that the stumps of the spinal cord were being damaged during the

procedure of inserting them into a collagen tube. Therefore, a method was employed in the tube was split longitudinally so that it could be applied as a cuff over the defect and the bordering spinal cord stumps. TOs 3, 4, and 5 required the fabrication of cylinders of porous collagen scaffolds, with axially oriented pores. This achievement is described in a reprint in the Appendix [1]. These 3 TOs also required to incorporation of a glycosaminoglycan (GAG) into the collagen scaffolds. While we had previously employed chondroitin sulfate for this purpose concerns became clear regarding the potential neural inhibitory effects of this GAG. Therefore, we incorporated hyaluronic acid, instead of chondroitin sulfate, into the porous collagen scaffold as described in 2 papers in the Appendix [2,3]. The results of the animal implantations revealed that the implantation of pre-formed collagen devices may not be able to adequately fill the segmental defect, and that the segmental defect itself may be too severe a model in which to evaluate the efficacy of the collagen devices. At the same time it became clear that it would be possible to develop an injectable form of the collagen scaffold, which would have the potential to more completely fill the segmental defect and would enable the treatment of the much more common spinal cord defect resulting from contusion. The achievements in developing the injectable form of collagen scaffold, accomplished since the last Annual Report, are described below.

Experiments were conducted with a commercially available soluble type I collagen (Col) from rat tail (BD Biosciences, San Jose, CA) and soluble porcine dermal type I Col prepared as a medical grade product (obtained from Geistlich Pharma, Wolhusen, Switzerland). The advantage of the Geistlich soluble collagen is that it has been approved in some European countries (as a carrier for an antimicrobial agent, Taurolin). While it is not yet approved by FDA for any application, the fact that it has been used for human implantation should facilitate its approval for human trials should the animal work be successful. . A critical feature of the Col gel that we are employing is its ability to undergo cross-linking *in vivo* once it has conformed to the cavity into which it has been injected, thus resulting in a stronger, stiffer, and longer-lasting gel; the novel cross-linking agent is genipin (Gen). Gen is a naturally occurring iridoid compound which reacts with primary amines in Col to produce intrahelical, interhelical, and intermicrofibrilliar cross-links [4]. Gen is 3000-fold less cytotoxic than glutaraldehyde [5]. Gen has thus been proposed as a replacement for glutaraldehyde for the fixation of tissues for human implantation [6,7]. Of note are recent studies which suggest that cells may be able to survive in the presence of Gen cross-linking of Col. Gen also has been reported to have anti-inflammatory, neurogenic, and neuroprotective properties, which make it ideal for our use [8-11]. Also of value is that Gen cross-linked Col becomes blue and fluoresces at 630 nm [12]. This fluorescence is correlated to its mechanical properties, allowing for *in situ* measurements of its stiffness, extent of cross-linking, and degradation [12]. This fluorescence provides a convenient tool for following the cross-linking and degradation of Gen cross-linked Col gels.

The goals of our preliminary studies were to acquire experience in the preparation of the Col gels without and with Gen cross-linking and to compare the rat and porcine products to serve as a foundation for the use of the medical grade porcine Col in our future work. In brief, the respective rat and porcine Col solutions containing various amounts of Gen were added to a 96-well plate and incubated at 37°C. The fluorescence of the gels was measured using 590 nm excitation and 630 nm emission filters. The fluorescence of the Gen-containing gels was normalized by subtracting the baseline auto-fluorescence of Col without Gen.

The addition of Gen to solutions of soluble Col resulted in solid, non-flowing gels by 30 min. as compared to 1-2 hours in non-cross-linked gels. When cross-linked with Gen, collagen gels appeared blue/purple in color. This color deepened with cross-linking time. The

absorbance of the gels at 595 nm showed that the degree of color change was almost linearly proportional to the concentration of Gen contained within the gels (Fig. 1). In the early gelation regime, approximately 6 hours for all gels, the gels experienced an exponential increase in fluorescence (Fig. 2). The amount of Gen contained within the gels was proportional to both the rate and amount of total cross-linking as defined by the measured fluorescence. In the intermediate regime, 6-24 hours, the gels underwent a more linear increase in fluorescence (Fig. 3). The amount of Gen still correlated to an increased rate and total amount of cross-linking but to a lesser extent than at earlier times. For lower concentrations of Gen, this linear regime was extended significantly in time and continued past 80 hours for the lowest concentration of Gen tested. Therefore, the timeframe of this regime was inversely proportional to the amount of Gen contained within the solution. In the late stage (saturation) regime, the increase in fluorescence reached a plateau value (Fig. 4). As expected, this regime occurred much earlier in gels containing a higher level of Gen (~24 hours for 1mM, longer for lower Gen). The final value of fluorescence in the plateau was inversely proportional to the amount of Gen contained within the solution. This suggested a different cross-linking process dependent on Gen concentration.

Direct comparison of the rat tail and porcine soluble Col gels demonstrated that the rat tail Col cross-linked faster, and displayed higher fluorescence than porcine collagen gels (Fig. 5), likely due to the presence of telopeptide regions between the collagen triple helixes. These amine rich regions help to form self-assembled collagen fibrils and provide linking spots for Gen. The porcine collagen had fewer primary amine residues due to the removal of the atelopepitde regions. The difference in the gelation and cross-linking behavior of the rat and porcine Col gels, however, was not so great as to override the advantage of the medical grade quality of the porcine material, and for this reason it will be used in the proposed work.

Of importance is that we demonstrated *in vitro* that Col solutions were capable of undergoing gelation if injected directly to a liquid medium. Additionally, Gen diffusion into the medium was slow enough so that a significant amount of Gen was retained within the gel to provide significant cross-linking. In one experiment (Fig. 6), Col gels were divided into 3 groups: 1) direct plating into a 96-well plate with no phosphate buffered saline (PBS); 2) direct injection into PBS with the gel allowed to solidify and remain in the PBS; and 3) direct injection into PBS and then removal and replacement of PBS after 1hr. At the designated time point the media of the 3 gels were removed and the fluorescence was measured. After removal, the fluorescence intensity continued to be monitored for all gels until the completion of the experiment. When injected directly into PBS, Gen leached out of the gel into the surrounding medium. If the medium was left to incubate the gel, the intensity continued to rise to approximately the same level as Col not injected into PBS, but over a longer time course. However, if the PBS was removed and replaced at 1 hr, the fluorescence intensity essentially came to a halt at whatever level was reached within the one hour. The importance of this experiment is that when injected into tissue, enough Gen will remain within the gelling solution to provide substantial cross-linking *in vivo.*

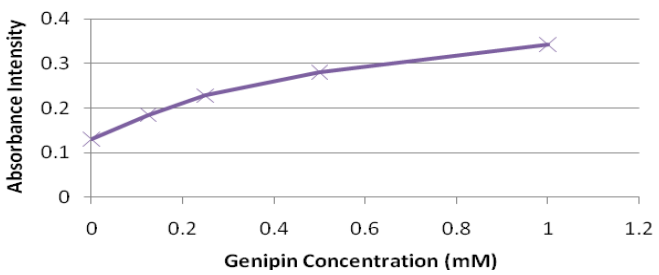

Fig. 1. 2 mg/ml porcine Col. Absorbance at 595 nm, 70 hrs post-gelation.

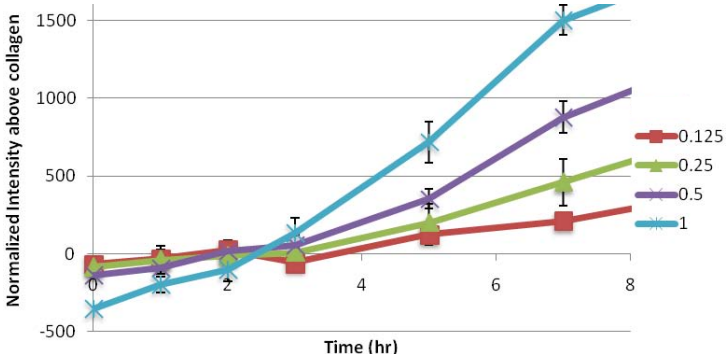

Fig. 2. 2 mg/ml porcine Col. "Early" regime of Gen cross-linking. n=8. Gen conc. in mM.

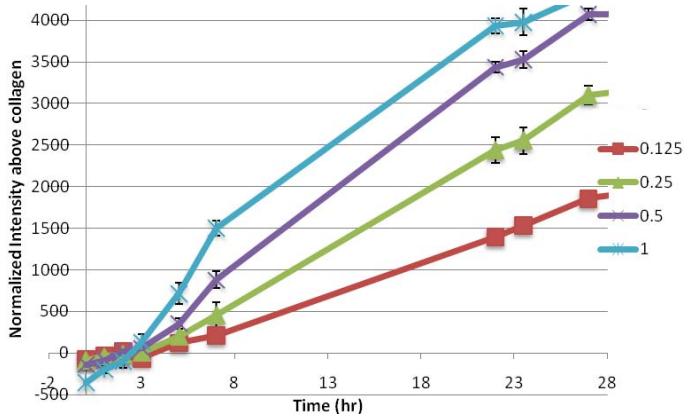

Fig. 3. 2 mg/ml porcine Col. Linear ("intermediate") regime of Gen cross-linking. n=8. Gen conc. in mM.

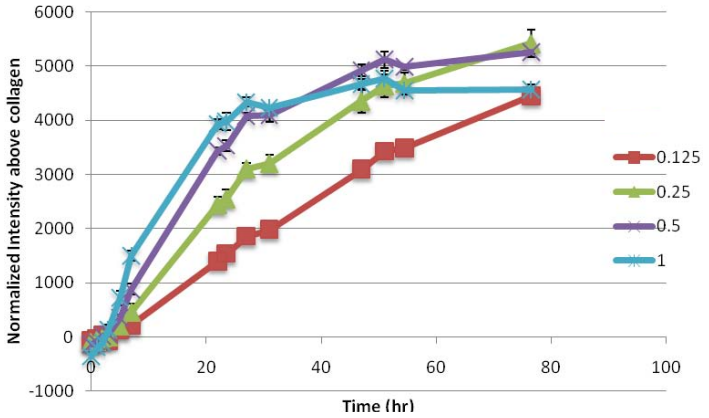

Fig. 4. 2 mg/ml porcine Col. "Late" (saturation) regime of Gen cross-linking. .n=8.

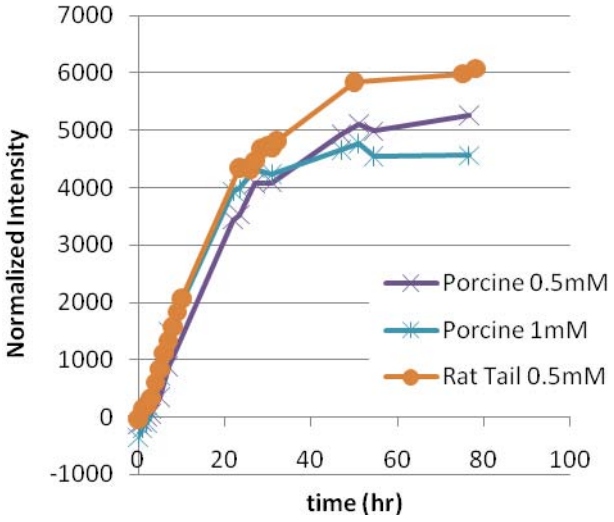

Fig. 5. 2 mg/ml rat tail and porcine Col. Comparison of cross-linking kinetics for porcine and rat-tail Col gels with Gen conc. of 0.5 and 1 mM.

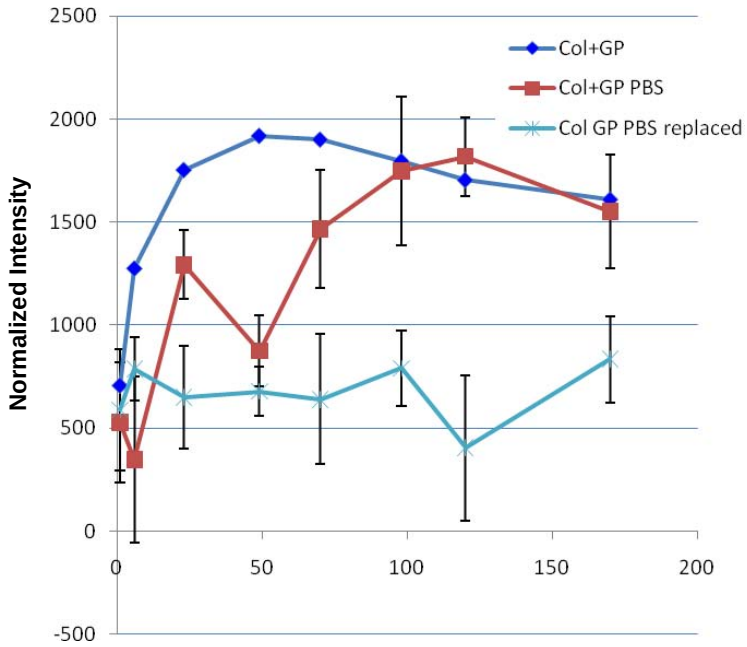

Fig. 6. Aqueous gelation of Col solutions containing Gen (GP). n=8.

B. Stem Cell Growth and Differentiation

TOs 6-9 dealt with the growth, differentiation and gene transfection of stem cells *in vitro*, in preparation for their ultimate implantation in spinal cord defects. The prior Annual Reports described our progress in the: a) implementation of methods for the isolation and growth of marrow-derived MSCs, and differentiation *in vitro*; b) non-viral transfection of undifferentiated MSCs in monolayer and collagen scaffolds, with plasmid DNA encoding a neurotrophic factor; and investigation of nanoparticles [13-15] (see Appendix), as carriers of genes for neurotrophic factors, to be incorporated into collagen scaffolds for implantation into spinal cord defects.

Since the last Annual report we have also performed studies to incorporate neural stem cells into our injectable collagen scaffolds. NSCs (from Fred Gage [16]) were seeded into Col gels prepared from soluble rat tail tendon Col (BD Biosciences), which was neutralized and diluted to 0.5mg/ml. NSCs (from P17 – 20) were added to the pre-gel solutions to a final cell density of 8 million cells per ml. The solution was incubated at 37^{o}C to promote thermal gelation of the Col. After 2 hours, DMEM (supplemented with 20ng/ml FGF2) was added, and the cell-seeded construct was cultured overnight to allow sufficient time for cytotoxic effects to be revealed, using a live-dead cell assay. The results (Fig. 7) demonstrated that more than 95% of the cells were viable.

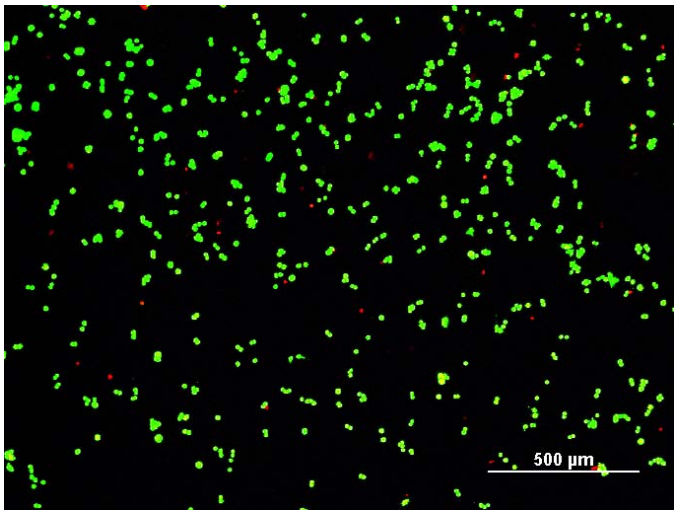

Fig. 7 Greater than 95% cell viability was found in a live (green)-dead (red) cell assay of NSCs seeded in a Col gel.

We are currently engaged in experiments to differentiate the NSCs into neural cells in the Col gel, and to determine if the cells can survive in Col gels undergoing Gen cross-linking.

C. Implantation of Devices in a Rat Model

Table 1 shows the animal studies that were completed. The various aspects of the animal model, including the rationale for the strain or rat which was employed, were described in the Annual Reports. A commercially available absorbable collagen membrane (BioGide, Geistlich Biomaterials, Wolhusen, Switzerland) was used for covering membrane and wrap. Rats in Groups 1 through 11 were sacrificed 6 weeks after injury. Rats in Groups 12 through 15 were sacrificed 2 weeks after injury. In groups 12 through 15, the spinal canal surrounding the defect area was decalcified and sectioned without removal of the spinal cord.

Table 1. Summary of the Animal Studies
(5-mm thoracic spinal cord gap injury in all groups)

Group #	IMPLANT	n*
1	Control: Injury w/o implant (Sprague-Dawley rats)	8
2	Dorsal barrier (covering membrane) alone (Sprague-Dawley)	7
3	Wrap w/o covering membrane (Sprague-Dawley)	4
4	Tube split on top w/o covering membrane (Lewis rats)	7
5	Tube split on bottom AND covering membrane (Lewis)	8
6	Control: Injury w/o implant (Lewis)	3
7	Tube split on top AND covering membrane (Lewis)	8
8	2% collagen cylindrical scaffold freeze dried at -40°C and DHT crosslinked 24 hrs at 105 °C (3 mm diameter; 5 mm long; pre-wet with PBS) + partial wrap (over top only) + covering membrane	8
9	Control: Injury + covering membrane	7
10	2% collagen cylindrical scaffold freeze dried at -40°C and DHT crosslinked 24 hrs at 105 °C (3 mm diameter; 5 mm long; pre-wet with PBS) seeded with 1 million adult neural stem cells (from Fred Gage) + partial wrap (over top only) + covering membrane	8
11	2% collagen cylindrical scaffold freeze dried at -40°C and DHT crosslinked 24 hrs at 105 °C (3 mm diameter; 5 mm long; pre-wet with PBS) + 2.5 μg Plasmid DNA GDNF using GenePorter2 (modified protocol) + partial wrap (over top only) + covering membrane	8
12	1% collagen cylindrical scaffold, freeze dried at -40°C and DHT crosslinked 24 hrs at 105°C + partial wrap (over top only) + covering membrane	6
13	1% collagen cylindrical scaffold, freeze dried at -40°C and DHT crosslinked 24 hrs at 105°C + laminin (~50μg) + partial wrap (over top only) + covering membrane	6
14	1% collagen cylindrical scaffold, freeze dried at -40°C and DHT crosslinked 24 hrs at 105°C AND carbodiimide crosslinked + laminin (~50μg) + partial wrap (over top only) + covering membrane	6
15	Control: Injury + covering membrane	6

The following summarizes the most recent findings (Groups 12-15) that have not been previously reported in the Annual Reports. The prior findings employing the 5 mm gap spinal cord model indicated that a principal factor in the healing response was the collapse of the surrounding soft tissue into the defect and the degree to which the collagen scaffold implants remained apposed to the stumps of the cut spinal cord. This prompted the recent work to evaluate the gap injury model at an earlier time point; 2 weeks post injury, as compared to a 6 week time point in our prior studies for histological evaluation. Also, it was desired to determine the degree to which select configurations of a covering membrane, wrap, and scaffold could prevent the collapse of overlying tissue into a gap defect, which can impede axonal elongation. The experimental groups were as follows: Group 12 animals were implanted with a 5-mm long, cylindrical scaffold that was dehydrothermally cross-linked. The scaffold filled the gap between the transected spinal cord stumps (Fig. 8-left). A collagen membrane was partially wrapped around the nerve stumps and the implanted scaffold to simulate the dura mater (Fig. 8-center) and another collagen membrane was laid over the entire defect area to serve as a dorsal barrier to overlying tissue (Fig. 8-right). Group 13 was the same as Group 12 except that the collagen scaffold also contained a small amount of laminin. Group 14 was the same as Group 13 except that the collagen scaffold underwent additional cross-linking using carbodiimide. Group 15 was the control group in which the gap injury was created and only the collagen membrane overlying the defect area was implanted (n = 6 for all groups).

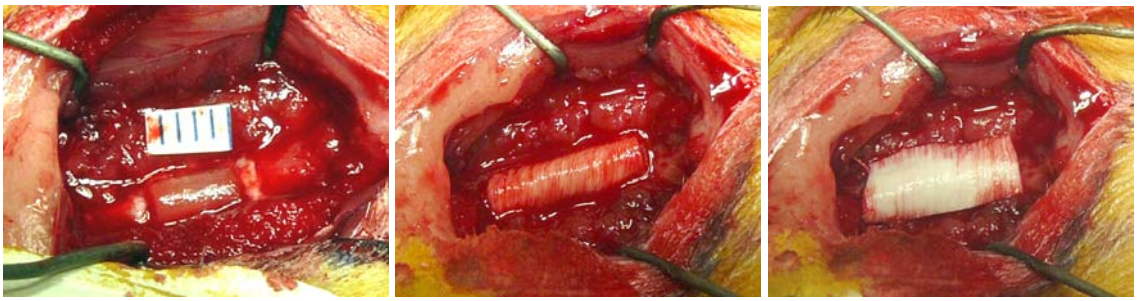

Fig. 8. Collagen scaffold implanted into a 5-mm gap defect in the rat spinal cord (left). A collagen membrane is partially wrapped around the scaffold and spinal cord stumps (center). An additional collagen membrane is placed over the defect area (right).

The presence of a collagen scaffold within the defect did not affect the lesion length at 2 weeks post injury compared to non-implanted control animals (Fig. 9). There was collapse of overlying tissue into the defect in all groups. However, the group with an implanted scaffold that was cross-linked using carbodiimide maintained almost twice the spinal canal height compared to control (Fig. 10). Examples of tissue collapse into the defect are shown in Fig. 11A and 11B, whereas Fig. 11C shows an example where there is little collapse of tissue into the defect.

In all groups there was intense GFAP staining of the spinal cords stumps on both sides of the defect (Fig. 12). However, there was no GFAP staining within the defect neither in animals with implanted collagen scaffolds or in controls (Fig. 13). Thus, there was an absence of astrocyte migration into the defect at 2 weeks post injury.

In summary, the animal studies employing a 5 mm gap in the thoracic spinal cord of the rat demonstrated that collagen membranes and tubes re not sufficient to prevent the collapse of surrounding soft tissues into the gap. A carbodiimide cross-linked porous cylindrical scaffold prevented, to some extent, this collapse. However, use of the scaffold carries with it the

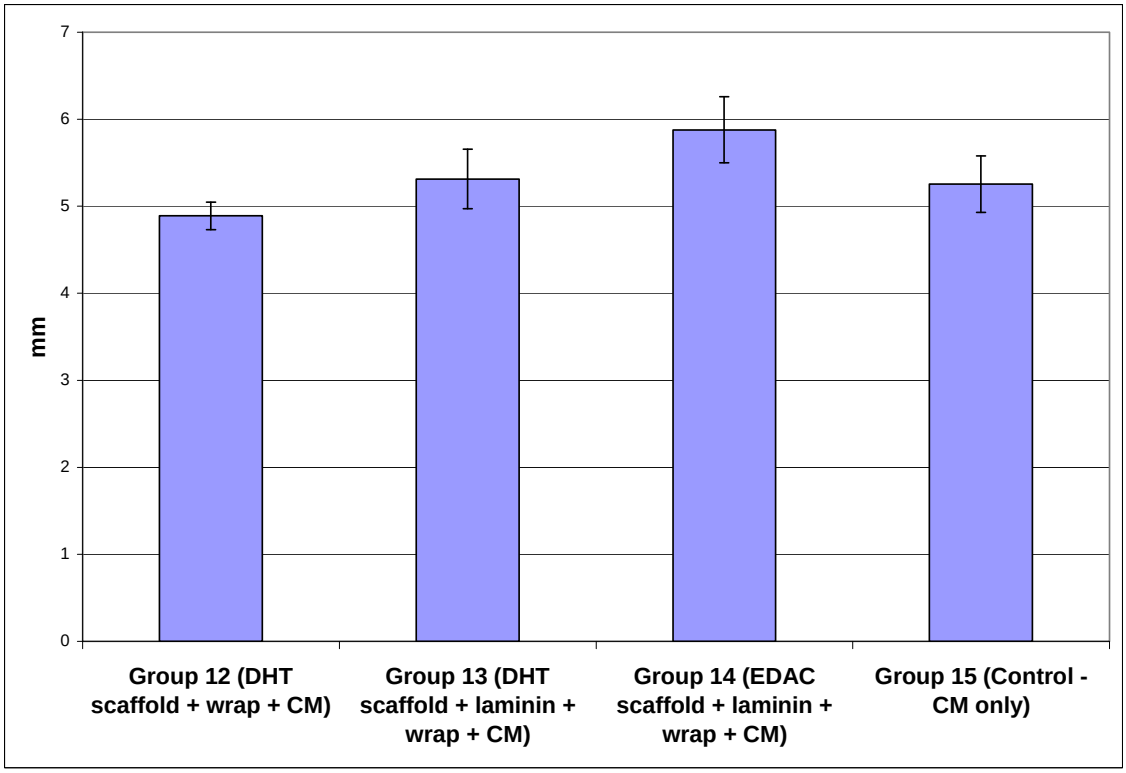

Fig. 9. Lesion length.

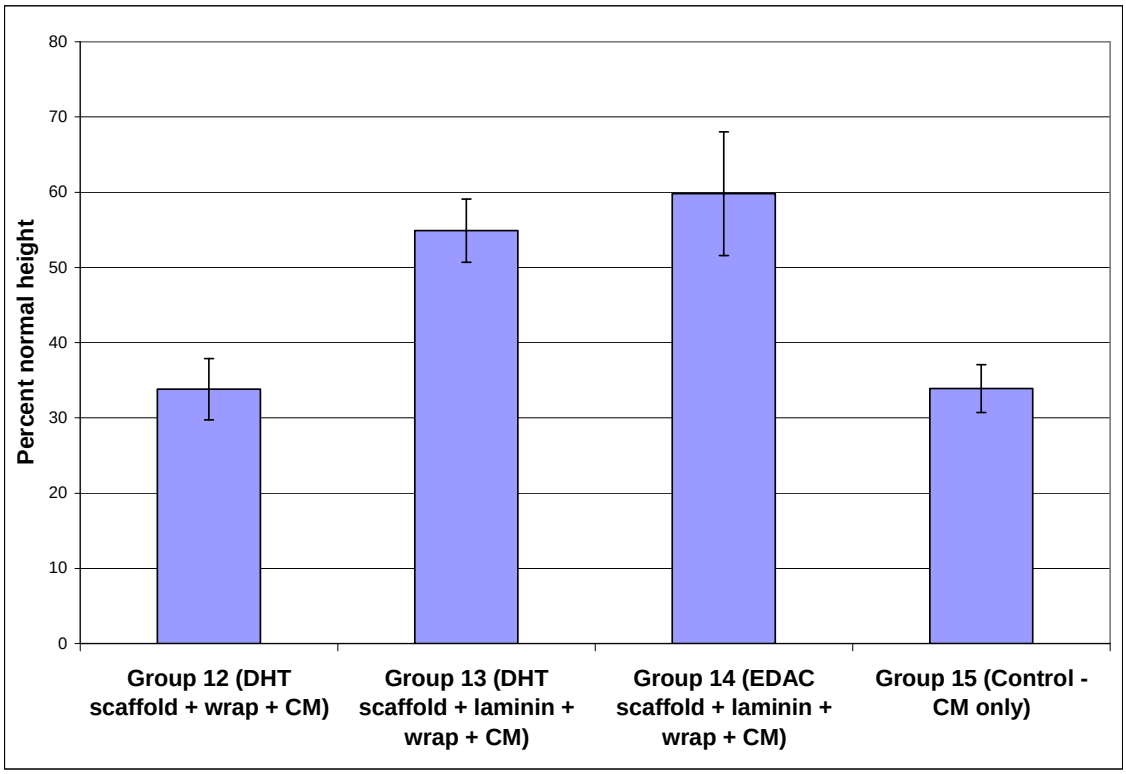

Fig. 10. Height of the spinal canal at the location of the defect.

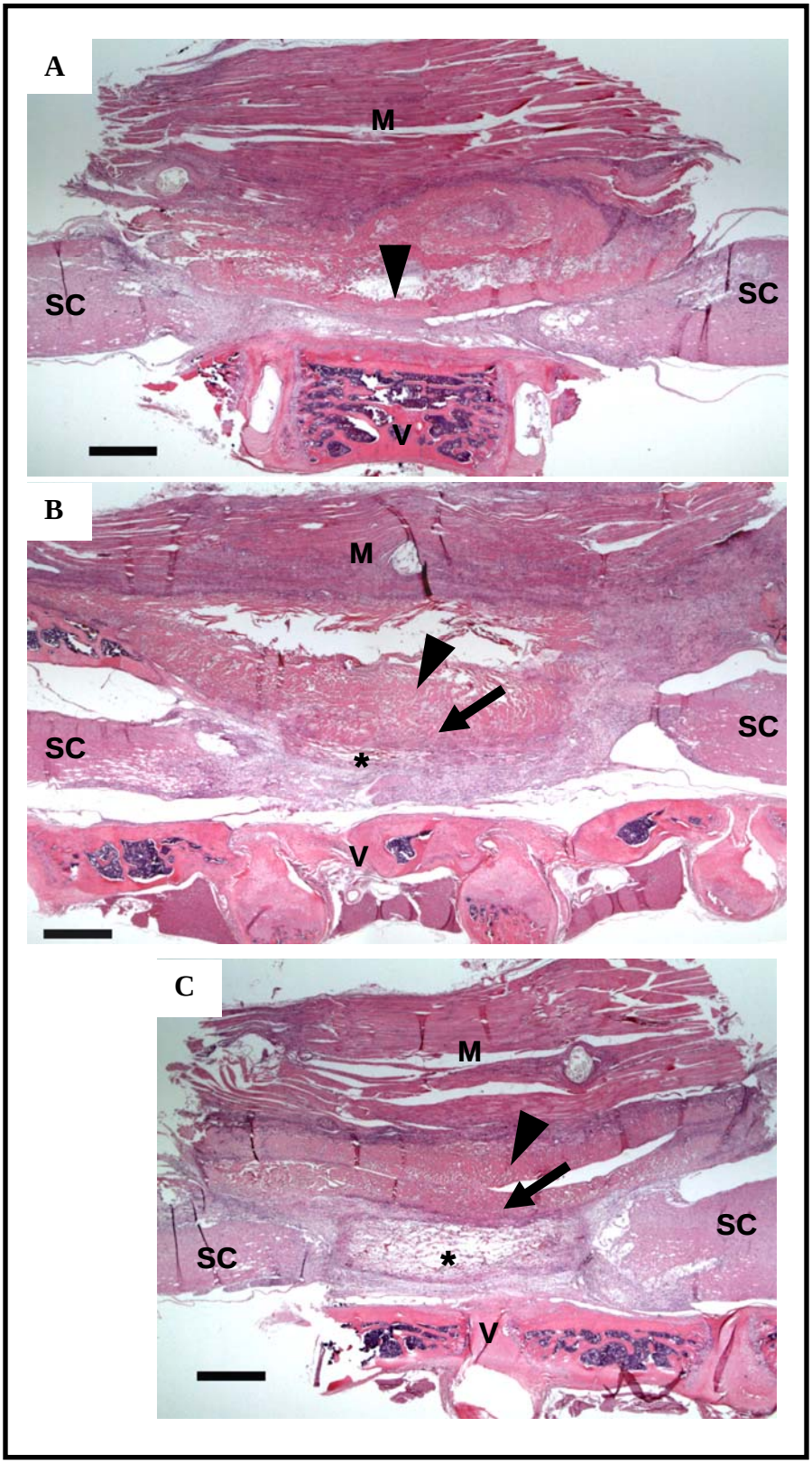

Fig. 11. H&E staining of a 5-mm gap defect in a rat spinal cord with collagen implants after 2 weeks. **A**: Animal receiving overlying collagen membrane only (arrowhead). There is collapse of the membrane and overlying muscle (M) tissue into the defect. A thin cord of fibrous tissue is seen connecting the rostral and caudal spinal cord stumps (SC). **B**: Animal receiving collagen scaffold (*) + membrane wrap (arrow) + overlying membrane (arrowhead). The membrane and overlying muscle (M) tissue is seen collapsed into the defect and compressing the scaffold (*). **C**: Animal receiving collagen scaffold (*) + membrane wrap (arrow) + overlying membrane (arrowhead). Here the overlying tissue is not collapsed into the defect and the scaffold (*) maintains its original shape. SC, spinal cord. V, vertebrae. M, muscle. Scale 1-mm.

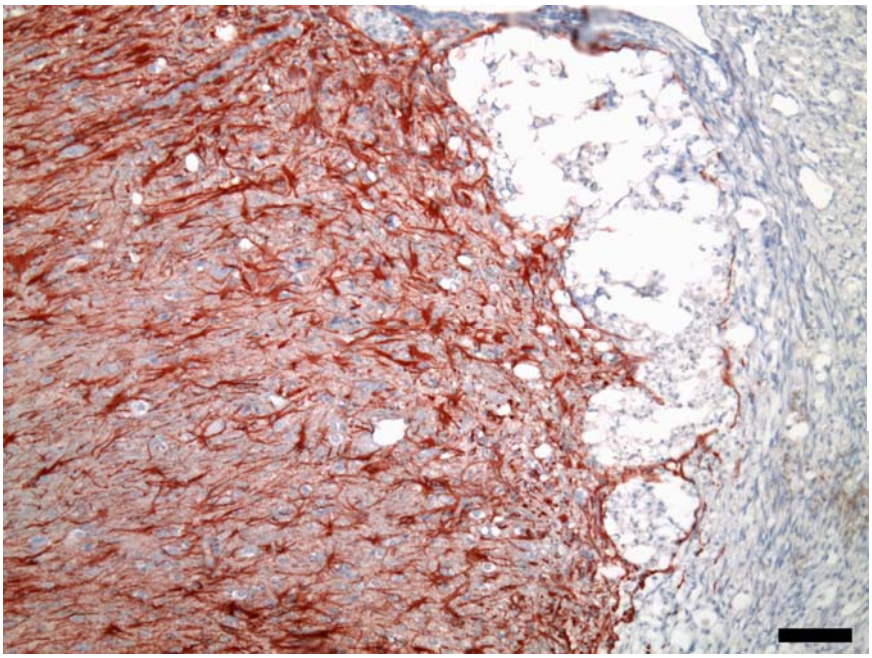

Fig. 12. The interface between the spinal cord stump and the defect in a representative animal. Astrocytes within the spinal cord stump are stained red using an anti-GFAP antibody. Scale 100 μm.

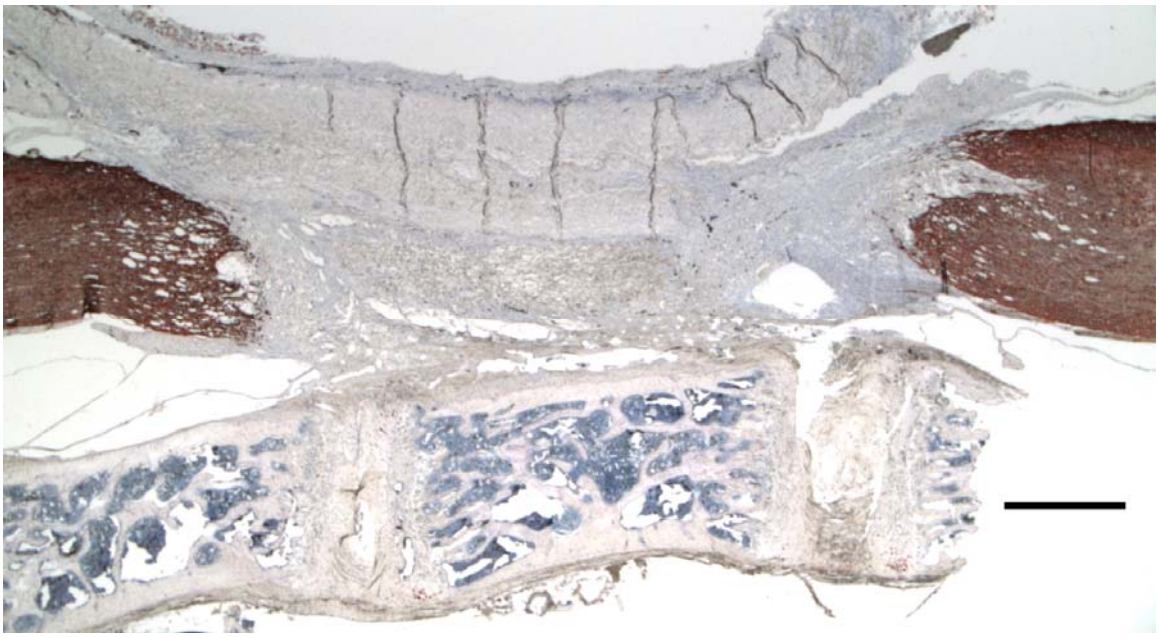

Fig. 13. There is intense GFAP staining of the rostral and caudal spinal cord stumps, however, there is no GFAP staining within the defect. Scale 1 mm.

challenge of maintaining contact of the spinal cord stump with the scaffold. When such contact cannot be maintained, fibrous tissue can become interposed between the stump and the scaffold, and inhibit neural cell infiltration of the scaffold. These findings question the value of the gap model for screening devices for spinal cord regeneration, particularly as most clinical spinal cord injuries do not result in a segmental defect.

III. KEY RESEARCH ACCOMPLISHMENTS

- Development of methods to fabricate collagen tubes and porous cylindrical collagen scaffolds with axially oriented pores.
- Demonstration of the problem of preventing collapse of surrounding soft tissue into gaps in the spinal cord.
- Development of porous collagen-hyaluronic acid scaffolds.
- Development of magnetized calcium nanoparticles for the non-viral transfection of stem cells with plasmid DNA encoding neurotrophic factors.

IV. REPORTABLE OUTCOMES

1. Methods to fabricate porous cylindrical collagen scaffolds with axially oriented pores.
2. Response to select collagen devices in a 5-mm gap in the rat spinal cord.
3. Method for the production of porous collagen-hyaluronic acid scaffolds.
4. Development of magnetized calcium nanoparticles for the non-viral transfection of stem cells with plasmid DNA encoding neurotrophic factors.
5. Utilization of gelatin and chitosan nanoparticles for the non-viral transfection of cells with the gene for a growth factor.
6. Development of collagen gels capable of being cross-linked *in vivo*.

V. CONCLUSIONS

Collagen devices can serve in several therapeutic capacities in the treatment of spinal cord injury. Novel nanoparticles can facilitate the non-viral transfection of MSCs with the genes for neurotrophic factors for their ultimate treatment of spinal cord injury. Injectable collagen gels capable of being cross-linked *in vivo* hold the promise for the treatment of a wide array of spinal cord injuries.

VI. REFERENCES

1. Madaghiele M, Sannino A, Yannas IV, Spector M. Collagen-based matrices with axially oriented pores. J Biomed Mater Res A 2008;85(3):757-67.
2. Tang S, Spector M. Incorporation of hyaluronic acid into collagen scaffolds for the control of chondrocyte-mediated contraction and chondrogenesis. Biomed. Mater.: Mater. in Tissue Engr. and Regen. Med. 2007:S135-S141.
3. Wang TW, Spector M. Development of hyaluronic acid-based scaffolds for brain tissue engineering. Acta Biomater 2009;5(7):2371-84.
4. Sung HW, Chang WH, Ma CY, Lee MH. Crosslinking of biological tissues using genipin and/or carbodiimide. J Biomed Mater Res A 2003;64(3):427-38.
5. Sung H, Huang R, Huang L, Tsai C. In vitro evaluation of cytotoxicity of a naturally occurring cross-linking reagent for biological tissue fixation. Journal of biomaterials science. Polymer edition 1999;10(1):63.
6. Chang Y, Tsai CC, Liang HC, Sung HW. Reconstruction of the right ventricular outflow tract with a bovine jugular vein graft fixed with a naturally occurring crosslinking agent (genipin) in a canine model. J Thorac Cardiovasc Surg 2001;122(6):1208-18.
7. Chang Y, Tsai CC, Liang HC, Sung HW. In vivo evaluation of cellular and acellular bovine pericardia fixed with a naturally occurring crosslinking agent (genipin). Biomaterials 2002;23(12):2447-57.

8. Suzuki H, Yamazaki M, Chiba K, Sawanishi H. Characteristic properties of genipin as an activator in neuronal nitric oxide synthase. Journal of Health Science 2007;53(6):730-733.
9. Yamazaki M, Chiba K. Neurotrophic effects of genipin on Neuro2a cells. J Health Sci 2005;51(6):687-692.
10. Yamazaki M, Chiba K, Mohri T, Hatanaka H. Cyclic GMP-dependent neurite outgrowth by genipin and nerve growth factor in PC12h cells. European journal of pharmacology 2004.
11. Koo HJ, Lim KH, Jung HJ, Park EH. Anti-inflammatory evaluation of gardenia extract, geniposide and genipin. J Ethnopharmacol 2006;103(3):496-500.
12. Sundararaghavan HG, Monteiro GA, Lapin NA, Chabal YJ, Miksan JR, Shreiber DI. Genipin-induced changes in collagen gels: correlation of mechanical properties to fluorescence. J Biomed Mater Res A 2008;87(2):308-20.
13. Xu X, Capito RM, Spector M. Delivery of plasmid IGF-1 to chondrocytes via cationized gelatin nanoparticles. J Biomed Mater Res A 2008;84(1):73-83.
14. Xu X, Capito RM, Spector M. Plasmid size influences chitosan nanoparticle mediated gene transfer to chondrocytes. J Biomed Mater Res A 2008;84A(4):1038-1048.
15. Wu H-C, Wang T-W, Bohn MC, Lin F-H, Spector M. Novel magnetic hydroxyapatite nanoparticles as non-viral vectors for the glial cell line-derived neurotrophic factor gene. Advanced Functional Materials 2009;19:1-11.
16. Gage FH, Ray J, Fisher LJ. Isolation, characterization, and use of stem cells from the CNS. Annu Rev Neurosci 1995;18:159-92.

VII. BIBLIOGRAPHY OF PUBLICATIONS AND MEETING ABSTRACTS

A. Publications

1. Tang S, Spector M. Incorporation of hyaluronic acid into collagen scaffolds for the control of chondrocyte-mediated contraction and chondrogenesis. Biomed. Mater.: Mater. in Tissue Engr. and Regen. Med. 2007:S135-S141.
2. Madaghiele M, Sannino A, Yannas IV, Spector M. Collagen-based matrices with axially oriented pores. J Biomed Mater Res A 2008;85(3):757-67.
3. Xu X, Capito RM, Spector M. Delivery of plasmid IGF-1 to chondrocytes via cationized gelatin nanoparticles. J Biomed Mater Res A 2008;84(1):73-83.
4. Xu X, Capito RM, Spector M. Plasmid size influences chitosan nanoparticle mediated gene transfer to chondrocytes. J Biomed Mater Res A 2008;84A(4):1038-1048.
5. Wang TW, Spector M. Development of hyaluronic acid-based scaffolds for brain tissue engineering. Acta Biomater 2009;5(7):2371-84.
6. Wu H-C, Wang T-W, Bohn MC, Lin F-H, Spector M. Novel magnetic hydroxyapatite nanoparticles as non-viral vectors for the glial cell line-derived neurotrophic factor gene. Advanced Functional Materials 2009;19:1-11.

B. Meeting Abstracts

Collagen Implants for Spinal Cord Regeneration; R Cholas, Ma C, H-P Hsu, I Yannas, and M Spector; Northeast Bioengineering, March, 2005, Cambridge, MA

Collagen Devices for Cartilage and Spinal Cord Tissue Engineering; S Vickers, S Matin, R Cholas, and M Spector; Korea-China Symposium on Biomaterials and Nano-Bio Technology, Oct. 19-24, 2006, Jeju Island, Korea

Collagen Devices for Spinal Cord Regeneration; M. Spector; Second Department of Defense (DOD) Military Health Research Forum for the Peer Reviewed Medical Research Program (PRMRP), May 1-4, 2006, San Juan, Puerto Rico

Effects of Bridging a Gap in the Rat Spinal Cord with a Collagen Tube and Membrane; S Matin, RH Cholas, H-P Hsu, IV Yannas, and M Spector; Society for Biomaterials Annual Meeting, April 18-21, 2007, Chicago, IL

Fabrication and Characterization of Porous Hyaluronic Acid-Collagen Composite Scaffolds; S Tang, SM Vickers, H-P Hsu' and Myron Spector; Society for Biomaterials Annual Meeting, April 18-21, 2007, Chicago, IL

Incorporation of Osteogenic Protein-1 Plasmid into Chitosan Nanoparticles for Non-Viral Gene Transfer to Chondrocytes; X Xu, RM Capito, and M Spector; Society for Biomaterials Annual Meeting, April 18-21, 2007, Chicago, IL

Non-Viral Transfer of GDNF Plasmid DNA to Mesenchymal Stem Cells via Collagen Scaffolds; C Bolliet, MC Bohn, and M Spector; TERMIS North America, June 13-16, 2007, Toronto, Canada

Collagen Tubes to Facilitate Regeneration of the Adult Rat Spinal Cord; R Cholas, H-P Hsu, IV Yannas, and M Spector; TERMIS North America, June 13-16, 2007, Toronto, Canada

Novel Magnetic-Hydroxyapatite Nanoparticles for Non-Viral Gene Delivery; H-C Wu, MC Bohn, F-H Lin, and M Spector**;** TERMIS North America; December 6-10, 2008, San Diego, California

VIII. LIST OF PERSONNEL RECEIVING PAY FROM THE RESEARCH EFFORT

Myron Spector, Ph.D.
Hu-ping hsu, M.D.

IX. APPENDIX (REPRINTS OF PUBLICATIONS)

1. Tang S, Spector M. Incorporation of hyaluronic acid into collagen scaffolds for the control of chondrocyte-mediated contraction and chondrogenesis. Biomed. Mater.: Mater. in Tissue Engr. and Regen. Med. 2007:S135-S141.
2. Madaghiele M, Sannino A, Yannas IV, Spector M. Collagen-based matrices with axially oriented pores. J Biomed Mater Res A 2008;85(3):757-67.
3. Xu X, Capito RM, Spector M. Delivery of plasmid IGF-1 to chondrocytes via cationized gelatin nanoparticles. J Biomed Mater Res A 2008;84(1):73-83.
4. Xu X, Capito RM, Spector M. Plasmid size influences chitosan nanoparticle mediated gene transfer to chondrocytes. J Biomed Mater Res A 2008;84A(4):1038-1048.
5. Wang TW, Spector M. Development of hyaluronic acid-based scaffolds for brain tissue engineering. Acta Biomater 2009;5(7):2371-84.
6. Wu H-C, Wang T-W, Bohn MC, Lin F-H, Spector M. Novel magnetic hydroxyapatite nanoparticles as non-viral vectors for the glial cell line-derived neurotrophic factor gene. Advanced Functional Materials 2009;19:1-11.

Biomed. Mater. **2** (2007) S135–S141 doi:10.1088/1748-6041/2/3/S10

Incorporation of hyaluronic acid into collagen scaffolds for the control of chondrocyte-mediated contraction and chondrogenesis

Shunqing Tang[1,2,3] **and Myron Spector**[2,3]

[1] Department of Biomedical Engineering, Jinan University, Guangzhou 510632, People's Republic of China
[2] Tissue Engineering, VA Boston Healthcare System, Boston, MA 02130, USA
[3] Department of Orthopaedic Surgery, Brigham and Women's Hospital, Harvard Medical School, Boston, MA 02115, USA

E-mail: tshunqt@jnu.edu.cn

Received 20 April 2007
Accepted for publication 17 May 2007
Published 30 July 2007
Online at stacks.iop.org/BMM/2/S135

Abstract
Hyaluronic acid (HA), a principal matrix molecule in many tissues, is present in high amounts in articular cartilage. HA contributes in unique ways to the physical behavior of the tissue, and has been shown to have beneficial effects on chondrocyte activity. The goal of this study was to incorporate graduated amounts of HA into type I collagen scaffolds for the control of chondrocyte-mediated contraction and chondrogenesis *in vitro*. The results demonstrated that the amount of contraction of HA/collagen scaffolds by adult canine articular chondrocytes increased with the HA content of the scaffolds. The greatest amount of chondrogenesis after two weeks was found in the scaffolds which had undergone the most contraction. HA can play a useful role in adjusting the mechanical behavior of tissue engineering scaffolds and chondrogenesis in chondrocyte-seeded scaffolds.

1. Introduction

As one of the tissue engineering triads, along with cells and growth factors, the biomaterial scaffold plays an important role in tissue regeneration. Motivation for the choice of the components of the scaffold can include whether they and the constructed scaffold promote the seeded cells to (1) expand in number and differentiate, (2) efficiently express genes for, and synthesize, extracellular matrix (ECM) molecules and (3) facilitate the assembly of the ECM and cells into a tissue. The components of the scaffold, when released during degradation, may directly affect cell behavior. Moreover, the physical/mechanical properties of scaffold may also affect histogenesis.

One approach to identify promising scaffold components is to consider the role of certain biomolecules in the ECM of the targeted tissue. Hyaluronic acid (HA), also known as hyaluronan, is a ubiquitous and flexible biomacromolecule in the ECM of multiple tissues [1]. HA can form a polyion complex with the collagen to fix and assemble collagen molecules released by cells. This process is necessary for cells to construct ECM niches in their early stage of expansion and differentiation, in order to allow soluble as well as insoluble molecules subsequently released by the cell to be retained in the ECM, thus facilitating histogenesis. There are other roles, including mechanical as well as metabolic and biochemical, that HA also play, especially in tissues, such as cornea, cartilage, and skin, in which the HA content is relatively high.

HA and HA-containing scaffolds have often been reported to have positive effects in stimulating chondrocyte biosynthesis of ECM [2, 3]. HA has frequently been incorporated into scaffolds with other biomaterials such as collagen [4–6], chitosan [7, 8] and gelatin [9] for cartilage tissue engineering.

Physical features of the scaffold, including pore characteristics and mechanical properties, can affect vital aspects of histogenesis. Prior work has demonstrated

contraction of chondrocyte-seeded collagen scaffolds related to the cell expression of a contractile actin isoform, α-smooth muscle actin [10]. Subsequent studies demonstrated that this contraction of the construct accelerated chondrogenesis [11], likely in part by collapsing the pores of the construct such that newly synthesized matrix molecules would be captured in the ECM. In the prior investigation, the stiffness, and thus the resistance, of the scaffold to cell-mediated contraction was regulated by the cross-link density of the collagen scaffold. Incorporation of various amounts of HA into collagen scaffolds may provide an alternate approach to regulate the resistance of the construct to contraction. At the same time, HA, when released from the scaffold during degradation, could provide a positive effect on the chondrocyte behavior and on the formation of the types of polyionic complexes that can contribute to the formation of the ECM.

The objective of the current study was to combine various amounts of HA with type I collagen to produce scaffolds for the initial investigation *in vitro*. The chondrocyte-mediated contraction of the constructs was evaluated, and the degree of chondrogenesis in the constructs was examined. Scaffolds comprising chitosan/agarose and agarose/HA were also prepared for comparison.

2. Experimental details

2.1. Preparation of HA containing scaffolds

Insoluble type I collagen (bovine tendon microfibrillar collagen; Integra LifeSciences, Plainsboro, NJ), which was swelled in 0.05 M acetic acid solution at a concentration of 6 mg ml^{-1} (as described in [12]), was mixed with HA sodium (*Streptococcus zooepidermicus*; Sigma Chemical Co., St Louis, MO), which was directly dissolved in water at a concentration of 10 mg ml^{-1}. The mixture was blended at a high speed at 4 °C for 1 h. The pH value of the mixture was adjusted with 2 M HCl in order to prevent the formation of polyion complexes. The collagen slurry alone, or homogenously mixed with the HA solution in a selected weight ratio, was degassed by vacuum or centrifuged. The slurry was poured into six-well polystrene tissue culture plates and freeze–dried to form a 3D porous HA/collagen scaffold (using a published protocol [13]). The HA solution alone and the collagen slurry alone were directly poured into the polystyrene wells and freeze–dried to produce pure HA and pure collagen scaffolds.

As comparisons, 35% chitosan/agarose and 80% agarose/HA scaffolds were prepared by mixing a hot agarose solution with a chitosan (400 cp) solution in 0.05 M acetic acid and with the HA solution, respectively, in selected ratios. These chitosan/agarose and agarose/HA solutions were also freeze–dried at 0 °C.

Eight mm diameter samples were cut from sheets of the scaffolds, approximately 2 mm thick, by a punch, and then cross-linked with 1-ethyl-3-(3-dimethylaminopropyl) carbodiimide (EDC)–*N*-hydroxysuccinide (NHS) using a 7 day protocol previously described [14] or dehydrated by heat treatment under vacuum at 95 °C for 24 h (dehydrothermal treatment). Samples were sterilized by epoxyethane gas.

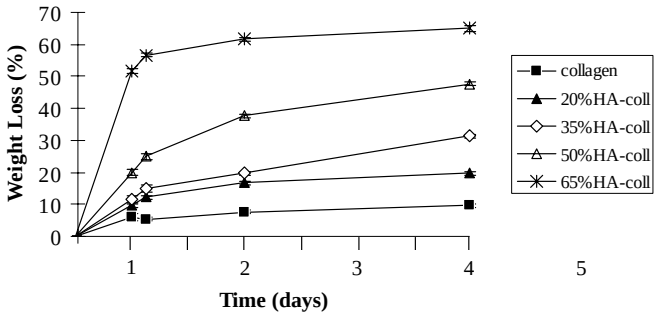

Figure 1. Graph showing the weight loss of scaffolds with time in PBS as a percentage of the original weight of the scaffold ($n = 3$). The data are plotted with the mean ± standard error of the mean. The error bars fall within the symbols, and thus cannot be seen.

2.2. Morphological evaluation of the scaffolds by light microscopy

Scaffolds were examined by light microscopy during the process of swelling in order to gain additional insights into the behavior of the various HA–collagen formulations and judge the relative strength of the scaffold in the culture medium. Samples of the scaffolds swelled in water for 24 h were placed onto glass slides, and images were captured on an Olympus light microscope at various time intervals.

2.3. Analysis of HA in scaffolds

The HA concentration of solutions was analyzed by a carbazole method [15] that was a modification of the Bitteer and Muir method for the quantification of hexuronic acids [16, 17]. Stock solutions of sodium tetraborahydrate in sulfuric acid and carbazole in ethanol were prepared. Samples containing HA were added to the sodium tetraborahydrate and the closed tubes were shaken and then heated. Carbazole was subsequently added and the tubes heated. The absorption of the samples was measured at 530 nm (DU-530 UV–vis spectrophotometer; Beckman Coulter, Fullerton, CA). A standard curve was used to obtain the concentrations of the HA samples.

2.4. Degradation of scaffold in phosphate buffered saline

The HA-containing scaffolds ($n = 3$) were put into a phosphate buffered saline (PBS) solution for degradation. After a certain time interval, the remaining scaffold was taken out, washed, dried and weighed. Loss of the weight of the scaffolds in PBS could be calculated with degradation time.

2.5. Chondrocyte-seeded scaffolds

Chondrocytes were isolated by enzymatic digestion of articular cartilage from the knee (stifle) joint of an adult dog. The cartilage samples were treated with pronase (20 U mL^{-1}, Sigma) for 1 h, followed by type II collagenase (200 U mL^{-1}, Worthington Biochemical, Lakewood, NJ) overnight. The cells were expanded in number in monolayer culture through three subcultures (i.e. passage three cells). The medium used

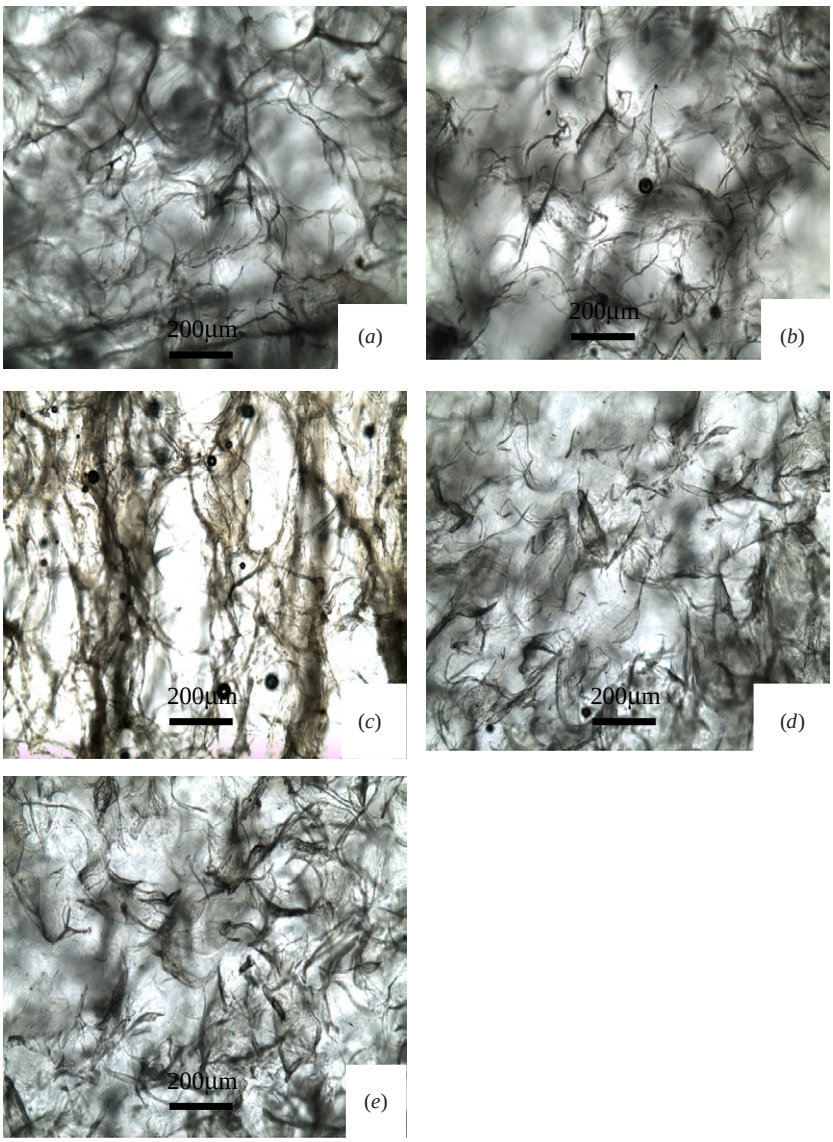

Figure 2. Images of the various scaffolds after swelling in water for 24 h. (*a*)–(*e*): 10%, 35%, 50%, 65% and 80% HA/collagen scaffolds cross-linked by EDC.

for the monolayer expansion of the cells was adapted from a prior study [18]: basal medium (DMEM, 0.1 mM nonessential amino acids, 100 mM *N*-2-hydroxyethylpiperazine-*N*-2-ethanesulfonic (HEPES) buffer, 100 U mL^{-1} penicillin, 100 mg mL^{-1} streptomycin and 0.29 mg mL^{-1} l-glutamine, all from Gibco Life Technologies, Carlsbad, CA) supplemented with 10% FBS, 1 ng mL^{-1} transforming growth factor-b1 (TGFβ1; R&D Systems, Minneapolis, MN), 5 ng mL^{-1} fibroblast growth factor-2 (FGF-2; R&D Systems) and 10 ng mL^{-1} platelet derived growth factor-$\beta\beta$ (PDGF-$\beta\beta$; R&D Systems). After expansion the cells were trypsinized and resuspended in chondrogenic medium: basal medium supplemented with 1% insulin transferrin-selenium (ITS)+1 Premix (Sigma), 10 ng mL^{-1} TGF-β1, 10^{-7} M dexamethasone (Sigma), 0.1 mM ascorbic acid 2-phosphate and 1.25 mg mL^{-1} bovine serum albumin. HA/collagen scaffolds ($n = 3$) prepared with 10%, 35%, 50%, 80% and 100% (w/w) HA and cross-linked for 7 days were seeded with the chondrocytes using a pipette method. One million cells were pipetted onto one side of the sample and then the sample was flipped and 1 million cells were pipetted onto the opposite side. The cell-seeded matrices were put into agarose-coated 12-well plates and grown in the chondrogenic medium for two weeks. The medium was changed every other day.

2.6. Contraction of scaffolds during culture

The average diameter of seeded-cell scaffolds was measured with a millimeter rule every other day in culture ($n = 3$). The decrease of diameter of scaffolds was used for evaluating chondrocyte-mediated contraction of the scaffolds. The cell-seeded scaffolds often displayed an opaque, whitish, core surrounded by a transparent periphery without cells, or with a few cells. Separate measurements were made of the diameter of the core and the total diameter of the construct.

2.7. Histology

After two weeks in culture, the chondrocyte-seeded scaffolds were fixed in 10% formalin, dehydrated using conventional techniques and embedded into paraffin and microtomed. Sections, approximately 7 μm thick, were stained with Safranin-O for proteoglycan and immunohistochemical analysis for type II collagen as described previously [11].

3. Results and discussion

3.1. Degradation of scaffolds

Quantitative analyses showed that the HA contents in the scaffolds were close to the prepared value (data not shown). The degradation rate in PBS increased with increasing HA content ($n = 3$; figure 1). By 7 days the scaffolds appeared to lose most of the HA, as demonstrated by the final weight loss values that approximated the initial percentage of the HA in the scaffolds. That the collagen itself underwent some degradative loss (figure 1) explains differences between the final weight loss values and the initial amount of HA in the respective scaffolds. The majority of the weight loss of the scaffold with the highest HA content (65% HA/collagen) occurred rapidly, within 24 h (figure 1). After 24 h the weight loss curve generally paralleled the weight loss of the pure collagen scaffold. The 20% HA/collagen scaffold also paralleled the collagen loss rate after the first 24 h loss of HA. The weight losses from the scaffolds containing 35 and 50% HA occurred more gradually over the 7 day period, with about 50% of the weight lost in the first 24 h (figure 1). Two-factor analysis of variance (ANOVA) demonstrated significant effects of HA content ($p < 0.0001$, power $= 1$) and time in culture ($p < 0.0001$, power $= 1$) on the weight loss. Fisher's protected least-square differences post-hoc testing demonstrated significant differences in comparisons between each pair of groups.

The loss of HA would likely result in the softening and loss of stiffness of the HA-containing scaffolds. In contrast, the collagen samples lost little of their weight in PBS over the time course of the experiment, and this likely maintained more of their mechanical properties.

Light microscopy examination of the scaffolds after swelling in water for 24 h revealed differences in the morphological features (figure 2). The higher the HA content of the scaffolds the less distinct were the struts of the scaffold, such that they only provided a blurred image by light microscopy. The 50% HA/collagen scaffolds which were not cross-linked or only dehydrothermally treated did not yield clear images of a fibrous network likely owing to their softening in the water. In comparison, 10%, 35%, 50%, 65% and 80% HA/collagen scaffolds cross-linked by EDC displayed distinct struts comprising the sponge-like materials, even after 24 h in water (figures 2(*a*)–(*e*)).

In the present study, a few 'soft' scaffolds were prepared to investigate how the compliant scaffold might affect the behavior of chondrocytes grown in the scaffolds. Agarose was chosen to trap seeded cells and ECM in the scaffold. Light microscopy of chitosan/agarose scaffold without cross-linking and cross-linked agarose/HA after swelling in water for 24 h did not reveal distinct fibrous networks.

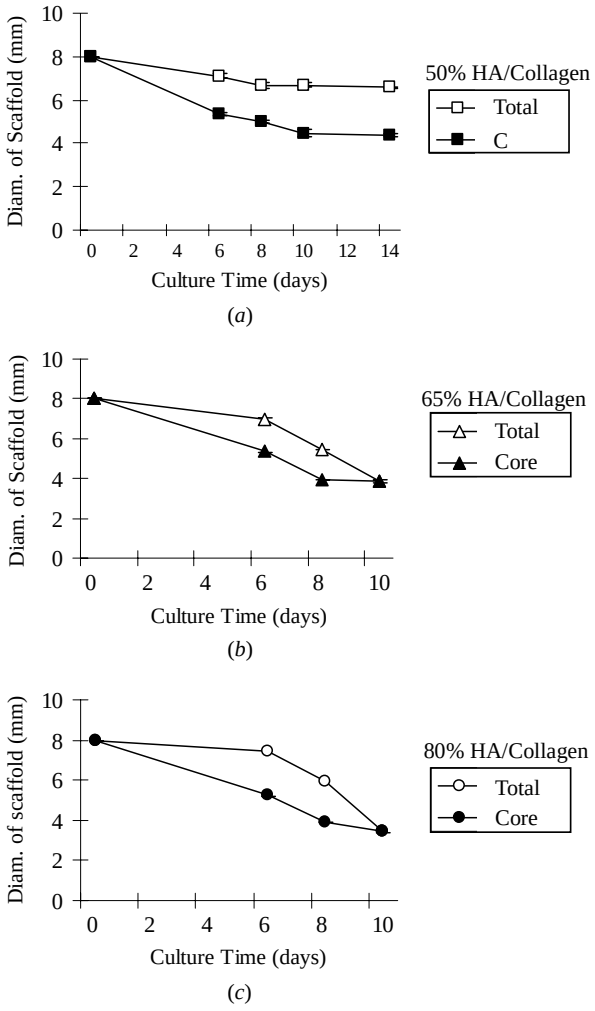

Figure 3. Contraction of HA/collagen scaffolds cross-linked by EDC with culture time (total, total diameter including white center and transparent edge; core, measurement of core diameter only). (*a*) 50% HA/collagen; (*b*) 65% HA/collagen; (*c*) 80% HA/collagen.

3.2. Contraction of scaffolds

Control scaffolds without seeded cells showed a slight increase in diameter as a result of swelling in the culture medium. Chondrocyte-seeded scaffolds with lower HA contents (10% and 35% HA/collagen scaffolds) displayed little reduction in size with time in culture (data not shown). Contraction of the chondrocyte-seeded scaffolds with higher HA contents (50%, 65% and 80% HA/collagen samples) was evident by 7 days in culture, with an increase in the amount of contraction found with increasing HA content (figures 3(*a*)–(*c*)). The 10 day mean total diameters of the 50, 65 and 80% HA/collagen scaffolds were 6.7, 3.9 and 3.4 mm, respectively. In each of these three groups, after 6 and 8 days, there were noticeable core regions of the scaffolds which could be measured separately from the total diameter of the scaffolds (figure 3). However, by 10 days, transparent peripheral regions of the 65 and 80% HA/collagen scaffolds, which earlier appeared to have a few cells and could be distinguished from the core, were no longer observed. Distinctly appearing core and

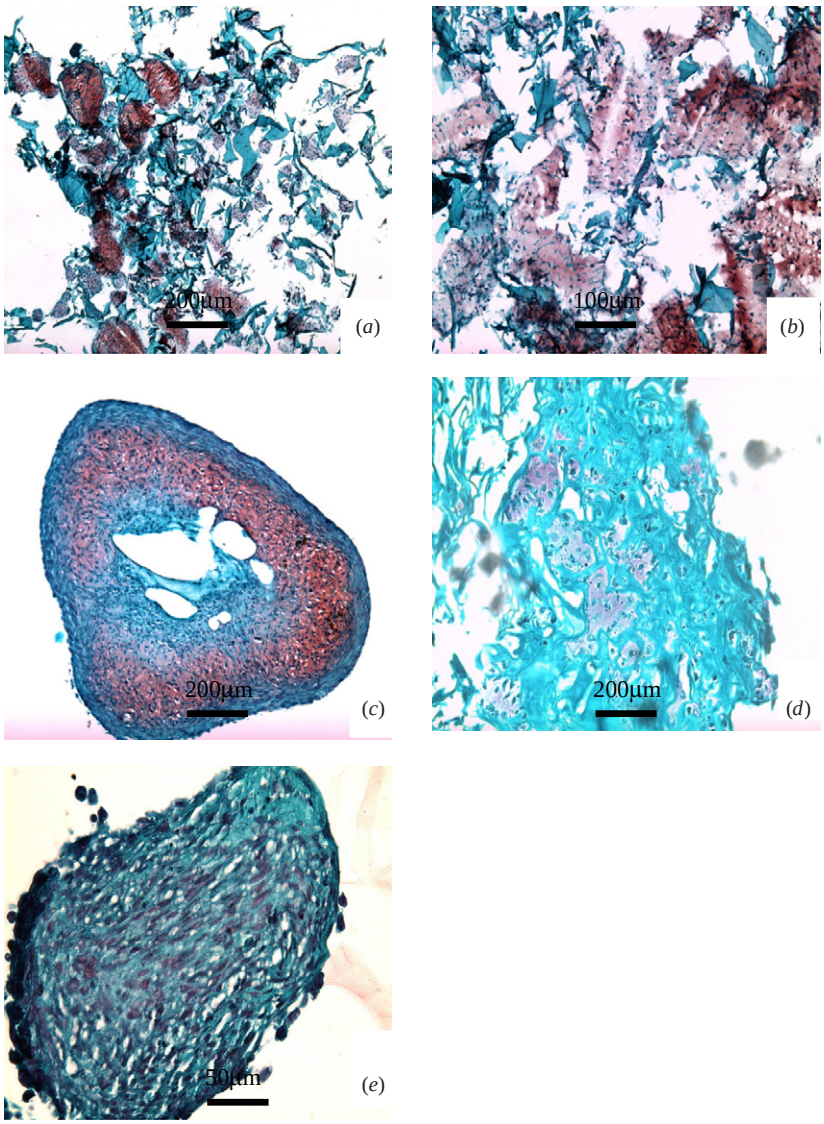

Figure 4. Histological micrographs of Safranin-O stained sections of chondrocyte-seeded HA–collagen scaffolds (P3 cells, 2 weeks): (*a*)–(*c*) 50%, 80%, 100% HA/collagen cross-linked by EDC respectively, (*d*) 35% chitosan/agarose, (*e*) 80% agarose/HA.

periphery zones remained in the 50% HA/collagen scaffolds to the completion of the experiment in 14 days. Three-factor ANOVA revealed significant effects of HA content, time in culture and measurement of the core region of the scaffold or total diameter on the diameter of the scaffold (all factors with $p < 0.0001$, power $= 1$).

This finding indicated that the greater the collagen cross-link density of the scaffolds resulting from reduced HA content, the greater the resistance of the scaffold to contraction by the chondrocytes. The contraction of scaffolds could also be affected by the decrease in the stiffness of the scaffolds as the struts of the material degrade. Examination of the edge of chondrocyte-seeded scaffolds indicated that the periphery (transparent edge) of 50% HA/collagen scaffolds, which did not contain cells (or had few cells), did not contract although most of HA in it is lost; in comparison, the peripheral regions of the 65% and 80% HA/collagen scaffolds did eventually collapse.

These results demonstrate that adjusting the HA content of collagen scaffolds provides control over the change in the stiffness of the scaffold with time in culture and on its resistance to cell-mediated contraction. At the same time, addition of HA to the collagen scaffold could allow the beneficial effects of HA on cells to be realized as the HA is released.

3.3. Histology of the cell-seeded scaffolds

It was found that the cells in the stiff, cross-linked scaffolds which did not contract (namely, 10% and 35% HA/collagen scaffolds) exhausted nutrients in culture medium, judged by the change of the color of the culture medium. This suggested that the open pores, confirmed by histology, facilitated the diffusion of nutrients to the cells.

There was no evident positive Safranin-O staining for proteoglycan in scaffolds containing up to 80% HA (figures 4(*a*) and (*b*)). There was, however, some difficulty

in obtaining complete histological sections from some of these scaffolds because they fragmented during microtomy (figures 4(*a*) and (*b*)). Therefore, extracellular matrix containing proteoglycan may have been lost during the histological procedure. The pure HA scaffolds that contracted greatly (to about 1 mm in diameter) demonstrated the presence of proteoglycan reflected in positive Safranin-O staining (figure 4(*c*)). In addition, cells with chondrocytic morphology could be found in lacunae, thus demonstrating chondrogenesis.

This finding supports the previous work [11] that demonstrated that the degree of chondrogenesis increases with decreasing cross-link density and increasing contraction of the scaffold. This may be due to the resulting increase in cell density and decrease in pore volume that favor the retention of newly synthesized matrix molecules. The current finding also supports prior observations that the greater the amount of chondrogenesis the less the amount of residual scaffold material found in the samples. The present study raises the question of the favorable influence of increasing HA content in the scaffolds on the process of cartilage formation.

In comparison, there is little newly synthesized GAG and type II collagen in the chitosan/agarose scaffold without cross-linking (figure 4(*d*)) although the culture condition was the same with the HA-containing one. So too was there little chondrogenesis found in cross-linked agarose/HA scaffold (figure 4(*e*)). This suggested that two factors, high HA content and soft structure, were important for chondrocytes expressing GAG and type II collagen.

In the chitosan/agarose scaffold, although the agarose gel had the potential to capture the newly synthesized GAG, there was less ECM compared to the HA scaffolds perhaps because of the absence of HA as a stimulator agent. In the agarose/HA scaffold, although HA might have been available to promote chondrocyte biosynthesis of ECM, cross-linking coupled with the low HA content retarded chondrocyte-mediated contraction of the scaffold.

Chondrocytes in the scaffolds can readily be exposed to fragments of degraded HA from the scaffold, which may promote chondrogenesis. In future work it will be useful to determine how to control the HA degradation process, and to determine the HA fragments which have the greatest effects on chondrocytes.

While contraction of the chondrocyte-seeded scaffold can favor chondrogenesis *in vitro*, this approach may be difficult to harness to make implantable cartilaginous constructs of certain size. Additional work will be required to consider how best to produce tissue-engineered cartilaginous constructs using this approach.

4. Conclusions

The components and structures of scaffold have critical effects on seeded chondrocytes expressing and assembling ECM molecules. Addition of HA to type I collagen scaffolds can promote chondrogenesis through its effect in reducing the mechanical resistance of the scaffold to chondrocyte-mediated contraction and perhaps to direct effects on the metabolism of the cells.

Acknowledgments

This work was supported by the US Department of Veterans Affairs, Veterans Health Administration, Rehabilitation Research and Development Service, a VA Research Career Scientist Award (MS) and the Department of Defense. The authors gratefully acknowledge Dong Zhang, MD, Hu-Ping Hsu MD and Scott M Vickers, PhD for assistances with cell culture and histology, and preparation of the scaffolds. The authors are also grateful to Professor I V Yannas for use of the facilities in his Fibers and Polymers Laboratory at the Massachusetts Institute of Technology for the preparation of the collagen scaffolds.

References

[1] Lee J Y and Spicer A P 2000 Hyaluronan: a multifunctional, megaDalton, stealth molecule *Curr. Opin. Cell Biol.* **12** 581–6

[2] Ehlers E M, Behrens P, Wunsch L, Kuhnel W and Russlies M 2001 Effects of hyaluronic acid on the morphology and proliferation of human chondrocytes in primary cell culture *Ann. Anat.* **183** 13–7

[3] Goodstone N J, Cartwright A and Ashton B 2004 Effects of high molecular weight hyaluronan on chondrocytes cultured within a resorbable gelatin sponge *Tissue Eng.* **10** 621–31

[4] Liu L S, Thompson A Y, Heidaran M A, Poser J W and Spiro R C 1999 An osteoconductive collagen/hyaluronate matrix for bone regeneration *Biomaterials* **20** 1097–108

[5] Park S N, Lee H J, Lee K H and Suh H 2003 Biological characterization of EDC-crosslinked collagen–hyaluronic acid matrix in dermal tissue restoration *Biomaterials* **24** 1631–41

[6] Park S N, Park J C, Kim H O, Song M J and Suh H 2002 Characterization of porous collagen/hyaluronic acid scaffold modified by 1-ethyl-3-(3-dimethylaminopropyl) carbodiimide cross-linking *Biomaterials* **23** 1205–12

[7] Chang C H, Liu H C, Lin C C, Chou C H and Lin F H 2003 Gelatin-chondroitin-hyaluronan tri-copolymer scaffold for cartilage tissue engineering *Biomaterials* **24** 4853–8

[8] Yamane S, Iwasaki N, Majima T, Funakoshi T, Masuko T, Handa K, Minan A, Monde K and Nishimura S 2005 Feasibility of chitosan-based hyaluronic acid hybrid biomaterial for a novel scaffold in cartilage tissue engineering *Biomaterials* **26** 611–9

[9] Chen J, Li Q, Xu J, Huang Y, Ding Y, Deng H, Zhao S and Chen R 2005 Study on biocompatibility of complexes of collagen-chitosan-sodium hyaluronate and cornea *Artif. Organs* **29** 104–13

[10] Kinner B and Spector M 2001 Smooth muscle actin expression by human articular chondrocytes and their contraction of a collagen–glycosaminoglycan matrix *in vitro J. Orthopaedic Res.* **19** 231–41

[11] Vickers S M, Squitieri L S and Spector M 2006 The effects of cross-linking type II collagen-GAG scaffolds on chondrogenesis *in vitro*: dynamic pore reduction promotes cartilage formation *Tiss. Eng.* **12** 1345–55

[12] Yannas I V, Burke J F, Gordon P L, Huang C and Rubenstein R H 1980 Design of an artificial skin: II.

Control of chemical composition *J. Biomed. Mater. Res.* **14** 107–32
[13] O'Brien F J, Harley B A, Yannas I V and Gibson L 2004 Influence of freezing rate on pore structure in freeze-dried collagen-GAG scaffolds *Biomaterials* **25** 1077–86
[14] Tang S Q, Vickers S M, Hsu H P and Spector M 2007 Fabrication and characterization of porous hyaluronic acid-collagen composite scaffolds *J. Biomed. Mater. Res.* A **82** 323–5
[15] Hedberg E L, Shih C K, Solchaga L A, Caplan A I and Mikos A G 2004 Controlled release of hyaluronan oligomers from biodegradable polymeric microparticle carriers *J. Controlled Release* **100** 257–66
[16] Kosakai M and Yosizawa Z 1979 A partial modification of the carbazole method of bitter and muir for quantitation of hexuronic acids *Anal. Biochem.* **93** 295–8
[17] Platzer M, Ozegowski J H and Neubert R H 1999 Quantification of hyaluronan in pharmaceutical formulations using high performance capillary electrophoresis and the modified uronic acid carbazole reaction *J. Pharm. Biomed. Anal.* **21** 491–6
[18] Crescenzi V, Francescangeli A, Taglienti A, Capitani D and Mannina L 2003 Synthesis and partial characterization of hydrogels obtained via glutaraldehyde crosslinking of acetylated chitosan and of hyaluronan derivatives *Biomacromolecules* **4** 1045–54

Collagen-based matrices with axially oriented pores

Marta Madaghiele,[1,2] Alessandro Sannino,[1] Ioannis V. Yannas,[3,4] Myron Spector[2,3,4,5]
[1]*Department of Engineering for Innovation, University of Lecce, Lecce, 73100 Italy*
[2]*Tissue Engineering, VA Boston Healthcare System, Boston, Massachusetts 02130*
[3]*Department of Mechanical Engineering, Massachusetts Institute of Technology, Cambridge, Massachusetts 02139*
[4]*Department of Biological Engineering, Massachusetts Institute of Technology, Cambridge, Massachusetts 02139*
[5]*Department of Orthopaedic Surgery, Brigham and Women's Hospital, Harvard Medical School, Boston, Massachusetts 02115*

Received 12 January 2007; revised 28 March 2007; accepted 15 May 2007
Published online 26 September 2007 in Wiley InterScience (www.interscience.wiley.com). DOI: 10.1002/jbm.a.31517

Abstract: The aim of this work was the implementation of a simple technique for the production of cylindrical collagen-based scaffolds with axially oriented pore channels. Matrices with this particular porous structure have the potential to improve the regeneration of peripheral nerves and spinal cord by physically supporting and guiding the growth of neural structures across the site of injury. The regenerative potential may be further enhanced when the collagen scaffold is used as a delivery vehicle for exogenous cells and growth factors. The scaffold manufacturing technique described here is based on unidirectional freezing of a collagen suspension and subsequent freeze-drying, which produces nearly axially oriented pores. The mean pore size is dependent on both the concentration of collagen in suspension and the temperature of freezing. Environmental scanning electron microscopy and light microscopy were used to assess qualitatively and quantitatively the pore size and the pore orientation. In particular the definition of an orientation index (OI) was employed as a means to quantify the orientation of the pore channels inside the scaffolds. © 2007 Wiley Periodicals, Inc. J Biomed Mater Res 85A: 757–767, 2008

Key words: collagen; scaffold; porosity; microstructure; tissue engineering

INTRODUCTION

The pore characteristics of degradable scaffolds that generally govern their performance as regenerative templates include the void fraction (percent porosity), pore diameter distribution, and pore interconnectivity. Furthermore, in applications in the peripheral nervous system, in which a scaffold bridges gaps in tissues, the orientation of the pores of the scaffold has also been shown to play a critical role in its performance. An analysis of data from several independent investigations of peripheral nerve regeneration, as well as studies in the central nervous system, showed that axially oriented structures of different types exhibited strong regenerative activity.[1–5]

This work was performed in the Tissue Engineering Laboratories of the VA Boston Healthcare System.

Correspondence to: M. Spector; e-mail: mspector@rics.bwh.harvard.edu

Contract grant sponsors: Department of Defense and the Rehabilitation Research and Development Service, U.S. Department of Veterans Affairs; The Department of Engineering for Innovation of the University of Lecce, Italy

The need for such scaffolds in peripheral nerve and spinal cord tissue engineering strategies prompted the current study to investigate a process for introducing axially aligned pores into a collagen scaffold. Such a matrix not only supports axonal elongation, but is also potentially an effective means for the local delivery of exogenous cells and growth factors to the site of injury.[4,6–8]

The use of collagen–glycosaminoglycan (CG) matrices with longitudinally oriented pores has been reported in several studies on the regeneration of peripheral nerves,[1–3,9–11] spinal cord,[12] and tendon.[13] The porous structure was obtained by freezing a CG suspension via slow was into a cooling bath and subsequent freeze-drying, as described in early studies with CG matrices.[14] The velocity of immersion and the temperature of the freezing bath were found to significantly affect the pore size and the pore orientation of the resulting matrices. Only particular combinations of immersing velocity and freezing temperature were found to yield axially oriented pores for cylindrical scaffolds with a diameter ranging from 1.5 to 3.8 mm.[1,12,13,15,16]

The objective of the present study was to implement a relatively simple technique, based on uniaxial

freezing and subsequent freeze-drying, for the production of collagen-based scaffolds with axially oriented pores to be used as nerve guidance matrices. The fabrication technique proposed in this study employed a different method for creating a longitudinal temperature gradient than the procedure described above for CG scaffolds. The technique has been reported to be successful for the production investigated in the current study of agarose-based scaffolds with linearly oriented pores and, more recently, for the development of anisotropic hydroxyapatite/collagen composites for bone regeneration.[5,17,18] Here we investigate if a similar approach can yield the desired axial orientation in glycosaminoglycan-free collagen matrices. Considering the possible application of the scaffolds as nerve guidance matrices for the regeneration of the spinal cord, only collagen has been used as the starting material instead of a CG copolymer, due to findings indicating that chondroitin-6-sulfate is an inhibitor of regeneration in the central nervous system.[19] In previous work, scaffolds having a diameter of 3 mm and a length of 5 mm have been produced and characterized, corresponding to the mean diameter of the adult rat spinal cord and the typical length of the defect (5 mm complete transection) produced in the rat spinal cord in numerous studies.[12]

Particular attention was directed to the synthesis of scaffolds with different pore diameters, achieved by varying both the concentration of the collagen in suspension and the temperature of freezing. Prior studies demonstrated that the optimal diameter of oriented pores for peripheral nerve regeneration was around 20 μm[10] for a CG scaffold with ~99% porosity. This finding directed the present work to determine conditions that would result in collagen scaffolds of comparable pore size. Mean pore diameters of 120–125 μm were reported in a study of agarose scaffolds.[17]

In our study, the porous structure of the scaffolds was characterized in detail by means of light microscopy and environmental scanning electron microscopy (ESEM). We also describe a method for quantitative evaluation of pore orientation.

MATERIALS AND METHODS

Preparation of collagen scaffolds

The collagen used for the fabrication of the scaffolds was derived from porcine tissue using a proprietary process (Geistlich Biomaterials, Wolhusen, Switzerland). The material is principally type I collagen, with a small amount of type III collagen. This collagen has been used to produce a membrane (Bio-Gide, Geistlich Biomaterials), which has been shown to be safe and effective in various applications in numerous human studies.[20–23] It has been approved by the U.S. Food and Drug Administration for selected clinical applications; the membrane is also commercially available in many European countries. The collagen scaffolds were produced according to the following procedure. The type I/III collagen dry powder (Geistlich Biomaterials) was suspended in dilute hydrochloric acid (pH = 3.2) by mixing at 15,000 rpm in an overhead blender (IKA Works, Wilmington, NC). Hydrochloric acid was used instead of acetic acid to prevent formation of the residual odor, which can persist with the latter acid. The collagen suspension, containing either 0.5 or 2% w/v collagen, was refrigerated during the mixing process (4°C) to avoid the denaturation of the collagen fibers. The slurry was then degassed via centrifugation and injected into 10 cylindrical holes, 3 mm in diameter, machined into a polyethylene plate, 15 mm thick. Prior to the injection of the collagen suspension into the polyethylene mold, copper caps were fitted into the bottom openings of the holes in the mold. Subsequently, the copper-fitted end of the mold was rapidly cooled at two different freezing temperatures, yielding four experimental groups (Table I). Groups I and II were frozen by directly placing the mold onto the shelf of a freeze-dryer (VirTis, Gardiner, NY) and precooled to −40°C for 1 h; for groups III and IV, the freezing of the suspension was achieved by placing the mold onto a copper plate, previously cooled with liquid nitrogen (LN_2) for 10 min. The copper plate onto which the mold was placed was precooled by pouring LN_2 on it until a film of LN_2 formed on its surface, indicating that the temperature of the plate was very close to that of LN_2 (−196°C). During the 10 min necessary for the freezing of the entire length of the scaffolds (15 mm), LN_2 was continuously supplied to avoid temperature changes of the plate. After freezing had occurred, the molds were immediately transferred to a freeze dryer for subsequent lyophilization. The ice phase was thus sublimated under vacuum (<100 mTorr) for 17 h at a temperature of 0°C. After equilibrating at room temperature, the porous scaffolds were removed from the molds and crosslinked by a dehydrothermal process (DHT) at 105°C and 30 mmHg for 24 h. This treatment leads to the formation of covalent linkages among the polypeptide chains of the collagen fibers without denaturing the collagen into gelatin.[24,25]

TABLE I
Experimental Groups

	Collagen Concentration (% w/v)	Freezing Temperature
Group I	2	−40°C[a]
Group II	0.5	−40°C
Group III	2	LN_2[a]
Group IV	0.5	LN_2

Four experimental groups of matrices were obtained by changing the collagen concentration and the freezing temperature.

[a]The collagen suspension in groups I and II were frozen by directly placing the copper-fitted end of the plastic mold onto the shelf of the freeze-dryer, precooled at −40°C; for Group III and IV, the freezing was achieved by placing the mold onto a copper plate, previously cooled with liquid nitrogen (LN_2).

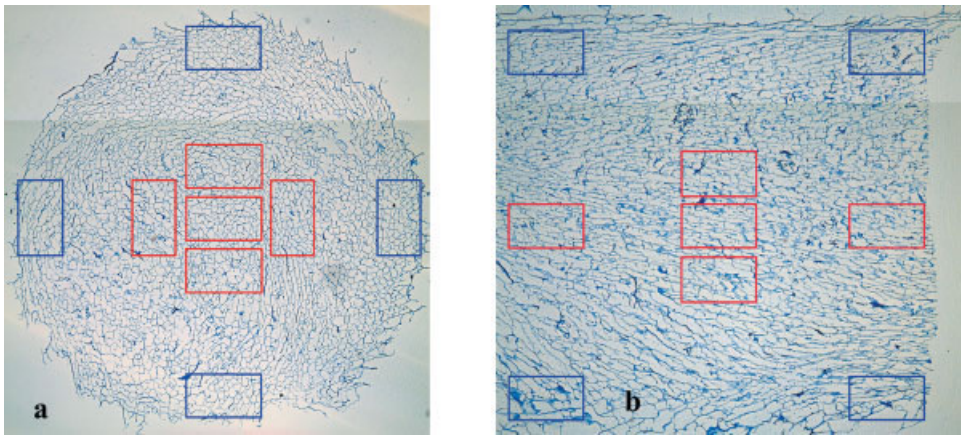

Figure 1. Number and location of the high magnification (×20) pictures taken to determine the mean pore size [cross-sectional view a)] and the mean pore orientation [longitudinal view (b)] in the central and peripheral areas (red and blue colours respectively). The images on the background are the light micrographs (×4) obtained for a sample of group I. [Color figure can be viewed in the online issue, which is available at www.interscience.wiley.com.]

In view of the intended implantation of the matrices into a 5-mm long defect in the adult rat spinal cord,[12] the crosslinked scaffolds were cut into 5-mm long cylinders using a razor blade. One 5-mm long sample was obtained from each mold. The cylindrical scaffolds received two transverse cuts at distances of 3 and 8 mm from the bottom, respectively. Both ends of the scaffolds resulting from the cuts were discarded.

Environmental scanning electron microscopy

Qualitative examination of the pore structure was carried out by means of ESEM. ESEM (XL30, FEI, Hillsboro, OR) was performed on noncoated samples (i.e., without a conductive coating, which may have obscured fine features). ESEM micrographs of transverse and longitudinal sections were taken at selected locations throughout the length of the scaffolds. A preliminary ESEM analysis was performed on the entire length of the scaffolds (15 mm) by observing the longitudinal section at distances of 2, 5, 7, 10, and 12 mm from the bottom (e.g., Fig. 2 for group III). Cross-sectional micrographs were then taken at distances of 3, 5.5, and 8 mm from the bottom, corresponding respectively to the lower end, middle section, and upper end of the 5-mm long matrices chosen for further characterization. The morphology of the external surface of the scaffolds, considered an important parameter in view of future plans to seed the scaffolds *in vitro* with cells, was also visualized by ESEM.

Quantitative light microscopy evaluation of pore characteristics

Transverse sections through the middle of the 5-mm long scaffolds were analyzed by means of optical microscopy to determine the mean pore diameter and the aspect ratio of the pores. Longitudinal sections through the upper 2.5 mm length of the scaffolds were used for the evaluation of the mean pore orientation. A total of six samples for each experimental group, obtained from at least two different batches of synthesis, were processed and analyzed as described below.

Specimens allocated for light microscopy were embedded in glycol methacrylate (JB-4, Polysciences, Warrington, PA), according to manufacturer's instructions. To avoid any shrinkage of the porous structure during the infiltration of the liquid resin, the samples were previously incubated into 100% alcohol overnight and then equilibrated into a 50% alcohol-50% JB-4 solution before starting the embedding procedure. The embedded specimens were then sectioned at 5 μm thickness with a microtome and mounted onto standard glass microscope slides. Before being cover-slipped, the sections were stained with aniline blue to enhance the contrast between the background and the collagen fibers under the optical microscope.

Images of the sections were taken at low (4× objective lens) and high magnification (20×) using an Olympus BX51 light microscope (Olympus Optical, Tokyo, Japan). The low magnification micrographs were captured to provide a wider view of the porous structure, thus allowing an estimation of the homogeneity and distribution of the pores throughout the entire section. For both the transverse and longitudinal sections, two different areas were then analyzed from high magnification pictures: (1) the peripheral area was defined as the outer 400 μm of the scaffold diameter; and (2) the central area was defined as the area covering the central 1.2 mm of the scaffold diameter. The mean pore diameter and pore orientation of the scaffold are here defined as the pore diameter and the pore orientation calculated from the analysis of the central zone. Figure 1 shows the number and the location of the high magnification pictures captured for the analysis of the transverse and longitudinal sections, respectively.

A total of at least 100 pores for each region were considered for the evaluation of the various pore parameters. The linear intercept method, often employed for the evaluation of the mean pore diameter of porous materials,[26,27] was applied here to determine the mean diameter, pore aspect ratio, and the orientation of pores using Scion Image Analysis 4.0.3 software (Scion Corporation, Frederick, MD).

Pore diameter

A linear intercept macro written for the Scion Image software involved the construction of an ellipse that best fits the mean cross-section of a pore, for each image analyzed. Briefly, the program consisted in scanning each image with an array of equidistant parallel test lines and determining the number of intersections between the lines and a pore wall. This procedure was repeated by rotating the array of parallel lines at 5° increments, and the angles and corresponding distances thus measured were finally used to plot a best-fit ellipse representing the average pore cross-section for each analyzed region. The major and minor axes of the ellipse, a and b, were calculated to define the mean pore diameter (D) and aspect ratio (AR) as:

$$D = 1.5 \times 2 \times \sqrt{\frac{a^2 + b^2}{2}} \quad (1)$$

$$\mathrm{AR} = \frac{\max(a, b)}{\min(a, b)} \quad (2)$$

In the calculation of the pore diameter [Eq. (1)], a correction factor of 1.5 was employed to account for the effect of pores that might not have been sectioned through their maximum diameter.[26,27]

Pore orientation

When analyzing the micrographs of longitudinal sections of the scaffolds, the angle of orientation of the best-fit ellipse, obtained from the linear intercept analysis, was calculated and assumed to be representative of the mean pore orientation in each image. The orientation of the pores was expressed in terms of an orientation index (OI) defined as follows:

$$\mathrm{OI} = 2\cos^2 \beta - 1 \quad (3)$$

where β is the average angle formed between the pore channel axis and the scaffold longitudinal axis.[15]

From the above definition, OI is equal to -1 in the limit of radial orientation ($\beta = 90°$) and equal to 1 in the limit of axial orientation ($\beta = 0°$).

Pore volume fraction and specific surface area

The pore volume fraction of the scaffold, V_f, was calculated according to the following:

$$V_f = 1 - \frac{V_c}{V_t} = 1 - \frac{m}{\rho} \quad (4)$$

where V_c, volume occupied by the collagen; V_t, total volume of the scaffold; ρ, density of anhydrous collagen, assumed to be 1.3 g/mL[27]; and m, mass of collagen per unit volume, i.e. the concentration of collagen used in suspension.

The specific surface area, or surface area per unit volume (SAV), is an important parameter as it may reflect the cell ligand density and thus one feature of the "biological activity" of a scaffold, in terms of cell attachment capability.[27] An approximation of the SAV was carried out employing a simplified model of the porous structure. In this model, the collagen scaffold was assumed to be formed by pore channels or pipes, with a diameter equal to the mean pore diameter of the scaffold and a length equal to that of the scaffold.[9] The number of pores contained in each transverse section was then calculated by dividing the cross-sectional area of the scaffold by the cross-sectional area of a pore. Considering both the inner and outer surfaces of each pore channel, the SAV can be calculated as follows:

$$\mathrm{SAV} = \frac{4R_{\mathrm{pore}}N}{R^2_{\mathrm{scaffold}}} = \frac{4}{R_{\mathrm{pore}}} \quad (5)$$

where R_{pore}, mean pore radius; N, number of pores in cross-section; and R_{scaffold}, radius of the scaffold, equal to 1.5 mm.

This estimation, although rough, is a useful method to begin to appreciate the surface area of the scaffold available for cell attachment.[9]

Statistical analyses

All data are expressed as means ± the standard deviation (SD). Two-factor analysis of variance (ANOVA) was applied to determine the effects of collagen concentration and freezing temperature on the pore size and orientation. A probability value of 95% ($p < 0.05$) was used as the criterion for significance.

RESULTS

Pore diameter

The mean pore diameter in cross-sections through the cylindrical scaffolds ranged from about 20 to 60 μm and varied with the collagen concentration in suspension and the temperature at which the suspension was frozen (Table II). There was an inverse relationship between pore diameter and collagen concentration, and smaller pore diameters were produced in samples frozen with LN_2 (Table II). Two-factor ANOVA demonstrated that both of these independent variables significantly affected the mean pore diameter of the central area of the scaffold cross-section ($p < 0.0001$; power = 1). Preliminary ESEM micrographs demonstrated a variation of pore characteristics along the full length (15 mm) of the original scaffolds (e.g., Fig. 2 for group III). However, the pore diameter and orientation did not appear to change noticeably in the lower half of the scaffolds, along the 5-mm length chosen to be representative for the matrices studied here [Fig. 2(b,c)]. Cross-sections corresponding to the middle cross-sections of the 5-mm matrices were assumed representative of the mean pore size of the scaffold and analyzed.

TABLE II
Pore Diameter and Aspect Ratio in Cross-Sections of the Cylindrical Scaffolds

	Central Area		Peripheral Area	
	Pore Size (μm)	Aspect Ratio	Pore Size (μm)	Aspect Ratio
Group I (2%, −40°C)	40 ± 1	1.15 ± 0.08	52 ± 15	1.11 ± 0.11
Group II (0.5%, −40°C)	62 ± 8	1.11 ± 0.04	55 ± 16	1.10 ± 0.10
Group III (2%, LN_2)	23 ± 2	1.06 ± 0.08	32 ± 6	1.11 ± 0.09
Group IV (0.5%, LN_2)	33 ± 5	1.11 ± 0.09	30 ± 5	1.11 ± 0.09

Pore size and pore aspect ratio, measured in the peripheral (outer 400 μm) and central (inner 1.2 mm of the scaffold diameter) areas of the scaffolds.

Results are expressed as means ± the standard deviation of the mean ($n = 6$).

Both collagen concentration and freezing temperature affect significantly the mean pore size ($p < 0.0001$).

Larger values of pore diameter were observed in the peripheral zone of the scaffold when compared with the central zone for groups I and III (Table II). The results for groups II and IV (Table II) were not considered reliable because the compliance of the samples, in spite of the crosslinking treatment, allowed their collapse during the processing (scaffold embedding and cutting), thus compromising the pore structure. Moreover, when comparing peripheral and central zones, it is worth noting that the peripheral zone displayed larger coefficients of variation, indicating a wider distribution of pore diameters (Table II).

The aspect ratio of the pores, related to the pore morphology, was not significantly affected by either the collagen concentration or the freezing temperature (Table II), and was close to 1 for all the experimental groups, suggesting that the uniaxial freezing of the collagen slurry described here resulted in the formation of nearly circular pores. This morphological result was also confirmed by qualitative analysis of ESEM cross-sectional micrographs.

Pore orientation

Light micrographs of longitudinal sections through the upper half of the 5-mm long scaffolds were analyzed to determine the mean pore orientation (Table III), as described previously for the calculation of OI and the angle of orientation. The mean pore orientations of the four experimental groups were not statistically different, indicating that the concentration of collagen in suspension and the freezing temperature

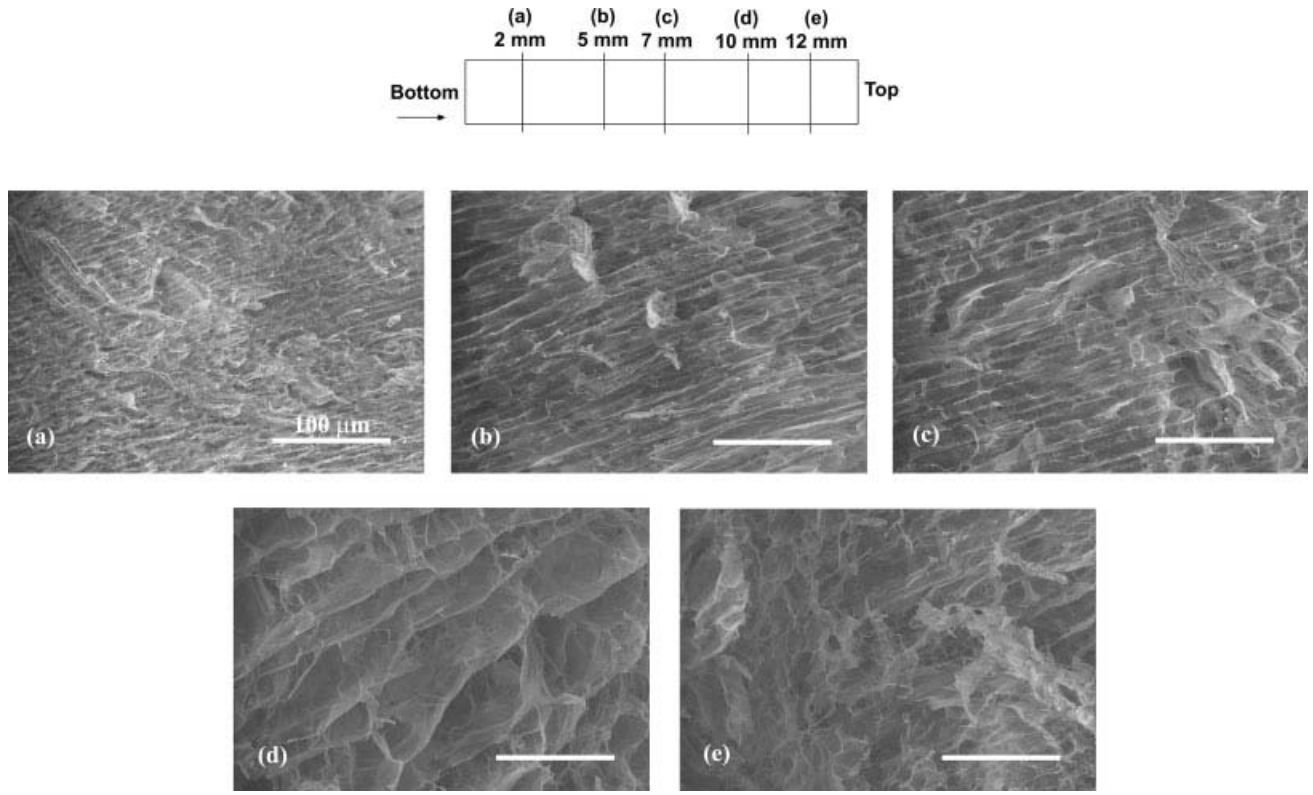

Figure 2. ESEM micrographs of a longitudinal section taken at 5 different locations along the length of the scaffold (group III). The micrographs were taken at distances of 2, 5, 7, 10, 12 mm from the bottom of the scaffold [images from (a)–(e), respectively]. The magnification is ×350 and the scale bar is 100 μm. In the pictures the orientation of the pore channels is parallel to the axis of the cylindrical matrix.

TABLE III
Pore Orientation

	Central Area		Peripheral Area	
	OI	Angle (degree)	OI	Angle (degree)
Group I (2%, −40°C)	0.92 ± 0.07	10.2 ± 4.8	0.80 ± 0.09	16.3 ± 4.6
Group II (0.5%, −40°C)	0.89 ± 0.11	11.4 ± 6.4	0.80 ± 0.19	13.8 ± 8.6
Group III (2%, LN_2)	0.77 ± 0.37	15.2 ± 13.3	0.55 ± 0.37	26.4 ± 13.5
Group IV (0.5%, LN_2)	0.94 ± 0.05	8.9 ± 3.8	0.89 ± 0.11	9.6 ± 6.7

Pore orientation expressed in terms of OI (mean ± the standard deviation of the mean; $n = 6$).
β is the angle formed between the axis of the pore channels and the longitudinal axis of the cylindrical scaffold.
The orientation in the central area is nearly axial for all the experimental groups; the peripheral area is slightly more radially oriented compared with the central one.

did not significantly affect the direction of growth of ice crystals during the freezing of the collagen slurry (two-factor ANOVA for collagen concentration and temperature, $p = 0.40$ and $p = 0.54$ respectively). The OI in the central area ranged from about 0.8 to 0.9, indicating a predominantly axial pore orientation resulting from an axial freezing process. Large coefficients of variation for OI in groups II and III, and a non-normal distribution of the data for OI in group III were observed (Table III).

As found for the central pore orientation, the collagen concentration and the freezing temperature did not affect significantly the orientation of the pore channels in the peripheral area ($p = 0.08$ and 0.37, respectively). For each experimental group, the mean values of OI were lower than those yielded in the central area (Table III), suggesting that the peripheral pores might be slightly more radially oriented, if compared with the pores found in the central zone. Figure 3 demonstrates the low magnification (4×)

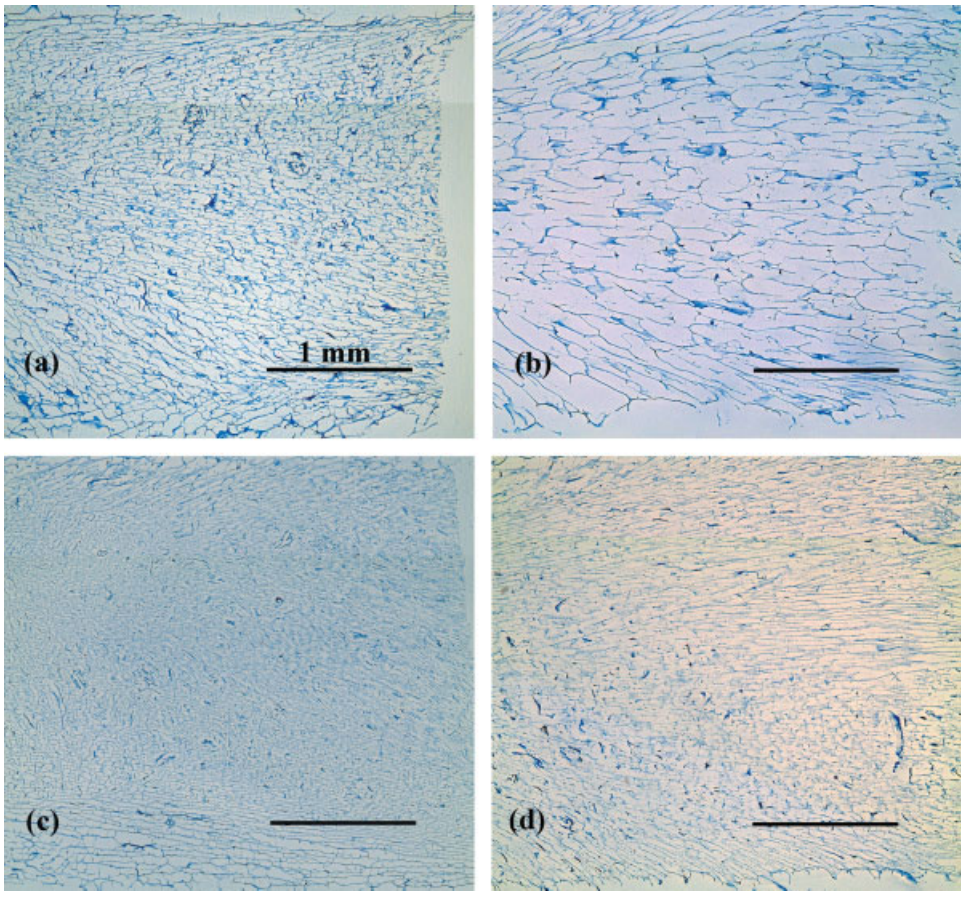

Figure 3. Longitudinal views (×4) of samples of the four experimental groups: (a) group I; (b) group II; (c) group III; (d) group IV. The micrographs report the upper half of the 5-mm-long matrices. [Color figure can be viewed in the online issue, which is available at www.interscience.wiley.com.]

TABLE IV
Pore Volume Fraction and Surface Area

	Pore Volume Fraction (%)	Specific Surface Area (mm^2/mm^3)
Group I (2%, −40°C)	98.4	200
Group II (0.5%, −40°C)	99.5	133
Group III (2%, LN_2)	98.4	400
Group IV (0.5%, LN_2)	99.5	250

Values of pore volume fraction and specific surface area, calculated according to Eqs. (4) and (5), respectively.

The value of specific surface area is referred to the mean pore diameter measured for the central area of the four experimental groups.

micrographs representing the typical longitudinal pore structure obtained for each experimental group.

Pore volume fraction and SAV

The pore volume fraction calculated according to Eq. (4) was a function only of the collagen concentration, and it was 98.4% for groups I and III (2% w/v collagen) and 99.5% for groups II and IV (0.5% w/v collagen), as reported in Table IV.

The values of the SAV were calculated according to Eq. (5), and are also listed in Table IV for each different mean pore size obtained for the four experimental groups. As mentioned above, the mean pore size of the matrices resulted from an analysis of the central area of the scaffold (inner 1.2 mm). The group III scaffolds, with the smallest pore diameter correspondingly (20 μm), had the highest SAV.

ESEM analysis

A qualitative ESEM analysis on transverse and longitudinal sections has been performed to detect the morphology of the pore structure and its homogeneity throughout the scaffold. A preliminary study was focused on the analysis of the pore characteristics along the full length (15 mm) of the cylindrical matrices. Longitudinal pore channels could be observed throughout the samples, and increasing pore diameters were detected going from the bottom to the top of the scaffolds (Fig. 2). However, the pore size and the pore orientation appeared to be more uniform in the lower half of the scaffold length, when compared with the upper one [Fig. 2(b,c) vs. Fig. 2(d,e)]. Therefore, the original scaffolds were cut at distances of 3 and 8 mm from the bottom, respectively, to obtain the 5-mm long matrices characterized here. Cross-sectional micrographs representing the two ends of the 5-mm matrices confirmed the uniformity of pore size along the selected length (e.g., Fig. 4 for group I).

ESEM pictures of the external longitudinal surface of the matrices were taken to estimate the surface morphology, a feature that is expected to be particularly important in processes in which the matrices are seeded *in vitro* with exogenous cells. For all groups analyzed, the external surface seems to reflect the axial pore orientation observed in longitudinal sections (e.g., Fig. 5 for groups I and IV). It is worth noting also that the pore walls change from lamellar to fibrillar as the collagen concentration is decreased.

DISCUSSION

This work focused on the fabrication of cylindrical collagen scaffolds with axially oriented pores to be used as nerve guidance scaffolds in the context of an entubulation strategy. The use of a porous, oriented scaffold may facilitate nerve regeneration in the central nervous system as it has already been shown to do in the peripheral nervous system. In addition, the oriented scaffold may also be used as a delivery vehicle for exogenous cells, growth factors, and genes

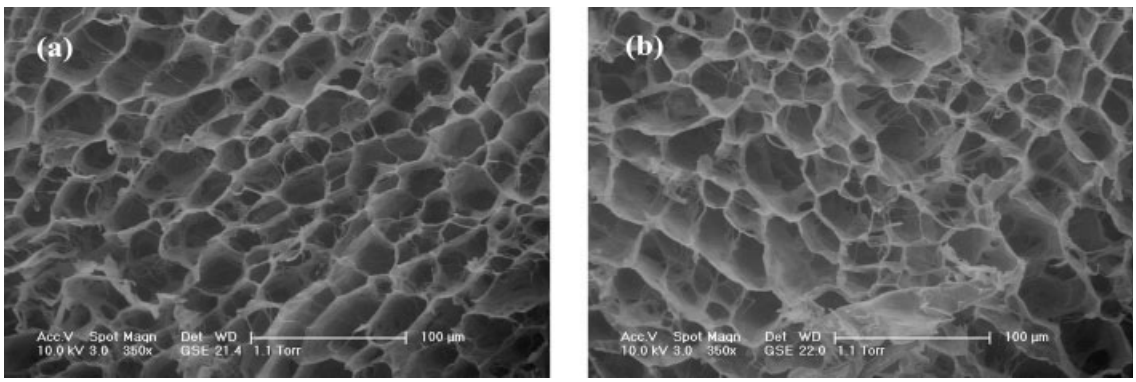

Figure 4. ESEM micrographs of the two cross-sections representing the two ends of a 5-mm-long scaffold (group I): (a) lower end, resulting by cutting the original matrix at a distance of 3 mm from the bottom; (b) upper end, resulting by cutting the original matrix at a length of 8 mm from the bottom. The magnification is ×350 and the scale bar is 100 μm.

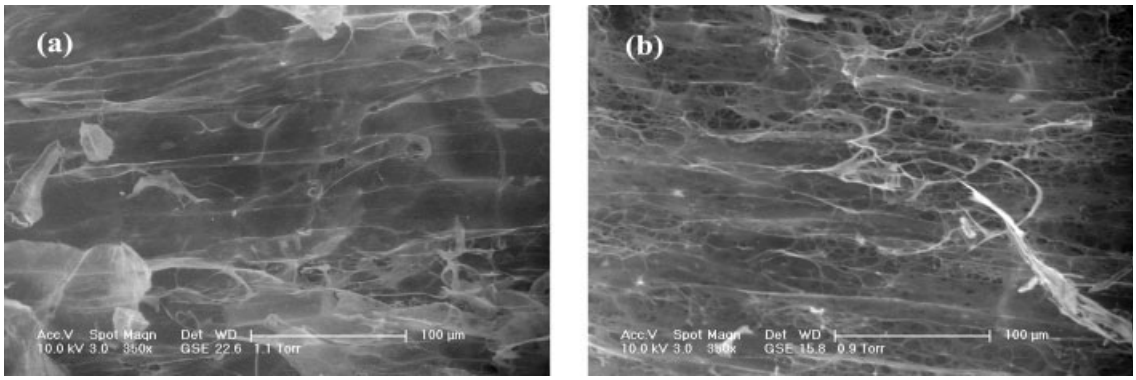

Figure 5. ESEM micrographs of the external longitudinal surface of the scaffolds: (a) group I; (b) group IV. The magnification is ×350 and the scale bar is 100 μm.

in cases where the regenerative response induced by the scaffold alone is insufficient, as observed in numerous studies targeting the regeneration of the spinal cord. Therefore, not only pore orientation, but also pore size, pore volume fraction, and resulting surface area available for cell attachment need to be controlled by the scaffold manufacturing method.

Several fabrication techniques for the production of scaffolds with longitudinally oriented pores have been reported to date, including fiber templating,[28] porogen leaching,[29] injection molding and solvent evaporation,[4] microfilament alignment,[30] and wire-heating.[31] Most of these manufacturing methods are based on the use of additional chemicals and/or polymeric fibers or metal wires, which are incorporated into the scaffold architecture and then removed, for example through solvents or thermal separation processes, to obtain the desired pore structure. Control of the pore diameter and pore volume fraction is achieved by varying the porogen concentration or the diameter and number of fibers used. Despite the success achieved in producing oriented scaffolds, the complexity of the fabrication process itself and the use of chemicals that might compromise the scaffold biocompatibility prompt the need for novel manufacturing technologies.

In this study, we produced collagen-based matrices with axially oriented pores by implementing a simple technique that is based on the control of ice crystal growth that takes place during the freezing of a collagen suspension. A longitudinal and uniaxial gradient of temperature is established throughout the collagen slurry so that ice crystals can grow longitudinally. A subsequent freeze drying process, by which ice is sublimated, leads to the formation of linearly oriented pore channels in a collagen sponge-like scaffold, without requiring the use of additional chemicals. The control of the pore diameter and pore volume fraction is easily performed by varying selected parameters affecting ice formation during freezing, such as the freezing temperature and the collagen concentration used in suspension.

A similar approach has been reported in the literature for the formation of axially oriented pores into agarose-based scaffolds.[5,17] A fixed agarose concentration (3% w/v) and a particular freezing apparatus (a block of dry ice immersed in a pool of LN_2) were used to obtain linearly oriented pore channels with a mean pore diameter of about 120 μm. In the present study axial pores of different diameters, ranging from 20 to 60 μm, were obtained by varying both the temperature of freezing and the collagen concentration in the suspension. The much larger pore diameter achieved for the agarose-based scaffolds, compared with the collagen scaffolds described here, may be because of the difference in thermal conductivities of materials that were employed during the freezing process. In the work by Stokols and Tuszynski, a glass[17] or plastic[5] mold containing the agarose solution was directly placed onto a block of dry ice, without the use of a metal base as heat conductor. Here copper caps were fitted into the cylindrical holes of the plastic mold before injecting the collagen slurry to enhance the heat transfer process between the mold and the cooling plate (either a copper plate pre-cooled with LN_2 or the freeze-dryer shelf at $-40^{\circ}C$) during the subsequent freezing process. The actual freezing temperature of the agarose solution might be higher than those obtained in this work, yielding larger pores.

In this study, both the freezing temperature and the collagen concentration were found to significantly affect the mean pore size of the collagen scaffolds. Since the porous structure obtained by the freeze-drying process is a negative replica of the ice crystal structure formed during the freezing phase, the single effects of collagen concentration and freezing temperature on the pore size can be explained in terms of ice crystal physics. As expected, a higher collagen concentration was found to yield smaller pores. Results obtained previously with CG scaffolds that were prepared via freeze-drying suggested that the higher viscosity of the collagen slurry resulting

from the increase of the collagen concentration might limit the rate of diffusion of water molecules, that is the rate of ice crystal growth, during the freezing process.[15] However, when studying the formation and growth of dendritic ice crystals in a steady-state freezing of a collagen suspension, Schoof et al.[32,33] observed a significant increase of the ice dendrite width when increasing the concentration of solute (e.g., acetic acid) in the collagen slurry, although they could not find a clear correlation between the pore channel width and the collagen concentration.[34] Further studies should therefore be addressed to clarify the effects of the collagen concentration on the pore size of the resulting freeze-dried scaffold.

With regard to the effect of different freezing temperatures on the ice crystal size, as expected lower temperatures of freezing yielded faster rates of ice crystal nucleation and lower rates of diffusion, and thus significantly smaller pores.[26] Indeed, the freezing rate is directly related to the magnitude of the temperature gradient across the ice front and the value of the ice front velocity.[34] In particular, since the collagen suspension is frozen starting at the bottom of the mold, a longitudinal gradient of temperature is established along the length of the cylindrical scaffold (15 mm). The upper layers of the slurry are expected to freeze at higher temperatures (i.e. larger pores) compared with the bottom layers, thus resulting in a gradient of pore sizes along the length of the scaffold.[18] ESEM micrographs confirmed the expected variation of pore sizes throughout the entire length of 15 mm, but did not show a significant change in pore diameter along the 5 mm length chosen for the scaffolds studied here (Figs. 2 and 4). Our findings confirmed and extended those by Yunoki et al.,[18] who recently reported the fabrication of hydroxyapatite/collagen composites with longitudinally oriented pores, with a mean pore size increasing along the thickness of the scaffolds.

As regards the longitudinal orientation of the pores, higher freezing temperatures were expected near the wall of the cylindrical mold into which the collagen suspension was injected, since the plastic mold was a thermal insulator. This peripheral temperature gradient leads to larger pore diameters in the peripheral area (Table II), and is also expected to be related to a heat transfer process at the wall of the mold. Such a process might explain the lower values of OI found at the periphery of the scaffolds when compared with the central region (Table III). However, the radial component of the heat flux is low compared with the axial component, and so that the overall freezing process becomes predominantly uniaxial.

Of interest is that this freeze-drying method might be adjusted to produce pores of various orientations in the same cylindrical specimen. Pores in the central region of the cylinder could be oriented axially whereas peripheral pores oriented radially. This may provide the opportunity to selectively seed peripheral pores with certain cell types, which could support regeneration of peripheral tissues, such as the epineurium, while allowing the central region to remain oriented to accommodate elongation of nerve fibers.

Of note was that a simple method could be employed to produce oriented pores in a collagen scaffold, with different pore sizes. The experimental evidence of an optimal range of pore diameter in several tissue engineering applications suggests that, while pores smaller than or close to the cell size physically prevent or limit cell infiltration, a mean pore diameter larger than a maximum value may not be sufficient to yield the minimum SAV required for an efficient cell binding.[27] The specific surface area or surface area per unit volume (SAV) for a given scaffold is a function of the bulk material (i.e., its chemical composition) and its architecture, in terms of pore size, pore interconnectivity, and pore volume fraction. Prior studies demonstrated that the optimal diameter of oriented pores for *in vivo* peripheral nerve regeneration was $\sim$20 μm for a CG sponge-like scaffold with a porosity of $\sim$99%,[10] and this finding directed the present study to encompass this pore diameter in the design specifications. Pores with diameters as small as 20 μm (group III scaffolds) could be effectively produced by controlling the collagen concentration and the temperature of the baseplate.

A linear relationship between SAV and the number of cells attached to the scaffold 24 h post-seeding has been documented in the literature for CG scaffolds with an equiaxed, that is, nonoriented, porosity, and a pore volume fraction of 99.5%.[27] In that study, the porous scaffold was modeled as an open-cell foam with a tetrakaidecahedral cell unit, and SAV was found to be inversely proportional to the pore diameter and directly proportional to the relative density or solid volume fraction of the scaffold. In the simplified approach adopted in the present study, the scaffold porosity was instead assumed to be closed, with membrane-like faces between adjacent pore channels. Thus the present model overestimates the actual surface area available for cell attachment by neglecting the actual interconnectivity between longitudinal pores [e.g., Fig. 5(b)] and the effect of the solid volume fraction. However, since an increase in collagen concentration changes the pore wall structure from fibrillar to lamellar [Fig. 5(a,b)], the closed-pore model here proposed is likely to estimate the surface area of high-density, oriented scaffolds more accurately than that of an open-cell foam. It is worth noting also that the observed dependence of the pore diameter on the collagen concentration suggests that, in both models,

increasing values of SAV are expected for higher collagen concentrations.

The group III scaffolds with the smallest pore diameter (20 μm) had the highest value of SAV, according to Eq. (5). However, the pore size might be too small to allow satisfactory infiltration of these scaffolds with mesenchymal or neural stem cells. Matrices in group I, II, and IV that have pore sizes of about 40, 62, and 33 μm, respectively, are more likely to be amenable to act as hosts for cells. Preliminary seeding experiments with adult rat mesenchymal and neural stem cells are currently being performed on group I scaffolds. Indeed, although matrices of group IV present a higher value of SAV than those of group I, their low solid volume fraction (0.5%) gives them poor mechanical properties compared with group I (1.6%), making their handling during cell seeding more delicate. However, future studies should be directed to investigate the effect of different collagen concentrations and cross-linking treatments on the stiffness of the oriented scaffolds, and to find out if and how scaffold stiffness can affect stem cell behavior *in vitro*.

CONCLUSIONS

A simple method to produce collagen matrices with nearly axially oriented pores has been presented. Longitudinally oriented pore channels have been successfully obtained by axial freezing of a collagen suspension and subsequent freeze-drying. Scaffolds with a diameter of 3 mm and a length of 5 mm have been produced and characterized in view of their potential application as nerve guidance matrices for the regeneration of the spinal cord in a rat model. The longitudinal pore orientation, quantified by means of an OI, is expected to support and guide the regeneration of axons across the site of injury. Moreover, different pore diameters, which may be suitable to support axonal elongation *in vivo* or the seeding of exogenous cells *in vitro*, have been obtained by changing the concentration of collagen in suspension and the temperature at which the suspension is frozen. The seeding of the linearly oriented matrices with mesenchymal and neural stem cells, which have the potential to enhance the regenerative process after spinal cord injury, is currently investigated.

The authors would like to thank Chen Ma, Paola Castellazzi and Rahmat Cholas for technical assistance.

References

1. Chamberlain LJ, Yannas IV, Hsu HP, Strichartz G, Spector M. Collagen-GAG substrate enhances the quality of nerve regeneration through collagen tubes up to level of autograft. Exp Neurol 1998;154:315–329.
2. Chamberlain LJ, Yannas IV, Hsu HP, Strichartz GR, Spector M. Near-terminus axonal structure and function following rat sciatic nerve regeneration through a collagen-GAG matrix in a ten-millimeter gap. J Neurosci Res 2000;60:666–677.
3. Yannas IV. Tissue and Organ Regeneration in Adults. New York: Springer; 2001.
4. Moore MJ, Friedman JA, Lewellyn EB, Mantila SM, Krych AJ, Ameenuddin S, Knight AM, Lu L, Currier BL, Spinner RJ, Marsh RW, Windebank AJ, Yaszemski MJ. Multiple-channel scaffolds to promote spinal cord axon regeneration. Biomaterials 2006;27:419–429.
5. Stokols S, Tuszynski MH. Freeze-dried agarose scaffolds with uniaxial channels stimulate and guide linear axonal growth following spinal cord injury. Biomaterials 2006;27:443–451.
6. Oudega M, Gautier SE, Chapon P, Fragoso M, Bates ML, Parel JM, Bunge MB. Axonal regeneration into Schwann cell grafts within resorbable poly(alpha-hydroxyacid) guidance channels in the adult rat spinal cord. Biomaterials 2001;22: 1125–1136.
7. Hurtado A, Moon LD, Maquet V, Blits B, Jerome R, Oudega M. Poly (D,L-lactic acid) macroporous guidance scaffolds seeded with Schwann cells genetically modified to secrete a bi-functional neurotrophin implanted in the completely transected adult rat thoracic spinal cord. Biomaterials 2006;27:430–442.
8. Teng YD, Lavik EB, Qu X, Park KI, Ourednik J, Zurakowski D, Langer R, Snyder EY. Functional recovery following traumatic spinal cord injury mediated by a unique polymer scaffold seeded with neural stem cells. Proc Natl Acad Sci USA 2002;99:3024–3029.
9. Chang AS. Electrophysiological recovery of peripheral nerves regenerated by biodegradable polymer matrix. MS Thesis. Department of Mechanical Engineering, Massachusetts Institute of Technology. 1988. 90 p.
10. Chang AS, Yannas IV, Krarup C, Sethi RR, Norregaard TV, Zervas NT. Polymeric templates for peripheral nerve regeneration. Electrophysiological study of functional recovery. Proc ACS Div Polym Mater Sci Eng 1988;59:906–910.
11. Chang AS, Yannas IV, Perutz S, Loree H, Sethi RR, Krarup C, Norregaard TV, Zervas NT, Silver J. Electrophysiological study of recovery of peripheral nerves regenerated by a collagen-glycosaminoglycan copolymer matrix. In: Gebelein CG, editor. Progress in Biomedical Polymers. New York: Plenum; 1990.
12. Spilker MH, Yannas IV, Hsu HP, Spector M. The effects of tubulation on healing and scar formation after transection of the adult rat spinal cord. Restor Neurol Neurosci 2001;18:23–38.
13. Louie LK.Effect of a porous collagen-glycosaminoglycan copolymer on early tendon healing in a novel animal model. Ph. D Thesis. Department of Materials Science and Engineering, Massachusetts Institute of Technology. 1997. 196 p.
14. Dagalakis N, Flink J, Stasikelis P, Burke JF, Yannas IV. Design of an artificial skin. Part III. Control of pore structure. J Biomed Mater Res 1980;14:511–528.
15. Loree HM. A freeze-drying process for fabrication of polymeric bridges for peripheral nerve regeneration. MS Thesis. Department of Mechanical Engineering, Massachusetts Institute of Technology, 1988. 106 p.
16. Loree HM, Yannas IV, Mikic B, Chang AS, Perutz SM, Norregaard TV, Krarup C. A Freeze-drying process for fabrication of polymeric bridges for peripheral nerve regeneration. Proceedings of 15th Annual Northeast Bioengineering Conference, 1989. p 53–54.
17. Stokols S, Tuszynski MH. The fabrication and characterization of linearly oriented nerve guidance scaffolds for spinal cord injury. Biomaterials 2004;25:5839–5846.

18. Yunoki S, Ikoma T, Monkawa A, Ohta K, Kikuchi M, Sotome S, Shinomiya K, Tanaka J. Control of the pore structure and mechanical property in hydroxyapatite/collagen composite using unidirectional ice growth. Mater Lett 2006;60:999–1002.
19. Horner PJ, Gage FH. Regenerating the central nervous system. Nature 2000;407:963–970.
20. Moses O, Pitaru S, Artzi Z, Nemcovsky CE. Healing of dehiscence-type defects in implants placed together with different barrier membranes: A comparative clinical study. Clin Oral Implants Res 2005;16:210–219.
21. Oh TJ, Meraw SJ, Lee EJ, Giannobile WV, Wang HL. Comparative analysis of collagen membranes for the treatment of implant dehiscence defects. Clin Oral Implants Res 2003;14:80–90.
22. Schlegel AK, Mohler H, Busch F, Mehl A. Preclinical and clinical studies of a collagen membrane (Bio-Gide). Biomaterials 1997;18:535–538.
23. Tawil G, El-Ghoule G, Mawla M. Clinical evaluation of a bilayered collagen membrane (Bio-Gide) supported by autografts in the treatment of bone defects around implants. Int J Oral Maxillofac Implants 2001;16:857–863.
24. Yannas IV, Tobolsky AV. Cross-linking of gelatine by dehydration. Nature 1967;215:509–510.
25. Yannas IV. Collagen and gelatin in the solid state. J Macromol Sci Revs Macromol Chem 1972;C7:49–104.
26. O'Brien FJ, Harley BA, Yannas IV, Gibson L. Influence of freezing rate on pore structure in freeze-dried collagen-GAG scaffolds. Biomaterials 2004;25:1077–1086.
27. O'Brien FJ, Harley BA, Yannas IV, Gibson LJ. The effect of pore size on cell adhesion in collagen-GAG scaffolds. Biomaterials 2005;26:433–441.
28. Flynn L, Dalton PD, Shoichet MS. Fiber templating of poly (2-hydroxyethyl methacrylate) for neural tissue engineering. Biomaterials 2003;24:4265–4272.
29. Lin ASP, Barrows TH, Cartmell SH, Guldberg RE. Microarchitectural and mechanical characterization of oriented porous polymer scaffolds. Biomaterials 2003;24:481–489.
30. Cai J, Peng X, Nelson KD, Eberhart R, Smith GM. Permeable guidance channels containing microfilament scaffolds enhance axon growth and maturation. J Biomed Mater Res A 2005;75:374–386.
31. Huang YC, Huang YY, Huang CC, Liu HC. Manufacture of porous polymer nerve conduits through a lyophilizing and wire-heating process. J Biomed Mater Res B Appl Biomater 2005;74:659–664.
32. Schoof H, Bruns L, Fischer A, Heschel I, Rau G. Dendritic ice morphology in unidirectionally solidified collagen suspensions. J Crystal Growth 2000;209:122–129.
33. Schoof H, Apel J, Heschel I, Rau G. Control of pore structure and size in freeze-dried collagen sponges. J Biomed Mater Res (Appl Biomater) 2001;58:352–357.
34. Kuberka M, Von Heimburg D, Schoof H, Heschel I, Rau G. Magnification of the pore size in biodegradable collagen sponges. Int J Artif Organs 2002;25:67–73.

Delivery of plasmid IGF-1 to chondrocytes via cationized gelatin nanoparticles

Ximing Xu,[1,2,3] Ramille M. Capito,[1,4] Myron Spector[1,3]
[1]*Tissue Engineering, VA Boston Healthcare System, Boston, Massachusetts 02130*
[2]*Department of Pharmaceutics, School of Pharmacy, Jiangsu University, Zhenjiang, Jiangsu 212001, People's Republic of China*
[3]*Department of Orthopedic Surgery, Brigham and Women's Hospital, Harvard Medical School, Boston, Massachusetts 02115*
[4]*Department of Materials Science and Engineering, Massachusetts Institute of Technology, Cambridge, Massachusetts 02139*

Received 27 September 2006; revised 6 November 2006; accepted 8 February 2007
Published online 28 June 2007 in Wiley InterScience (www.interscience.wiley.com). DOI: 10.1002/jbm.a.31372

Abstract: The objective of the present study was to investigate the use of gelatin and cationized-gelatin nanoparticles for the nonviral delivery of the plasmid DNA encoding for insulin-like growth factor (IGF)-1 to adult canine articular chondrocytes *in vitro*; plasmid for enhanced green fluorescence protein (EGFP) was used as a marker gene. The spherical cationized gelatin nanoparticles were on average 172 nm in diameter, compared with the often ellipsoid-shaped unmodified (noncationized) gelatin particles that generally appeared to be 10 μm to greater than 20 μm in length. The zeta potential of the positively charged cationized gelatin nanoparticles containing the plasmid was around 20 mV compared with about 2 mV for the unmodified gelatin particles. There was no noticeable fluorescence from the cells treated with the nanoparticles prepared with the original (noncationized) gelatin particles containing the pEGFP. In contrast, numerous cells in the group transfected with the cationized gelatin-pEGFP nanoparticles were found to fluoresce demonstrating the transfection of the cells. There was five-fold elevation in the amount of IGF-1 produced by the cells treated with the cationized gelatin nanoparticles containing the IGF-1 plasmid compared with the unmodified (noncationized) gelatin particles. There was a clear effect of varying the weight ratio of plasmid IGF-1 in the cationized gelatin nanoparticles on the IGF-1 in the medium of cells exposed to the nanoparticles for 5 h. A peak in the amount of released IGF-1 was detected at a gelatin:IGF-1 weight ratio of 250:1. © 2007 Wiley Periodicals, Inc. J Biomed Mater Res 84A: 73–83, 2008

Key words: gelatin; nanoparticles; IGF-1; chondrocytes

INTRODUCTION

It has become increasingly clear that a number of tissue engineering applications would benefit from the administration of selected growth factors in conjunction with a biomaterial scaffold.[1–4] The delivery of recombinant growth factors *in vivo*, however, either by bolus injection or by delivery from a biomaterial may have a limited effect because of the short half-life of the protein. One approach being investigated for prolonged overexpression of growth factors by cells *in vivo* is the incorporation of gene vectors into 3D scaffolds.[5–7] In an effort to implement the safest methodology for wedding gene therapy and tissue engineering, several studies have focused on the incorporation of nonviral vectors directly into the scaffold.[8,9] An alternative approach is to encapsulate plasmid DNA containing the gene encoding for the selected growth factor into nanoparticles, which can be injected or implanted along with or bound to a scaffold prior to its implantation. The benefit in using nanoparticles as gene delivery vehicles is the capability to easily direct and control gene expression kinetics by altering various processing parameters used to make the nanoparticles. A wide array of materials is undergoing investigation as nanoparticle delivery vehicles for plasmid DNA. Because our own work has employed collagen-based scaffolds,[10,11] we were prompted to investigate gelatin nanoparticles for this application. Gelatin, the water-soluble molecular chain resulting from the

Correspondence to: M. Spector; e-mail: mspector@rics.bwh.harvard.edu

Contract grant sponsor: Rehabilitation Research and Development Service, U.S. Department of Veterans Affairs

heat dissolution and partial hydrolysis of collagen, has been investigated for the production of nanoparticles for drug delivery for almost three decades.[12,13]

While gelatin nanoparticles were initially introduced as carriers for small molecular weight drugs[14,15] they were later investigated as carriers for peptides.[16] More recently gelatin nanoparticles have been studied as delivery vehicles for DNA.[17–21] Issues related to the use of gelatin nanoparticles for these applications include: size distribution,[19] charge,[22] stability, and reproducibility. Methods for producing gelatin nanoparticles[23] include: solvent evaporation techniques[24]; water-in-oil emulsion[25,26]; complex coacervation[17]; and an emulsifier-free emulsion method.[16] While all of these methods can be employed to incorporate small molecules into gelatin nanoparticles, a few are particularly useful for incorporating large molecules such as plasmid DNA. The advantage of complex coacervation, which is the separation caused by interaction of two oppositely charged colloids, is that it is simple and quick, and leads to the condensation of plasmid DNA.[17]

Gelatin is ideal for nanoparticle formation due to its versatility to be chemically modified and crosslinked to meet specific controlled release needs. In one case thiolated gelatin nanoparticles were developed to release the incorporated molecules in a highly reducing environment.[27] In other studies, DNA-containing poly(ethylene glycol)-modified (PEGylated) gelatin nanoparticles were synthesized.[28] for applications including the systemic administration of nonviral gene therapy vectors for solid tumors.[29,30] Still other applications benefited from the modification of the surface of gelatin nanoparticles by covalent attachment of biotin-binding proteins, enabling the binding of biotinylated drug targeting ligands by avidin–biotin-complex formation.[31–33] Antibody modified gelatin nanoparticles have also been used as drug carrier systems to target nanoparticles to specific cell types.[34] Of particular interest is the modification of the charge (increased positivity) of gelatin by cationization.[19] Cationized gelatin nanoparticles have been used for a myriad of applications[18,35–39] that benefit from the increased positive charge on the gelatin nanoparticles. As delivery vehicles for plasmid DNA, positively charged gelatin nanoparticles could be capable of condensing DNA and favoring interactions with the negatively charged cell membrane to facilitate endocytosis.

The objective of the present study was to investigate the use of gelatin nanoparticles for nonviral delivery of plasmid DNA containing the gene encoding for insulin-like growth factor (IGF)-1 into adult articular chondrocytes *in vitro*, and to determine the behavior of transfected chondrocytes within collagen (type II)-glycosaminoglycan (CG) scaffolds[10,11] with regard to IGF-1 release over time and effects on biosynthesis. The ultimate goal would be to use such nanoparticles along with or incorporated into collagen scaffolds to result in a prolonged and localized release of IGF-1. IGF-1 was implemented in the study on the basis of prior *in vitro* and *in vivo* studies that have demonstrated its favorable effects on chondrogenesis. Supplementation of culture medium with IGF-1 alone has been shown to increase cell proliferation, proteoglycan synthesis, type-II collagen synthesis, and chondrogenesis, both in monolayer and in three-dimensional cultures.[40–45] In addition, the combination of IGF-1 and osteogenic protein (OP)-1 promoted increased survival of and matrix synthesis by normal and osteoarthritic human articular chondrocytes.[46] *In vivo* fibrin polymers laden with IGF-1 resulted in improved histologic appearance and increased proportion of type II collagen in full-thickness cartilage defects in young mature horses.[47] Moreover, *ex vivo* gene transfer of a human IGF-1 cDNA into chondrocytes was found to enhance chondrogenesis both *in vitro* and *in vivo*, in work directed toward cartilage tissue engineering.[48,49]

Our supposition is that the nanoparticles containing the plasmid would be taken up by cells seeded into the scaffold prior to implantation, or by endogenous cells migrating into the scaffold *in vivo*. Once inside the cells, the nanoparticles would release the plasmid, which would gain entry into the nucleus and enable the overexpression of IGF-1. The IGF-1 released by the cells would then act to promote chondrogenesis, as described in the prior paragraph. Even though the transfection efficiency may be low, we hypothesize that enough cells will be transfected to produce therapeutic levels of IGF-1 locally.

MATERIALS AND METHODS

Preparation of cationized gelatin

Gelatin (porcine skin; G2625, Sigma-Aldrich, St. Louis, MO) was chemically modified by grafting amino groups to carboxyl groups as previously reported[36–38] using a carbodiimide chemical treatment. Briefly, 2.5 g gelatin was dissolved in 0.1*M* phosphate-buffered solution (pH 5.0), to which was added 7.9 mL ethylenediamine (Sigma-Aldrich) and 1.34 g 1-ethyl-3-(3-dimethylaminopropyl) carbodiimide hydrochloride, EDAC (Sigma-Aldrich). The pH was immediately adjusted to 5.0 with 5–6 *N* hydrochloric acid. The mixture was stirred at room temperature for 16–18 h, dialyzed for 48 h in distilled water, and then freeze-dried to obtain the cationized gelatin.

Preparation of plasmid DNA

The plasmids encoding for IGF-1 (pIGF-1) and enhanced green fluorescent protein (pEGFP) were amplified in *Escherichia coli* host strain DH5α, and purified by column chro-

matography with the QIAfilter plasmid Mega kit (QIAGEN, Valencia, CA) according to the manufacturer's protocol. The plasmid for EGFP was used as a reporter gene to visualize the transfection of chondrocytes by fluorescence microscopy. The antibiotics used to select pIGF-1 and pEGFP transformed cells were ampicilin and kanamycin, respectively. The size of the pEGFP was 4.7 kb and the pIGF-1 was between 6 and 7 kb in size. The yield, purity, and integrity of the prepared plasmids were evaluated with an ultraviolet spectrophotometer and by gel electrophoresis.

Incorporation of plasmid IGF-1 into cationized gelatin nanoparticles

Cationized gelatin-plasmid IGF-1 nanoparticles (CGPIN) were prepared by complex coacervation. The cationized gelatin stock solution (80 mg/mL) was made by dissolving 0.24 g cationized gelatin in 3 mL distilled water. The solution was then filtered for sterilization. Working solutions with different cationized gelatin concentrations were diluted with sterilized water. The pIGF-1 and pEGFP working solutions (200 μg/mL) were prepared with sterile filtered 50 m*M* sodium sulfate (Fisher Scientific, Hampton, NH). Aliquots (100–150 μL) of the cationized gelatin and pIGF-1 or pEGFP solutions were heated separately at 55°C for 30–45 min. Equal volumes of the solutions were quickly mixed and vortexed for 60 s. Nanoparticles, which were prepared with either the pIGF-1 or the pEGFP, were used without further purification. The nanoparticles containing pEGFP were prepared with cationized gelatin using a gelatin:plasmid weight ratio of 250:1, whereas a variety of ratios were investigated when making nanoparticles encapsulating pIGF-1. As a control group, nanoparticles were also synthesized using the original (noncationized) gelatin material.

Environmental scanning electron microscopy

Environmental scanning electron microscopy (ESEM, XL30, FEI/Philips, Hillsboro, OR) was used to investigate the size and shape of the nanoparticles. Samples were prepared by placing 1 μL of the nanoparticle suspension onto glass slides and air drying. The air-dried samples were then observed directly under ESEM, without the need to coat the samples with a conducting layer as required for conventional SEM.

Determination of nanoparticle size distribution

The particle size distribution was determined by a dynamic light scattering technique, performed at 25°C using a Brookhaven 200SM goniometer, a BI-9000AT digital auto-correlator, and Spectra-Physics Argon laser operating at 514 nm (Brookhaven Instruments Corporation, Holtsville, NY). The measured scattering intensities were analyzed by software provided by Brookhaven. The detection limits for dynamic light scattering generally range from 2–3 nm to 2–3 μm.

Zeta potential

The zeta potential of the nanoparticles, with different weight ratios of gelatin to plasmid, was measured with a Brookhaven Zeta Plus apparatus (Brookhaven Instruments Corporation, Holtsville, NY). The electrophoretic mobility was determined at 25°C, and the zeta potential was calculated. This measurement reflected the degree of cationization, and may be of use in future work relating the behavior of the nanoparticles (e.g., ability to be endocytosed by cells) to their charge.

Gene transfer to adult articular chondrocytes in monolayer using gelatin nanoparticles incorporating pEGFP and pIGF-1

Chondrocytes were isolated from the trochleae of both knees (stifle joints) from one adult mongrel dog (approximate age 2–4 years) using a sequential digestion of pronase (20 U/mL, 1 h) and collagenase (200 U/mL, overnight). The cells were expanded in number in monolayer culture with medium containing Dulbecco's modified Eagle's medium (DMEM, high glucose 4.5% without L-glutamine), 0.1 m*M* nonessential amino acids, 10 m*M* *N*-2-Hydroxyethylpiperazine-*N*′-2-ethanesulfonic (HEPES) buffer, 100 U/mL penicillin, 100 μg/mL streptomycin glutamate, 10% FBS (Invitrogen Corporation, Carlsbad, CA), and a mixture of the following growth factors (R&D Systems, Minneapolis, MN): TGF-β1 (1 ng/mL), FGF-2 (5 ng/mL), and PDGF-bb (10 ng/mL). At confluence, cells were trypsinized and either plated onto glass bottom microwell dishes (MatTek Corporation, Ashland, MA) for transfection with nanoparticles incorporating pEGFP or into 24-well tissue culture plates for transfection with nanoparticles incorporating pIGF-1. Passage 0 cells were seeded in both types of dishes at a density of 5×10^4 cells per well (density of 30,000 cells/cm^2) and were allowed to expand overnight to about 80–90% confluence (about 100,000 cells) before transfection.

For transfection with gelatin nanoparticles incorporating either plasmid, the medium was removed and replaced with a 250 μL suspension of nanoparticles diluted in a serum-free medium. The serum-free medium consisted of DMEM (high glucose 4.5% without L-glutamine), 0.1 m*M* nonessential amino acids, 10 m*M* HEPES buffer, 100 U/mL penicillin, 100 μg/mL streptomycin glutamate, ITS^{+1} (100×, by Sigma Chemical, St. Louis, MO), 0.1m*M* ascorbic acid 2-phosphate, 1.25 mg/mL bovine serum albumin, 10 ng/mL of TGF-β1, and 100 n*M* dexamethasone. Five hours later, the nanoparticle solution was removed and replaced with fresh serum-free medium (500 μL/well) that did not contain nanoparticles. On the basis of an average nanoparticle diameter and a gelatin density of about 1 g/mL, we estimated that the number of nanoparticles added to the monolayer chondrocytes was on the order of 10^{12}. Assuming that the cultures to which the nanoparticles were added contained ~100,000 cells, the number of nanoparticles per cell was estimated to be 10^7.

Monolayers that were treated with cationized gelatin nanoparticles incorporating pEGFP at a weight ratio of 250:1 and a plasmid amount of 10 μg per well were examined by transmitted fluorescence microscopy 48 h after

transfection in order to visualize successful gene transfer to cells using these nanoparticles.

IGF-1 expression as a function of plasmid loading in the nanoparticles

For IGF-1-transfected monolayers, the effects of cationized gelatin:IGF-1 ratio and plasmid amount added to each well were investigated. Five different cationized gelatin:IGF-1 ratios were investigated (by weight): 150:1, 200:1, 250:1, 300:1, and 400:1. For these groups, a constant plasmid load of 10 μg per well was used. In experiments in which plasmid amount was the main variable, the five different plasmid amounts used were 2, 5, 8, 10, and 12 μg of plasmid per well, at a constant cationized gelatin to pIGF-1 weight ratio of 250:1. Control conditions consisted of pIGF-1 only (10 μg) or no treatment (just added serum-free medium). Nanoparticles synthesized using unmodified (original) gelatin at a gelatin:IGF-1 ratio of 250:1 were also included as an experimental condition to determine the effect of cationization on nanoparticle characteristics and transfectibility. The serum-free medium from IGF-1-transfected cultures was collected at 144 h after transfection and assessed for the presence of IGF-1 protein ($n = 4$) with a human IGF-1 sandwich ELISA kit (R&D Systems, Minneapolis, MN).

Behavior of monolayer-transfected chondrocytes seeded within collagen-GAG scaffolds

An *in vitro* experiment was performed to determine if the chondrocytes transfected by the nanoparticles containing the IGF-1 plasmid would demonstrate elevated production of a cartilage-specific matrix molecule (GAG) when grown in a collagen-GAG scaffold, which: (1) might serve as an analog of extracellular matrix for *in vitro* evaluation of cell behavior in a three-dimensional (3D) culture system; and (2) could be used as a tissue engineering scaffold for the future delivery of the nanoparticle-transfected cells or the nanoparticles themselves *in vivo*.

The scaffolds were fabricated by freeze-drying a porcine-derived type II collagen-GAG slurry (Geistlich Biomaterials, Wolhusen, Switzerland) to form sheets ~2 mm in thickness. Morphometric analysis of the pore structure performed as previously reported[50] indicated a pore diameter of 190 ± 25 μm and porosity of 88% ± 1%. The porous sheets were sterilized and cross-linked by dehydrothermal treatment[51,52] under a vacuum (50 mTorr) and temperature of 105°C for 24 h. Nine-millimeter diameter disks (~2 mm thick) were punched out using a dermal punch (Moore Medical, New Britain, CA) and additionally cross-linked by a 10 min carbodiimide treatment containing an aqueous solution of 14 m*M* 1-ethyl-3-(3-dimethylaminopropyl) carbodiimide hydrochloride and 5.5 m*M* *N*-hydroxysuccinimide (EDAC; Sigma Chemical Co., St. Louis, MO). Excess EDAC was removed by rinsing in PBS.

Using CGPIN synthesized with a gelatin:plasmid weight ratio of 250:1, chondrocyte monolayers were transfected and the cells subsequently seeded in CG scaffolds ~24 h after transfection to assess the duration of IGF-1 overexpression in 3D culture and the effects on biosynthesis. Four million transfected cells were seeded onto each scaffold by pipetting a 20 μL suspension containing half of the total amount of cells on each side of the scaffold with a 10 min incubation period in between. By this static seeding method ~80% of the seeded chondrocytes have been found to attach to the scaffolds. Cell-seeded scaffolds were cultured in the serum-free medium described above. Medium was collected and changed every 2–3 days over a 14-day culture period. The amount of IGF-1 in the medium ($n = 6$) was detected by a sandwich ELISA kit for the human IGF-1 protein (R&D Systems). Cultures were terminated after 2 weeks and scaffolds were lyophilized and enzymatically digested using proteinase K (Roche Diagnostics, Indianapolis, IN) for DNA and GAG biochemical analyses.

DNA analysis

The DNA content of cell-seeded scaffolds was measured using the Picogreen Dye assay kit (Molecular Probes, Eugene, OR) ($n = 4$–6). The Picogreen dye was used with the reagents and standard provided according to the manufacturer instructions.

GAG analysis

The sulfated GAG content of cell-seeded scaffolds was determined by the dimethylmethylene blue (DMMB) dye assay[46] ($n = 4$–6). An aliquot of the proteinase K digest was mixed with the DMMB dye and the absorbance at 525 nm was measured with a spectrophotometer. The results were obtained by extrapolating from a standard curve using shark chondroitin-6-sulfate. Newly accumulated GAG was determined by subtracting the unseeded values from the sample values.

Statistical analyses

Data were analyzed by one or two-factor analysis of variance (ANOVA), and the Fisher's protected least squares differences (PLSD) post-hoc test to determine the significance in the difference between selected groups using StatView (SAS Institute, Cary, NC). Data are presented as mean ± standard error of the mean (SEM).

RESULTS

Morphology of the cationized gelatin-pIGF-1 nanoparticles

ESEM (Fig. 1) revealed different sizes and morphologies of the pIGF-1-containing nanoparticles prepared with cationized gelatin versus regular gelatin (using the same gelatin:plasmid weight ratio of 250:1). The cationized gelatin nanoparticles [Fig 1(a,b)] generally appeared to be of spherical shape. The small size of the cationized gelatin nanoparticles precluded definitive measurement of their diameter

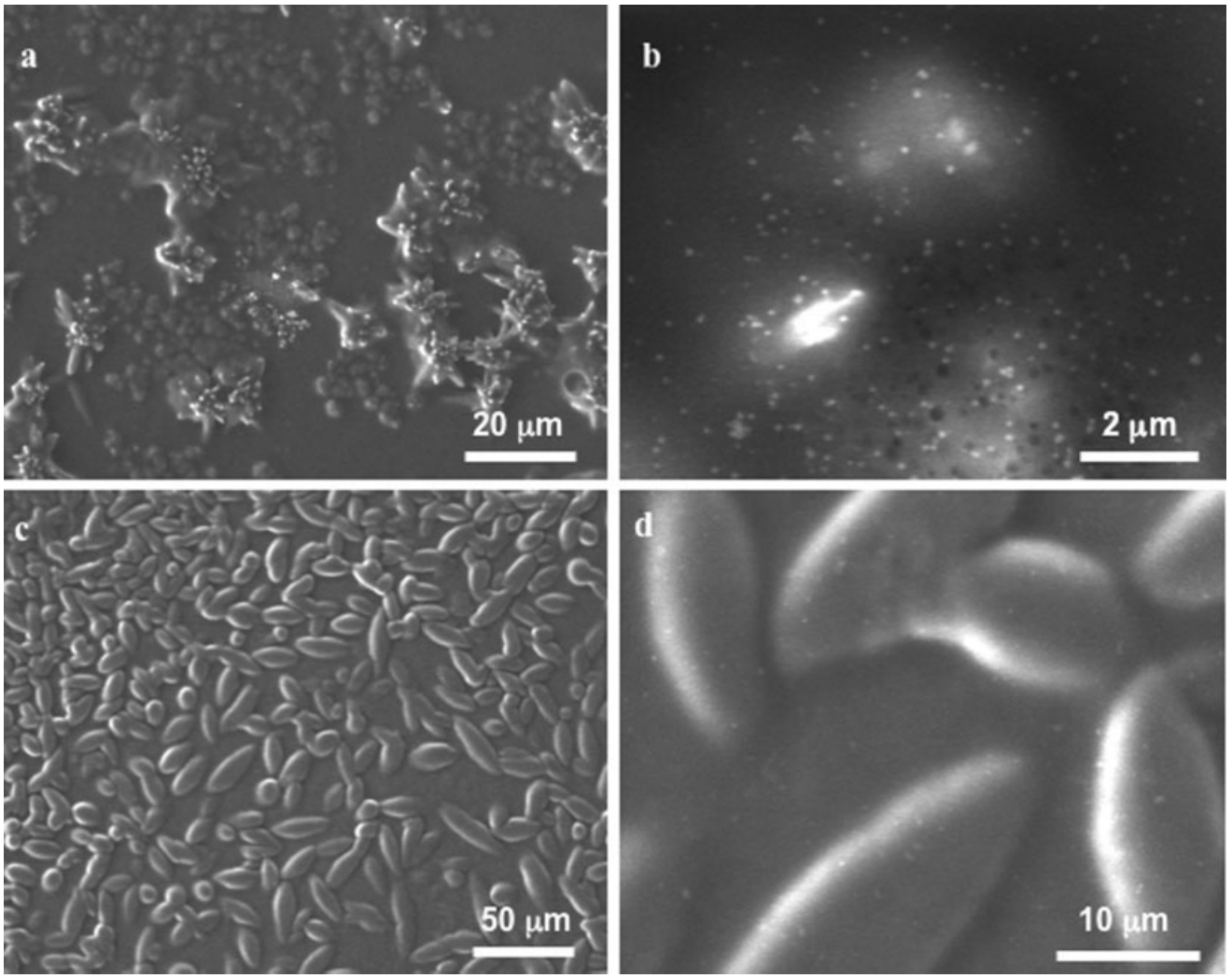

Figure 1. Environmental scanning electron microcopy images of cationized gelatin-pIGF-1 nanoparticles (a, b) and noncationized (original) gelatin-pIGF-1 microparticles (c, d), using a gelatin-plasmid weight ratio of 250:1.

by ESEM. The particles generally appeared, however, to be less than 200 nm, which was consistent with the measurements made by dynamic light scattering (reported in the next section). In contrast, the original gelatin formed micro-scale particles with spherical and ellipsoid shapes [Fig 1(c,d)], with the average diameter (and long axis) appearing to be from 10 μm to greater than 20 μm. For both the cationized and noncationized gelatin:plasmid preparations, the nanoparticles and microparticles, respectively, generally appeared to be of uniform size.

Particle size distribution

Dynamic light scattering revealed that the size of the cationized gelatin nanoparticles ranged from 7 to 387 nm, with an average diameter of 172 nm. The original gelatin particles displayed a wider size range

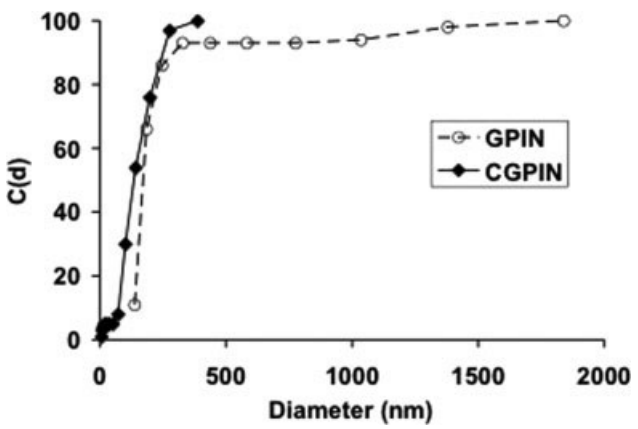

Figure 2. Particle size distribution of cationized gelatin-pIGF-1 nanoparticles (CGPIN) and original gelatin-pIGF-1 particles (GPIN). Cumulative percentage of nanoparticles, C (d), plotted against particle size. Nanoparticles were made with cationized gelatin and original gelatin at a weight ratio of 250:1.

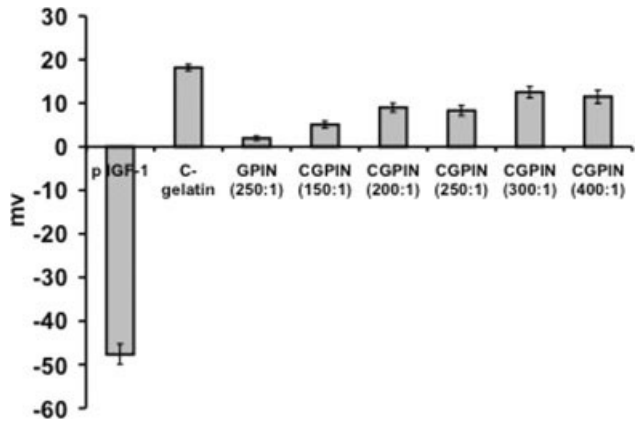

Figure 3. Zeta potential of naked IGF-1 plasmid (1st bar), cationized gelatin (2nd bar), original gelatin complexed to pIGF-1 at a 250:1 weight ratio (3rd bar), and cationized gelatin complexed with different amounts of pIGF-1 to yield the following gelatin:plasmid weight ratios: 150:1, 200:1, 250:1, 300:1, and 400:1.

extending to greater than 1.8 μm, larger than could be evaluated by dynamic light scattering (Fig. 2).

Surface charge of gelatin nanoparticles

The zeta potential (Fig. 3) of the naked plasmid IGF-1 solution was −48 ± 2 mV (mean ± standard error for 5 runs of the same sample). When the plasmid was coupled with different amounts of the positively charged cationized gelatin (+18 ± 0.7 mV for cationized gelatin alone), the zeta potential went from a negative value to a positive value and increased by ~50–58 mV. Interestingly, with the increasing cationized gelatin:plasmid weight ratio, the surface charge of the nanoparticles did not show a significant change. Cationized gelatin pIGF-1 nanoparticles displayed a fourfold higher positive charge compared to particles made with the unmodified gelatin (GPIN) using a 250:1 gelatin to plasmid weight ratio.

Fluorescence microscopy of the chondrocytes transfected with the nanoparticles containing pEGFP

There was no noticeable fluorescence from the cells treated with the nanoparticles prepared with the original (noncationized) gelatin particles containing the pEGFP [Fig. 4(a)]. In contrast numerous cells in the group transfected with the cationized gelatin-pEGFP nanoparticles were found to fluoresce indicating successful transfection and gene expression [Fig. 4(b)].

IGF-1 gene expression in transfected chondrocyte monolayers

No detectable IGF-1 was found in control monolayer cultures of these adult canine chondrocytes. The coefficients of variation for the IGF-1 levels recorded from all but two of the nine experimental groups, varying gelatin to plasmid weight ratios and plasmid loading ($n = 4$), were from 10–30%. In two of the groups (10 μg loading with a gelatin:plasmid ratio of 400:1 and 10 μg loading with 250:1) the coefficients were around 60% owing to an outlier in each that was about twice the mean value for the group. It was decided to omit the elevated data point in each of the two groups, reducing the sample size from 4 to 3, but taking a more conservative approach

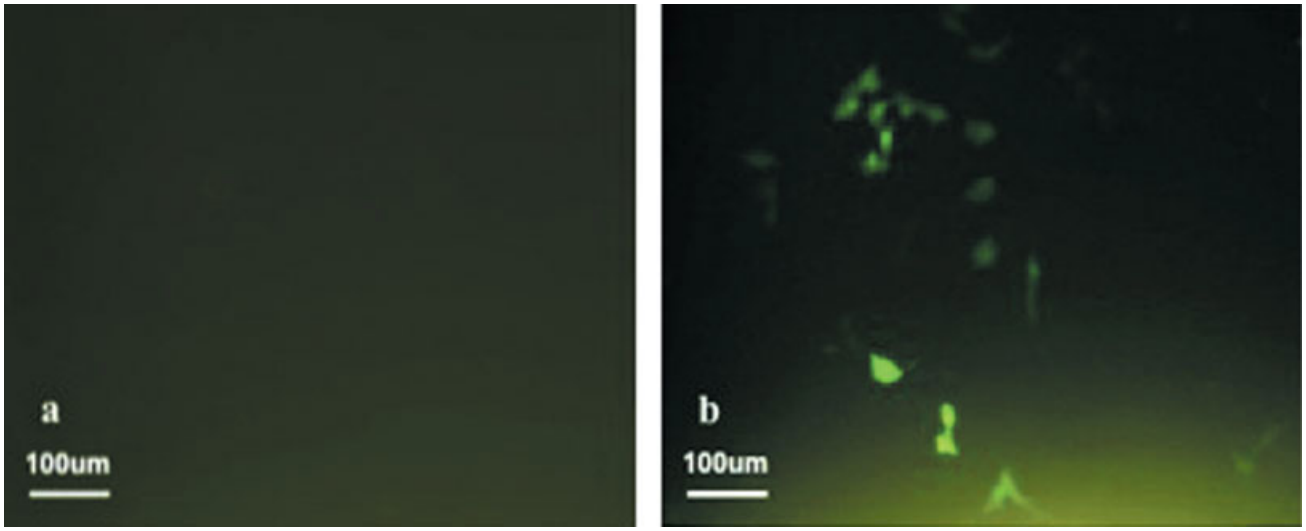

Figure 4. Fluorescence microscopy of chondrocytes transfected with nanoparticles incorporating pEGFP 48 h after transfection using original gelatin (a) or cationized gelatin (b). [Color figure can be viewed in the online issue, which is available at www.interscience.wiley.com.]

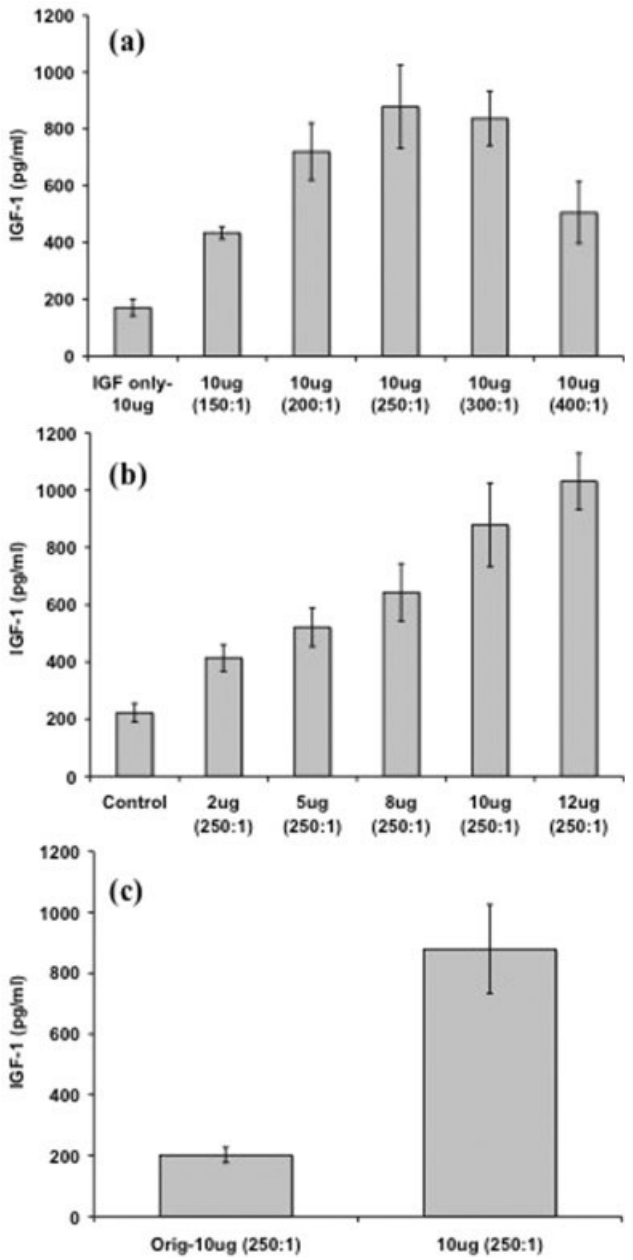

Figure 5. IGF-1 protein released into the medium from monolayer chondrocytes 144 h after treatment with gelatin-plasmid IGF-1 nanoparticles: varying the cationized gelatin to pIGF-1 weight ratio using a 10 mg plasmid load (a); varying plasmid load using a 250:1 weight ratio (b); and comparing transfection using original gelatin particles vs. cationized gelatin nanoparticles (c). $n = 3$–4; mean ± SEM.

to the analysis of the data (i.e. omitting the outliers decreased the detected levels of protein).

There was a clear effect of varying the weight ratio of gelatin to pIGF-1 on gene transfer and subsequent IGF-1 release in the medium [Fig. 5(a)]. Optimal IGF-1 expression was recorded for gelatin to plasmid weight ratios of 200–300:1. There was a fivefold elevation in the amount of IGF-1 produced from the group treated with nanoparticles synthesized at a weight ratio of 250:1 compared with the control group that was treated with pIGF-1 alone [Fig. 5(a)]. One-factor ANOVA revealed a significant effect of the weight ratio of cationized gelatin to pIGF-1 on the amount of IGF-1 synthesized by the cells ($p < 0.0002$; power = 1). Fisher's PLSD post-hoc testing demonstrated that all plasmid ratios had statistically significant elevations of IGF-1 production over the control condition treated with plasmid only (i.e. no incorporation in nanoparticles, $p < 0.04$). Among the gelatin:plasmid weight ratios, there was no statistically significant difference among the 200:1, 250:1, and 300:1 groups, but there was a significant difference comparing these groups with the 150:1 group ($p < 0.03$), and comparing the 250:1 and 300:1 groups versus the 400:1 group ($p < 0.02$).

There was also a notable effect of varying the amount of plasmid added to each well on IGF-1 produced by the transfected chondrocytes [Fig. 5(b)]. There was a gradual increase in IGF-1 expression with increasing plasmid load. Linear regression analysis demonstrated a correlation between IGF-1 expression and plasmid load ($R^2 = 0.65$). One-factor ANOVA showed a significant effect of plasmid amount added per well on IGF-1 expression ($p < 0.0001$; power = 1). Post-hoc testing revealed that there was a statistically significant elevation in IGF-1 produced for all plasmid loads except the 2 μg load when compared to the control group. The 12 μg load showed a statistically significant elevation of IGF-1 expression above the plasmid load groups of 8 μg or less ($p < 0.02$). The 10 μg load showed a significant elevation above plasmid loads of 5 μg or less ($p < 0.01$). There was, however, no significant difference between the 5 and 8 μg plasmid load groups or the 10 and 12 μg groups.

The difference between using unmodified (noncationized) gelatin and cationized gelatin nanoparticles for the transfection of the chondrocytes was clearly demonstrated [Fig. 5(c)]. There was a fivefold elevation in the amount of IGF-1 produced by transfected cells when using the cationized gelatin nanoparticles [Fig. 5(c)]. ANOVA showed a statistically significant difference in the IGF-1 expression between the groups ($p < 0.003$; power = 0.99).

IGF-1 gene expression of transfected chondrocytes seeded in CG scaffolds and effects on biosynthesis

Cultures of scaffolds seeded with chondrocytes that were transfected in monolayer using gelatin/pIGF-1 nanoparticles (CGPIN group) showed a clear elevation of IGF-1 release above the Control (no treatment, medium only) and Gelatin (gelatin alone, no plasmid) groups for all media collections (Fig. 6).

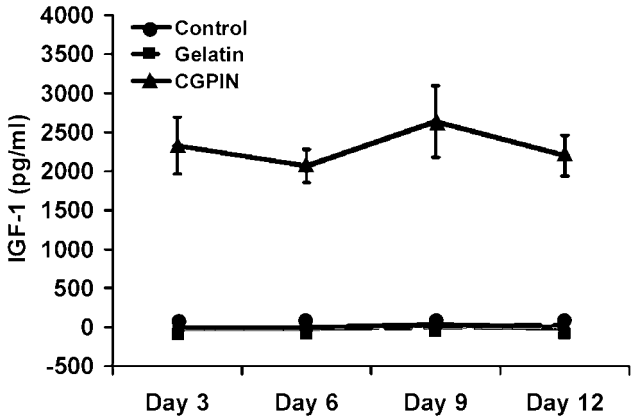

Figure 6. IGF-1 released in medium from control cell-seeded scaffolds and chondrocytes transfected in monolayer with CGPIN (gelatin:plasmid IGF-1 of 250:1) and subsequently seeded in CG scaffolds. $n = 6$; mean ± SEM. The results for the Control (no treatment, i.e., medium only) and Gelatin (gelatin alone, no plasmid) groups are superimposed on one another, and the error bars are contained within the space of the symbol.

The CGPIN group showed a steady IGF-1 release of about 2200 pg/mL every 3 days over the course of the 12-day period. There was no noticeable amount of IGF-1 released in the media for the Control or Gelatin groups. Two-factor ANOVA verified a significant effect of transfection with gelatin/pIGF-1 nanoparticles on IGF-1 release from cell-seeded scaffolds ($p < 0.0001$, power = 1) but no significant effect of time over the 12-day culture period.

There was a slight, significant elevation in DNA content (Fig. 7) at the end of the culture period for the Control group compared to the other groups ($p < 0.03$, power = 0.7). GAG and DNA analyses showed the highest level of accumulated GAG per DNA for the CGPIN group, with a 60% higher level than the Control group and a 40% higher GAG/DNA level than the Gelatin group. Constructs seeded with cells treated in monolayer with gelatin alone (Gelatin group) also showed a 38% higher GAG/DNA content than the Control group. ANOVA showed a significant effect of monolayer treatment on the resulting accumulated GAG/DNA content at the end of the 3D culture period ($p < 0.001$, power = 1).

DISCUSSION

The results of the present study demonstrated the benefits of altering the charge of gelatin through cationization, with respect to its use as a delivery vehicle for plasmid IGF-1 for nonviral gene transfer to chondrocytes. When complexed with the plasmid, unmodified gelatin tended to form particles of substantially larger size and broader size range. Increasing the positive charge of gelatin may have enabled it to condense the pIGF-1 such that smaller (nanometer-sized) particles could be produced, but this point needs to be further investigated before a definitive conclusion can be drawn.

The degree of cationization was reflected in the zeta potential measurements. The isoelectric point derived from zeta potential measurements of gelatin nanoparticles alone has previously been reported as 5.7.[19] In the present study, cationized gelatin alone was found to have a potential of +18 ± 0.7 mV, and cationized gelatin pIGF-1 nanoparticles displayed a potential of about +8 mV compared with +2 mV for the unmodified gelatin/IGF-1 plasmid complex for the same ratio (250:1 gelatin to plasmid weight ratio). In future work, it will be instructive to determine the degree of cationization based on the percentage of amino groups introduced into gelatin as determined by the conventional trinitrobenzene sulfonate method.[18]

Of interest were the findings demonstrating the difference in the functionality of the cationized and

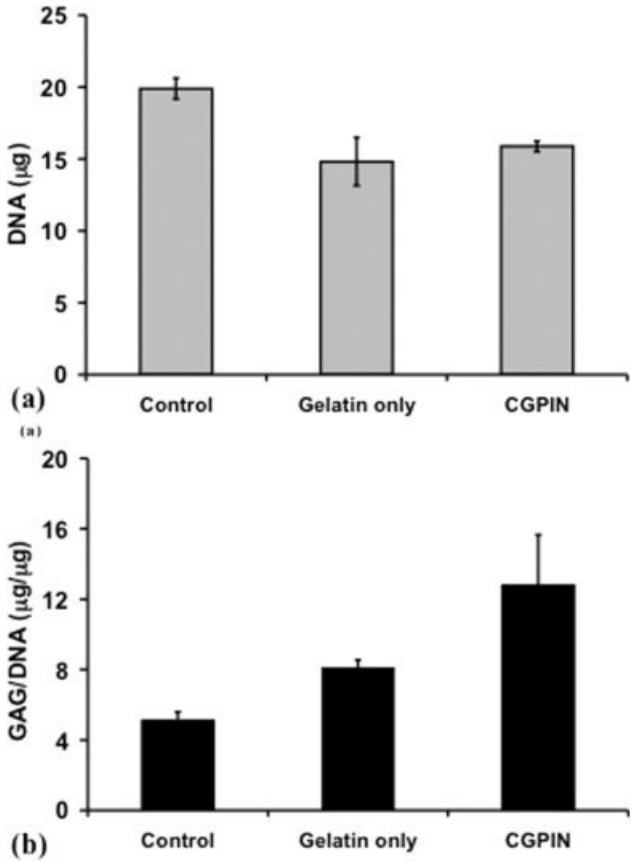

Figure 7. DNA contents (a) and accumulated GAG/DNA (b) measured at the end of the 3D culture period in CG scaffolds seeded with untreated chondrocyte monolayers (Control), chondrocytes treated with gelatin alone (Gelatin only), or chondrocytes transfected in monolayer with CGPIN at a gelatin:plasmid IGF-1 of 250:1 (CGPIN). $n = 4$; mean ± SEM.

noncationized gelatin particles as transfection agents for the plasmids encoding EGFP and IGF-1. Virtually no fluorescence was detected in chondrocytes treated with the marker gene, EGFP, incorporated in the unmodified gelatin particles, while many cells were transfected with the pEGFP using the cationized gelatin nanoparticles. This difference was also demonstrated by the five-fold difference in expression of IGF-1 between groups treated with the cationized gelatin-pIGF-1 versus the noncationized-pIGF-1 particles indicating that there are important functional differences imparted by charge modification, perhaps owing to a difference in particle size or surface charge. A higher positive surface charge may increase interactions with the negatively charged cellular membrane and a smaller particle diameter may increase probable entry into to cell, resulting in enhanced gene expression. Additional studies will be required to provide a deeper understanding of the transfection mechanisms that are responsible for the differences in the behavior of the cationized and noncationized particles.

The present findings also revealed an optimal cationized gelatin:pIGF-1 weight ratio range for transfecting adult articular chondrocytes, with maximum IGF-1 expression recorded for weight ratios of 200–300:1. The surface charge of the nanoparticles made with the varying weight ratios, however, may not have been a significant factor influencing gene transfer to chondrocytes as the surface charge did not seem to change significantly using different weight ratios. It will be useful in future work to evaluate other potential mechanisms related to the ability of these nanoparticles to transfect cells, such as particle size and morphology and the kinetics of plasmid release from nanoparticles prepared with other gelatin:plasmid weight ratios.

The current investigation demonstrated a nearly linear increase in IGF-1 production by cells with increasing plasmid load applied to the cultures when using cationized gelatin nanoparticles. Based on an estimated cell number in each well of about 100,000 cells and using a cationized gelatin:IGF-1 weight ratio of 250:1, one would need about 50 pg of incorporated plasmid within cationized gelatin nanoparticles per cell for meaningful gene expression. The $\sim$1 ng of IGF-1 collected in the first 144 h after transfection (using a 250:1 cationized gelatin:pIGF-1 and a 10 μg plasmid load) is well below the minimum therapeutic levels generally found *in vitro* to elicit a response from chondrocytes using the recombinant IGF-1 as a medium supplement. However, this 1 ng level was achieved after only 5 h of incubation of the cells with the nanoparticles. Moreover, in a contained defect *in vivo*, small levels of overexpressed IGF-1 concentrated locally may still be able to achieve therapeutic results.

The effect of localized and elevated levels of IGF-1 expression on biosynthesis was demonstrated by comparing CG scaffolds seeded with untreated chondrocytes and chondrocytes transfected in monolayer with CGPIN. These results showed that IGF-1 overexpression above the control groups can be maintained when transfected chondrocytes are seeded within CG scaffolds for up to about 2 weeks in 3D culture. The CGPIN group showed very steady IGF-1 release levels with no evidence of decreasing IGF-1 overexpression at the end of the 12-day culture period. The elevated levels of IGF-1 for the CGPIN group resulted in a 60% greater GAG/DNA content than the Control group after 12 days in 3D culture. The finding that cationized gelatin nanoparticles containing IGF-1 plasmid can stimulate GAG production in this *in vitro* assay is consistent with prior findings as reviewed in the *Introduction* section, and lays the groundwork for future *in vivo* studies to determine if this approach can play a meaning role in cartilage repair procedures by implanting the scaffolds, which contain the nanoparticles alone or the IGF-1/nanoparticle-transfected cells.

Surprisingly, CG constructs containing chondrocytes treated with gelatin alone (without plasmid) in monolayer also resulted in a significantly higher GAG/DNA content (38% higher) verses the Control group even though there was no elevation in IGF-1 expression for this group compared with the Control. This finding seems to indicate that gelatin alone can affect chondrocytes in monolayer and may induce elevations in biosynthesis when these cells are subsequently grown in CG scaffolds.

Few studies have yet investigated the mechanisms by which gelatin nanoparticles gain entry into cells. One recent transmission electron microscopy study[25] provided evidence of the endocytosis of gelatin nanoparticles by fibroblasts. While the nanoparticles in the cytoplasm of the cells appeared to disrupt the F-actin and β-tubulin cytoskeleton, there was no evidence of toxicity. Additional work is necessary to more completely understand the mechanisms by which gelatin nanoparticles are endocytosed, and the contained plasmid released and incorporated into the cell nucleus.

CONCLUSIONS

The results of the present work demonstrate that gelatin nanoparticles can be synthesized to incorporate plasmid containing the IGF-1 gene, and can successfully transfect expanded chondrocytes in monolayer culture. Chemical modification of gelatin by cationization, varying the cationized gelatin to plasmid weight ratio, and varying the amount of plasmid added to the cells all significantly affect result-

ing gene expression and growth factor release kinetics. Furthermore, chondrocytes transfected with pIGF using cationized gelatin nanoparticles are able to maintain steady IGF-1 overexpression when subsequently grown in CG scaffolds for up to 2 weeks in 3D culture, and show enhanced biosynthesis. These findings warrant additional study of the implementation of cationized gelatin nanoparticles incorporating growth factor plasmids in conjunction with scaffolds to facilitate tissue engineering.

The authors appreciate the assistance of Erika Marsillio, Ph.D for advice regarding the growth of the plasmids and JianYi Cui and Hao Wang, Ph.D. of the Department of Materials Science and Engineering at the Massachussetts Institute of Technology for assistance with light scattering and zeta potential measurements. Ximing Xu received support as a Visiting Associate Professor at Harvard Medical School from the Jiangsu Municipal Government and Jiangsu University, Zhenjiang, China. The authors are grateful to C.E. Evans and the Center for Orthopedic Molecular Biology and Gene Therapy at the Brigham and Women's Hospital and Harvard Medical School for providing the IGF-1 plasmid. This work was funded in part by Rehabilitation Research and Development of the Department of Veterans Affairs, a VA Research Career Scientist Award (MS), and the Department of Defense.

References

1. Vasita R, Katti DS. Growth factor-delivery systems for tissue engineering: A materials perspective. Expert Rev Med Devices 2006;3:29–47.
2. Tabata Y. Tissue regeneration based on growth factor release. Tissue Eng 2003;9 (Suppl 1):S5–S15.
3. Whitaker MJ, Quirk RA, Howdle SM, Shakesheff KM. Growth factor release from tissue engineering scaffolds. J Pharm Pharmacol 2001;53:1427–37.
4. Babensee JE, McIntire LV, Mikos AG. Growth factor delivery for tissue engineering. Pharm Res 2000;17:497–504.
5. Partridge KA, Oreffo RO. Gene delivery in bone tissue engineering: Progress and prospects using viral and nonviral strategies. Tissue Eng 2004;10:295–307.
6. Jang JH, Houchin TL, Shea LD. Gene delivery from polymer scaffolds for tissue engineering. Expert Rev Med Devices 2004;1:127–138.
7. Capito RM, Spector M. Scaffold-based articular cartilage repair. IEEE Eng Med Biol Mag 2003;22:42–50.
8. Samuel RE, Lee CR, Ghivizzani S, Evans CH, Yannas IV, Olsen BR, Spector M. Delivery of plasmid DNA to articular chondrocytes via novel collagen-glycosaminoglycan matrices. Hum Gene Ther 2002;13:791–802.
9. Bonadio J, Smiley E, Patil P, Goldstein S. Localized, direct plasmid gene delivery in vivo: Prolonged therapy results in reproducible tissue regeneration. Nat Med 1999;5:753–759.
10. Lee CR, Grodzinsky AJ, Hsu HP, Spector M. Effects of a cultured autologous chondrocyte-seeded type II collagen scaffold on the healing of a chondral defect in a canine model. J Orthop Res 2003;21:272–281.
11. Breinan HA, Martin SD, Hsu H-P, Spector M. Healing of canine articular cartilage defects treated with microfracture, a type II collagen matrix, or cultured autologous chondrocytes. J Orthop Res 2000;18:781–789.
12. Kreuter J. Nanoparticles and nanocapsules—New dosage forms in the nanometer size range. Pharm Acta Helv 1978; 53:33–39.
13. Marty JJ, Oppenheim RC, Speiser P. Nanoparticles—A new colloidal drug delivery system. Pharm Acta Helv 1978;53:17–23.
14. Vandervoort J, Ludwig A. Preparation and evaluation of drug-loaded gelatin nanoparticles for topical ophthalmic use. Eur J Pharm Biopharm 2004;57:251–261.
15. Leo E, Arletti R, Forni F, Cameroni R. General and cardiac toxicity of doxorubicin-loaded gelatin nanoparticles. Farmaco 1997;52:385–388.
16. Li JK, Wang N, Wu XS. Gelatin nanoencapsulation of protein/peptide drugs using an emulsifier-free emulsion method. J Microencapsul 1998;15:163–172.
17. Truong-Le VL, August JT, Leong KW. Controlled gene delivery by DNA-gelatin nanospheres. Hum Gene Ther 1998;9: 1709–1717.
18. Kushibiki T, Tomoshige R, Fukunaka Y, Kakemi M, Tabata Y. In vivo release and gene expression of plasmid DNA by hydrogels of gelatin with different cationization extents. J Control Release 2003;90:207–216.
19. Zwiorek K, Kloeckner J, Wagner E, Coester C. Gelatin nanoparticles as a new and simple gene delivery system. J Pharm Pharm Sci 2005;7:22–28.
20. Dang JM, Leong KW. Natural polymers for gene delivery and tissue engineering. Adv Drug Deliv Rev 2006;58:487–499.
21. Inada S, Fujiwara H, Atsuji K, Takashima K, Araki Y, Kubota T, Tabata Y, Yamagishi H. Successful gene transfer into dendritic cells with cationized gelatin and plasmid DNA complexes via a phagocytosis-dependent mechanism. Anticancer Res 2006;26(3A):1957–1963.
22. El-Shabouri MH. Positively charged nanoparticles for improving the oral bioavailability of cyclosporin-A. Int J Pharm 2002:249:101–108.
23. Farrugia CA, Groves MJ. Gelatin behaviour in dilute aqueous solution: Designing a nanoparticulate formulation. J Pharm Pharmacol 1999;51:643–649.
24. Coester CJ, Langer K, van Briesen H, Kreuter J. Gelatin nanoparticles by two step desolvation—A new preparation method, surface modifications and cell uptake. J Microencapsul 2000;17:187–193.
25. Gupta AK, Gupta M, Yarwood SJ, Curtis AS. Effect of cellular uptake of gelatin nanoparticles on adhesion, morphology and cytoskeleton organisation of human fibroblasts. J Control Release 2004;95:197–207.
26. Cascone MG, Lazzeri L, Carmignani C, Zhu Z. Gelatin nanoparticles produced by a simple W/O emulsion as delivery system for methotrexate. J Mater Sci: Mater Med 2002;13:523–526.
27. Kommareddy S, Amiji M. Preparation and evaluation of thiol-modified gelatin nanoparticles for intracellular DNA delivery in response to glutathione. Bioconjug Chem 2005;16: 1423–1432.
28. Kushibiki T, Tabata Y. Preparation of poly(ethylene glycol)-introduced cationized gelatin as a non-viral gene carrier. J Biomater Sci Polym Ed 2005;16:1447–1461.
29. Kaul G, Amiji M. Tumor-targeted gene delivery using poly (ethylene glycol)-modified gelatin nanoparticles: In vitro and in vivo studies. Pharm Res 2005;22:951–961.
30. Kaul G, Amiji M. Cellular interactions and in vitro DNA transfection studies with poly(ethylene glycol)-modified gelatin nanoparticles. J Pharm Sci 2005;94:184–198.
31. Wartlick H, Michaelis K, Balthasar S, Strebhardt K, Kreuter J, Langer K. Highly specific HER2-mediated cellular uptake of antibody-modified nanoparticles in tumour cells. J Drug Target 2004;12:461–471.

32. Langer K, Coester C, Weber C, von Briesen H, Kreuter J. Preparation of avidin-labeled protein nanoparticles as carriers for biotinylated peptide nucleic acid. Eur J Pharm Biopharm 2000;49:303–307.
33. Coester C, Kreuter J, von Briesen H, Langer K. Preparation of avidin-labelled gelatin nanoparticles as carriers for biotinylated peptide nucleic acid (PNA). Int J Pharm 2000;196:147–149.
34. Balthasar S, Michaelis K, Dinauer N, von Briesen H, Kreuter J, Langer K. Preparation and characterisation of antibody modified gelatin nanoparticles as drug carrier system for uptake in lymphocytes. Biomaterials 2005;26:2723–2732.
35. Zillies J, Coester C. Evaluating gelatin based nanoparticles as a carrier system for double stranded oligonucleotides. J Pharm Pharm Sci 2005;7:17–21.
36. Aoyama T, Hosseinkhani H, Yamamoto S, Ogawa O, Tabata Y. Enhanced expression of plasmid DNA-cationized gelatin complex by ultrasound in murine muscle. J Control Release 2002;80:345–356.
37. Fukunaka Y, Iwanaga K, Morimoto K, Kakemi M, Tabata Y. Controlled release of plasmid DNA from cationized gelatin hydrogels based on hydrogel degradation. J Control Release 2002;80:333–343.
38. Hosseinkhani H, Aoyama T, Ogawa O, Tabata Y. Ultrasound enhancement of in vitro transfection of plasmid DNA by a cationized gelatin. J Drug Target 2002;10:193–204.
39. Kushibiki T, Nagata-Nakajima N, Sugai M, Shimizu A, Tabata Y. Enhanced anti-fibrotic activity of plasmid DNA expressing small interference RNA for TGF- β type II receptor for a mouse model of obstructive nephropathy by cationized gelatin prepared from different amine compounds. J Control Release 2006;110:610–617.
40. Chiyokura Y. Effects of IGF-1, IGF-II, and PDGF on the proliferation of rabbit articular chondrocytes in culture. J Orthop Sci 1996;1:59–63.
41. Sah RL, Chen AC, Grodzinsky AJ, Trippel SB. Differential effects of bFGF and IGF-1 on matrix metabolism in calf and adult bovine cartilage explants. Arch Biochem Biophys 1994;308:137–147.
42. Fortier LA, Lust G, Mohammed HO, Nixon AJ. Coordinate upregulation of cartilage matrix synthesis in fibrin cultures supplemented with exogenous insulin-like growth factor-I. J Orthop Res 1999;17:467–474.
43. Worster AA, Brower-Toland BD, Fortier LA, Bent SJ, Williams J, Nixon AJ. Chondrocytic differentiation of mesenchymal stem cells sequentially exposed to transforming growth factor- β1 in monolayer and insulin-like growth factor-I in a three-dimensional matrix. J Orthop Res 2001;19:738–749.
44. Makower AM, Wroblewski J, Pawlowski A. Effects of IGF-I, rGH, FGF, EGF and NCS on DNA-synthesis, cell proliferation and morphology of chondrocytes isolated from rat rib growth cartilage. Cell Biol Int Rep 1989;13:259–270.
45. Verschure PJ, Van Noorden CJ, Van Marle J, Van den Berg WB. Articular cartilage destruction in experimental inflammatory arthritis: Insulin-like growth factor-1 regulation of proteoglycan metabolism in chondrocytes. Histochem J 1996;28: 835–857.
46. Loeser RF, Pacione CA, Chubinskaya S. The combination of insulin-like growth factor 1 and osteogenic protein 1 promotes increased survival of and matrix synthesis by normal and osteoarthritic human articular chondrocytes. Arthritis Rheum 2003;48:2188–2196.
47. Nixon AJ, Fortier LA, Williams J, Mohammed H. Enhanced repair of extensive articular defects by insulin-like growth factor-I-laden fibrin composites. J Orthop Res 1999;17:475–487.
48. Madry H, Padera R, Seidel J, Langer R, Freed LE, Trippel SB, Vunjak-Novakovic G. Gene transfer of a human insulin-like growth factor I cDNA enhances tissue engineering of cartilage. Hum Gene Ther 2002;13:1621–1630.
49. Madry H, Kaul G, Cucchiarini M, Stein U, Zurakowski D, Remberger K, Menger MD, Kohn D, Trippel SB. Enhanced repair of articular cartilage defects in vivo by transplanted chondrocytes overexpressing insulin-like growth factor I (IGF-I). Gene Ther 2005;12:1171–1179.
50. O'Brien FJ, Harley BA, Yannas IV, Gibson L. Influence of freezing rate on pore structure in freeze-dried collagen-GAG scaffolds. Biomaterials 2004;25:1077–1086.
51. Weadock K, Miller E, Bellincampi L, Zawadsky J. Physical crosslinking of collagen fibers: Comparison of ultraviolet irradiation and dehydrothermal treatment. J Biomed Mat Res 1995;29:1373–1379.
52. Yannas IV, Lee E, Orgill DP, Skrabut EM, Murphy GF. Synthesis and characterization of a model extracellular matrix that induces partial regeneration of adult mammalian skin. Proc Natl Acad Sci USA 1989;86:933–937.

Plasmid size influences chitosan nanoparticle mediated gene transfer to chondrocytes

Ximing Xu,[1,2,3] Ramille M. Capito,[1,4] Myron Spector[1,3,4]
[1]*Tissue Engineering, VA Boston Healthcare System, Boston, Massachusetts 02130*
[2]*Department of Pharmaceutics, School of Pharmacy, Jiangsu University, Zhenjiang, Jiangsu 212001, People's Republic of China*
[3]*Department of Orthopaedic Surgery, Brigham and Women's Hospital, Harvard Medical School, Boston, Massachusetts 02115*
[4]*Department of Materials Science and Engineering, Massachusetts Institute of Technology, Cambridge, Massachusetts 02139*

Received 21 April 2006; revised 1 April 2007; accepted 27 April 2007
Published online 8 August 2007 in Wiley InterScience (www.interscience.wiley.com). DOI: 10.1002/jbm.a.31479

Abstract: The objective of the present study was to prepare chitosan nanoparticles incorporating a relatively large plasmid encoding for osteogenic protein (OP)-1 and to determine the ability of these nanoparticles to transfect adult canine articular chondrocytes *in vitro*. The positive charge of chitosan acted to condense the relatively large negatively-charged OP-1 plasmid such that it could be incorporated into nanoparticles. Incorporation of the plasmid into the chitosan nanoparticles did not affect the structural integrity of the plasmid as demonstrated by gel electrophoresis. The morphology and size of the nanoparticles were found to vary with the chitosan:plasmid weight ratio. Nanoparticles formulated with a chitosan:plasmid ratio of 10:1 were of uniformly small size (less than 250 nm) and spherical shape. These nanoparticles had a positive charge of about 20 mV. FITC-labeled chitosan nanoparticles were found in virtually all of the cells after 24 h of incubation with the nanoparticles, and confocal microscopy revealed FITC-related fluorescence in the nucleus of the chondrocytes. Although transfection of the chondrocytes was demonstrated by the fluorescence of cells treated with chitosan nanoparticles containing the plasmid for the enhanced green fluorescence protein, cells transfected with nanoparticles incorporating the larger OP-1 plasmid did not show OP-1 expression measured by ELISA for up to 2 weeks in culture. These results indicate that although a large plasmid can be successfully incorporated within chitosan nanoparticles, the size of the plasmid incorporated within the nanoparticles may still significantly affect gene transfer to cells. © 2007 Wiley Periodicals, Inc. J Biomed Mater Res 84A: 1038–1048, 2008

Key words: gene transfer; chitosan; nanoparticles; osteogenic protein-1; chondrocytes

INTRODUCTION

It is now well established that growth factors may play an important therapeutic role in the treatment of cartilage defects.[1,2] However, growth factors are subject to clinical limitations that include a short half-life *in vivo* requiring multi-dose administration and expense for the large quantities that may be required. These potential problems have stimulated interest in the implementation of gene transfer methods[3] to enable the local, sustained expression of the growth factors. While high transfection efficiencies can be readily achieved with viral vectors, the potential for untoward biological responses to the viral vector[4] has prompted investigation of non-viral transfection approaches. In contrast, the non-viral vectors may provide several advantages such as non-infectivity, absence of immunogenicity, the possibility of multi-dose administration, and low cost.[5]

Non-viral vectors including cationic liposomes, cationic lipids, and synthetic and natural polymers[6–8] have been employed as delivery vehicles for genes. The advantage of cationic lipids, such as Lipofectamine,[9] is that they have a high transfection efficiency *in vitro*. However, their biocompatibility profile *in vivo* has not yet been established.[10] One of the natural polymers employed as a non-viral vector is chitosan.[10–12] Chitosan is a naturally occurring polysaccharide consisting of two subunits, D-glucosamine

Correspondence to: M. Spector; e-mail: mspector@rics.bwh.harvard.edu
Contract grant sponsor: Rehabilitation Research and Development Service, U.S. Department of Veterans Affairs
Contract grant sponsor: Department of Defense

and *N*-acetyl-D-glucosamine, linked together by glycosidic bonds.[10] Its desirable attributes as a non-viral vector include[11]: a positive charge capable of condensing DNA with which it interacts and favoring interactions with the negative charge of the cell membrane; general biocompatibility; and ability to form nanometer[11,13–16] and micrometer[10,17] sized complexes with DNA. Moreover, chitosan-DNA nanoparticles did not induce release of proinflammatory cytokines from macrophages.[18] A host of other advantages of employing chitosan as a delivery vehicle have been proposed,[13] including: (1) conjugation of other molecules to the chitosan to interact with specific membrane receptors, including integrins, that could elicit selected cell behavior including receptor-mediated endocytosis; (2) incorporation of agents to inhibit the intracellular degradation of the plasmid; and (3) inclusion of other biologically active substances. Of interest is that chitosan was found to provide better transfection than a cationic liposome under certain conditions; whereas "cationic liposome (lipofectin)-associated gene expression was inhibited by serum, chitosan showed resistance to serum."[12]

The objective of the present study was to prepare chitosan nanoparticles incorporating a relatively small plasmid containing the gene encoding for the enhanced green fluorescent protein (EGFP) and/or a relatively large plasmid containing the gene for osteogenic protein (OP)-1 [also known as bone morphogenetic protein (BMP)-7], and to evaluate the ability to use these chitosan nanoparticles to transfect adult articular chondrocytes. Most of the nonviral strategies directed toward the transfection of chondrocytes for cartilage repair have been lipid or liposome-based methods.[19–22] The reason for selecting OP-1 for this investigation is that several studies have demonstrated the favorable effects of OP-1 on chondrogenesis *in vitro*[23–28] and on cartilage repair *in vivo*.[29–31] While there have been several reports of OP-1 gene transfer to cells using viral vectors,[32–36] there have been only two reports of nonviral tranfection of cells with OP-1 plasmid DNA,[37,38] and no studies investigating the use of nanoparticles as delivery vehicles for the gene. The relatively large size of the OP-1 plasmid used in this study (~9–10 kb)[38] compared to the plasmid size for EGFP (~4.7 kb) provided the opportunity to determine whether plasmid size has an effect on transfectibility using chitosan nanoparticles.

The emphasis in the current study was the methodology for preparing nanoparticles incorporating a relatively large plasmid, and the effects of the conditions under which the nanoparticles were produced on their characteristics (*viz.*, size and shape). One of the specific aims of the study was to determine how the chitosan: plasmid OP-1 (pOP-1) ratio affected the size, morphology, and charge of the nanoparticles. A second aim of the study was to assess the structural integrity of the OP-1 complexed with chitosan using gel electrophoresis. The third aim of the study was to demonstrate by fluorescence microscopy and ELISA the functionality of the chitosan nanoparticles encoding EGFP and pOP-1, respectively, using adult articular chondrocytes. There has been only one prior report of the uptake of nanoparticles by chondrocytes[39] incorporating the relatively small plasmid for EGFP (pEGFP). This study investigates the incorporation and characterization of a plasmid much larger than pEGFP into chitosan nanoparticles and evaluates the effectiveness of the nanoparticles in transfecting chondrocytes *in vitro*.

MATERIALS AND METHODS

Preparation of chitosan nanoparticles containing pOP-1 and a fluorescent label

Chitosan stock solution (0.2%, w/v) was made as follows. Ten milligrams of medium to high molecular weight chitosan (Cat. No. 41,796-3, Sigma-Aldrich, St. Louis, MO) was added to a tube containing 11.6 μL acetic acid in 4.0 mL water and then kept at 37°C overnight. After the chitosan was dissolved, 0.028 gm of sodium acetate (Fisher Scientific, Fair Lawn, NJ) was added to the tube, the pH was adjusted to 5.5, and the volume increased to 5 mL. Chitosan working solutions with different concentrations were made from the stock by dilution with 5 m*M* acetate buffer (pH 5.5) and sterile filtered.

The pOP-1, (pW24, Cell & Molecular Technologies, Phillipsburg, NJ) working solution (200 μg/mL) was prepared with filtered 5 m*M* sodium sulfate (Fisher Scientific). The size of the plasmid, estimated by Cell & Molecular Technologies based on three restriction enzyme preparations was: 10,346 bp (HindIII restriction enzyme), 9406 bp (PstI) and 7793 bp (EcoRI). A complex coacervation method previously described[40] was used to make chitosan nanoparticles complexing the pOP-1. Complex coacervation is the separation caused by the interaction of two oppositely charged colloids. Briefly, 100–150 μL chitosan and pOP-1 solutions were heated separately at 55°C for 30–45 min. Equal volumes of both solutions were quickly mixed together and vortexed for 30–45 s. The nanoparticles were used without further purification.

Fluorescein-5-isothiocyanate (FITC) was added to the nanoparticles along with the OP-1 plasmid using the following procedure.[18] Forty milligrams FITC (Sigma-Aldrich) was dissolved in 5 mL dimethylsulfoxide, and 0.5 mL chitosan (0.1%) solution was added, and the mixture was stirred for 1–2 h. The FITC-labeled chitosan was then precipitated with 25 mL NaOH solution at pH 8. After centrifugation of the precipitated product at 4800 rpm for 15 min the supernatant solution was discarded. The pellet was washed three times with 25 mL distilled water. The resulting chitosan was resuspended in acetate buffer and then used to prepare nanoparticles incorporating pOP-1, as described above.

The plasmid encoding for EGFP (Clontech, Mountain View, CA), with a plasmid size of 4.7 kb, was used as a reporter gene to transfect chondrocytes. The plasmid was amplified in Escherichia coli host strain DH5α, and purified using the QIAfilter plasmid Mega kit (Qiagen, Valencia, CA). The EGFP and OP-1 plasmids were incorporated into the same chitosan nanoparticle (chitosan:total plasmid weight ratio of 10:1 and a pEGFP:pOP-1 weight ratio of 7:3) in order to track the transfection of the chondrocytes by the chitosan nanoparticles via fluorescence. Realizing that plasmid size may have an effect on gene transfer and that GFP expression alone would not verify that the OP-1 plasmid was incorporated or expressed by the transfected chondrocytes, chitosan nanoparticles incorporating OP-1 plasmid alone were similarly synthesized and used for transfection in order to directly assess the overexpression of the larger OP-1 plasmid by ELISA.

Electrophoresis of nanoparticles and plasmid stability

Incorporation of the pOP-1 into chitosan nanoparticles was studied using agarose gel electrophoresis. Two issues were addressed through experimentation: the retention of the plasmid in chitosan nanoparticles prepared with various amounts of the plasmid, and the structure of the plasmid after being released by the chitosan. Integrity of the plasmid released from the nanoparticles was determined using restriction enzymes. For each gel, naked pOP-1 (0.8 μg in 80 μL 5 m*M* sodium sulfate solution) was used as the control. A 1 kb DNA Ladder (Cat. No. 10381-010, Invitrogen, Carlsbad, C) was also run on each gel in parallel.

Increasing amounts of chitosan were mixed with a single quantity of pOP-1 (10 μg), to yield the following weight ratios of chitosan to pOP-1: 0.5:1; 1:1; 2:1; 5:1; 10:1; 20:1; and 40:1. The nanoparticles were loaded onto a 0.8% agarose gel in tris-borate-ethylenediamine tetraacetic acid, EDTA (TBE) buffer (×1) with ethidium bromide. The gel was run at 100 V for 60–80 min, and then photographed with Foto/Analyst Visionary (Fotodyne, New Berlin, WI).

The structural integrity of pOP-1 released from the nanoparticles was also investigated by electrophoresis. To digest the chitosan,[40,41] 80 μL of the nanoparticle suspensions of the various chitosan:pOP-1 ratios equivalent to 0.8 μg pOP-1 was added to 8 μL chitosanase (0.24 U/mL, Sigma-Aldrich) and 20 μL lysozyme (100 U/mL, Sigma-Aldrich) in 5 m*M* sodium acetate buffer (pH 5.5). The mixture was incubated at 37°C for 4 h. The digest solutions were then run on the gel.

Samples of the stock pOP-1 solution and aliquots (16 μL) of the digest solutions from each of the nanoparticle-pOP-1 preparations were cut with Hind (III) restriction endonuclease (New England BioLabs, Ipswich, MA) and run on gels. Samples of the stock plasmid were also cut with SalI, XhoI BamHI and EcoRI restriction enzymes, and analyzed by gel electrophoresis as described above, in order to estimate the size of the plasmid.

Environmental scanning electron microscopy

Environmental scanning electron microscopy (ESEM, XL30, FEI/Philips, Hillsboro, OR) was used to investigate the size and shape of the nanoparticles. Samples were prepared by placing 1 μL of the nanoparticle suspension onto a slide and air drying the preparation. The air-dried samples were then observed directly under ESEM, without the need to apply a conductive coating. Nanoparticles with chitosan:plasmid weight ratios of 5:1, 10:1, and 20:1 were examined by ESEM.

Determination of nanoparticle size distribution

The particle size distribution was determined by the dynamic light scattering technique performed at 25°C with a Brookhaven 200SM goniometer, a BI-9000AT digital auto-correlator, and Spectra-Physics Argon laser operating at 514 nm (Brookhaven Instruments Corporation, Holtsville, NY). The measured scattering intensities were analyzed by the software provided by Brookhaven Instruments Corporation. Nanoparticles with chitosan: plasmid weight ratios of 5:1, 10:1, and 20:1 were evaluated for their particle size distribution.

Zeta potential

The zeta potential of the nanoparticles, reflecting their charge, was measured with Brookhaven's Zeta Plus apparatus (Brookhaven Instruments Corporation). The electrophoretic mobility of nanoparticles, with chitosan:plasmid weight ratios of 5:1, 10:1, and 20:1, in acetate buffer (pH 5.5) was determined at 25°C. A pH 5.5 was used because this was the pH at which the nanoparticles were made. The zeta potential was calculated using the Hückel approximation for small particles in low dielectric constant medium.

Chondrocyte uptake of nanoparticles incorporating FITC and plasmids for enhanced green fluorescent protein and OP-1

Chondrocytes were obtained by enzymatic digestion of the articular cartilage obtained from the knee joint of one adult dog. The cells were expanded in number in monolayer culture using a modification of the medium previously reported,[42] consisting of Dulbecco's modified Eagle's medium, DMEM (4.5%, without L-glutamine and with 1 m*M* sodium pyruvate), 0.1 m*M* nonessential amino acids, 10 m*M* *N*-2-hydroxyehtylpiperazine-*N*′-2-ethanesulfonic (HEPES) buffer, 100 U/mL penicillin, 100 μg/mL streptomycin glutamate, 10% FBS (Invitrogen Corporation, Carlsbad, CA), and a mixture of the following growth factors (R&D Systems, Minneapolis, MN): TGF-β1 (1 ng/mL), FGF-2 (5 ng/mL) and PDGF-bb (10 ng/mL). Chondrocytes subcultured once (passage 1) were used in this investigation.

Twenty-four hours prior to addition of the nanoparticles to the cultures, the cells were seeded onto glass-bottomed dishes (14-mm diameter wells; MatTek Corporation, Ashland, MA) at a density of 5×10^4 cells per dish. The cells were cultured in the medium described above. At 80–90% confluence, the medium was removed and replaced with a

250-μL suspension of fluorescence-labeled nanoparticles in serum-free medium consisting of high glucose DMEM (4.5%, without L-glutamine and with 1 m*M* sodium pyruvate), 0.1 m*M* nonessential amino acids, 10 m*M* HEPES buffer, 100 U/mL penicillin, 100 μg/mL streptomycin glutamate, ITS^{+1} (100×, by Sigma Chemical, St. Louis, MO), 0.1 m*M* ascorbic acid 2-phosphate, 1.25 mg/mL bovine serum albumin, 10 ng/mL of TGF-β1, and 100 n*M* dexamethasone. Four hours later, another 250 μL of serum-free medium was added. After an additional 20-h incubation period, the chondrocytes were rinsed with phosphate-buffered saline (PBS) and 500 μL of serum-free medium added. For control experiments, nanoparticles without FITC and an FITC solution alone were used. Nanoparticle uptake by the chondrocytes was examined by fluorescence microscopy and confocal laser scanning microscopy.

Chondrocytes were also cultured with the nanoparticles which contained the EGFP and OP-1 plasmids together in the same nanoparticle or with nanoparticles incorporating OP-1 plasmid alone using the same culture conditions as described above. In control cultures, EGFP plasmid alone (i.e., not incorporated into nanoparticles) or combined with a lipid transfection reagent (GenePorter®; Gene Therapy Systems, San Diego, CA) was added directly to the cultures. Transfected cells were examined by transmitted fluorescence microscopy.

For cultures transfected with OP-1 plasmid nanoparticles, media were collected 1, 3, 5, and 7 days after transfection and assessed for OP-1 protein using a DuoSet human ELISA kit (R&D Systems, Minneapolis, MN). For a positive control group, chondrocytes were transfected with OP-1 plasmid using the GenePorter transfection reagent according to the manufacturer's instructions. For a negative control group, cultures were not treated with any transfection reagent or plasmid.

RESULTS

Electrophoresis of the OP-1 plasmid released from the nanoparticles

The naked OP-1 plasmid in the stock solution was found to move slowly in the electrophoretic gel, likely due to the coiled configuration [Fig. 1(a,b)]. After the digestion with restriction enzymes, the size of plasmid in the stock solution was estimated by summing the sizes of the prominent linear fragments: 14,500 bp (XhoI); 13,800 bp (BamHI); 12,800 bp (EcoRI); 12,200 bp (SalI); and 11,500 bp [Hind (III)]. The size of the plasmid released from the digestion of the nanoparticles was estimated to be about 11,500 bp using the Hind (III) enzyme.

The interaction between chitosan and pOP-1 was evaluated by agarose gel electrophoresis (Fig. 1). At the lowest weight ratio of chitosan to pOP-1 of 0.5:1, [lane 2 of Fig. 1(a)] some of the pOP-1 was released from the nanoparticles and migrated into the gel as demonstrated by a faint band [asterisk in Fig. 1(a)]

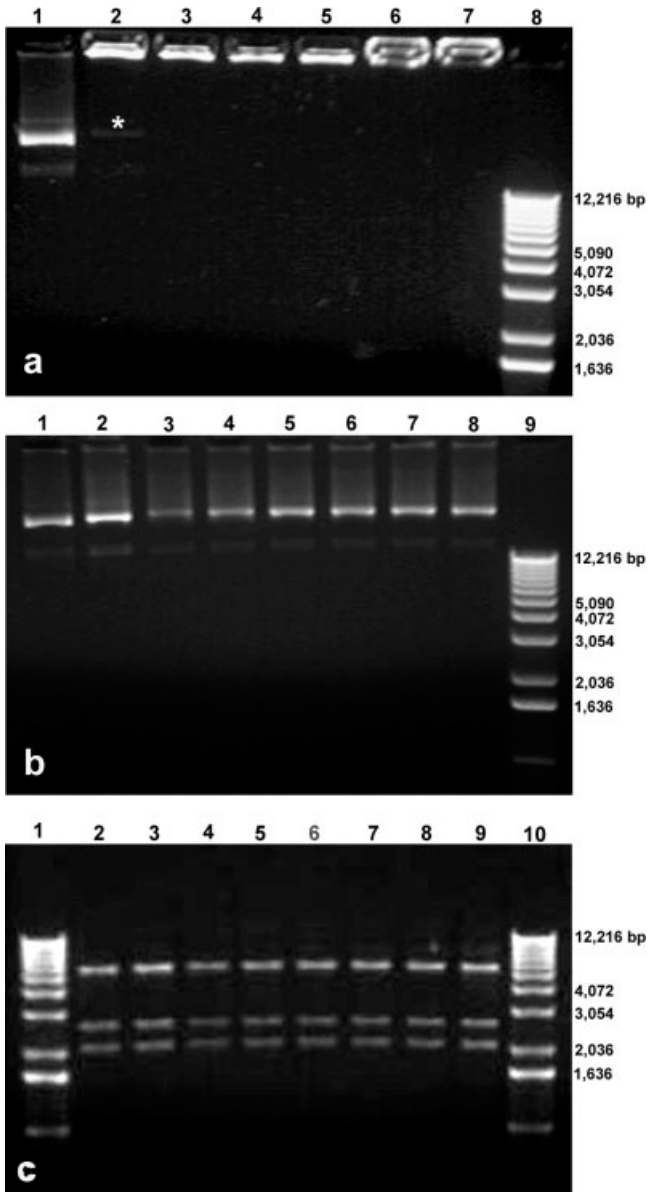

Figure 1. (a) Retention of the OP-1 plasmid in the chitosan nanoparticles as analyzed by agarose gel electrophoresis. Lane 1 demonstrates the migration of the naked pOP-1. Lanes 2–7 were loaded with nanoparticles made up of plasmid complexed with progressively increasing amounts of chitosan with chitosan:pOP-1 ratios of 0.5:1, 1:1, 2:1, 5:1, 10:1, and 20:1, respectively. Lane 8 shows the 1 Kb ladder. Only in lane 2 with the lowest amount of chitosan complexed to the plasmid, was any plasmid released as demonstrated by its migration (asterisk). (b) Electrophoresis analysis of plasmid recovered from nanoparticles after digestion of the chitosan by treatment with chitosanase and lysozyme. Lane 1 is the stock pOP-1. Lane 2 was loaded with the stock pOP-1 treated with the chitosanase and lysozyme. The enzymatic digest from nanoparticles with chitosan:pOP-1 ratios of 0.5:1, 1:1, 2:1, 5:1, 10:1, and 20:1, were loaded in lanes 3–8, respectively. Lane 9 shows the 1 kb ladder. (c) Restriction enzyme Hind (III) digestion of pOP-1 released from nanoparticles. Lanes 1 and 10 are the 1 Kb ladder. Lane 2: restriction enzyme cleavage of stock pOP-1; lane 3: cleavage of pOP-1 treated with the chitosanase and lysozyme; lanes 4–9: pOP-1 from digested nanoparticles with chitosan:pOP-1 ratios of 0.5:1, 2:1, 5:1, 10:1, 20:1, and 40:1, respectively.

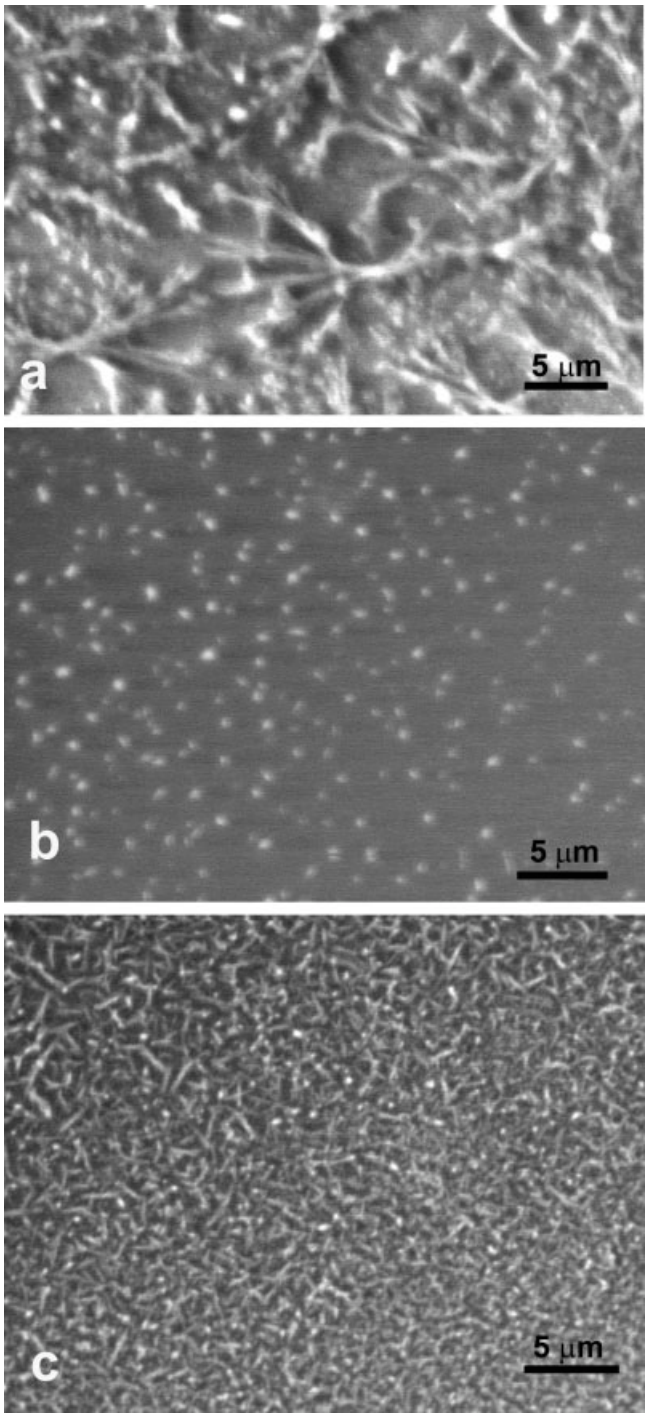

Figure 2. Environmental scanning electron microcopy images of nanoparticles incorporating pOP-1, prepared with different chitosan:pOP-1 ratios. (a) chitosan:pOP-1 ratio of 5:1; (b) chitosan:pOP-1 ratio of 10:1; and (c) chitosan: pOP-1 ratio of 20:1.

corresponding to the location of the naked plasmid control [lane 1 of Fig. 1(a)]. With an increasing chitosan:plasmid ratio [lanes 3–7 of Fig. 1(a)], there was no sign of migration of the pOP-1 plasmid, indicating that it remained within the nanoparticles. A 1:1 ratio of chitosan to pOP-1 [lane 3 of Fig. 1(a)] appeared to be sufficient to retain most of the plasmid in the polymer nanoparticles.

The electrophoretic mobility of the plasmid released by enzymatically digesting the nanoparticles [lanes 3–8 of Fig. 1(b)] was comparable to the stock plasmid [lane 1 of Fig. 1(b)] and the stock pOP-1 treated with the digestion enzymes [lane 2 of Fig. 1(b)]. This indicated that incorporation of the plasmid into the chitosan nanoparticles, and its release by enzymatic digestion of the chitosan, did not alter the structural integrity of the plasmid. There was no noticeable difference in the location of the bands from the released plasmid [lanes 3–8 of Fig. 1(b)] when compared to the stock control plasmids [lanes 1 and 2 of Fig. 1(b)].

After Hind (III) restriction enzyme cleavage of the plasmid recovered from enzymatic digestion of the nanoparticles, the molecular profiles [lanes 4–9 of Fig. 1(c)] were found to be similar to that of the original pOP-1 [lane 2 of Fig. 1(c)].

Morphology of the chitosan-pOP-1 nanoparticles

ESEM revealed various morphologies of the nanoparticles prepared with chitosan:plasmid weight ratios of 5:1, 10:1, and 20:1 [Fig. 2(a–c)]. The nanoparticles with the chitosan:plasmid ratio of 10:1 were generally uniform in size and less than 500 nm in diameter [Fig. 2(b)]; this small size and low atomic number precluded higher magnification imaging of the nanoparticles in the ESEM. Also of interest was the fact that the small particles did not display a tendency to aggregate [Fig. 2(b)]. In contrast, nanoparticles prepared with the lower chitosan:plasmid weight ratio of 5:1 demonstrated varied morphologies with some spherical particles approximately twice the diameter of the 10:1 particles and other nanoparticles with a fibrous and branching structure, about 500 nm in width and up to 10 μm long [Fig. 2(a)]. Nanoparticles prepared with the higher chitosan:plasmid weight ratio of 20:1 also displayed a fibrous and branching structure but of a substantially smaller size than the 5:1 particles, with the length of the features being about 1 μm [Fig. 2(c)]. In the case of the 20:1 particles the branching morphology may have been the result of aggregation of elongated or fibrous particles [Fig. 2(c)].

Particle size distribution

Dynamic light scattering revealed that the chitosan-OP-1 nanoparticles were polydisperse in size, with widely varying ranges of diameter based on the chitosan:pOP-1 ratio (Fig. 3). The smallest average particle diameter (Table I) and greatest percentage of

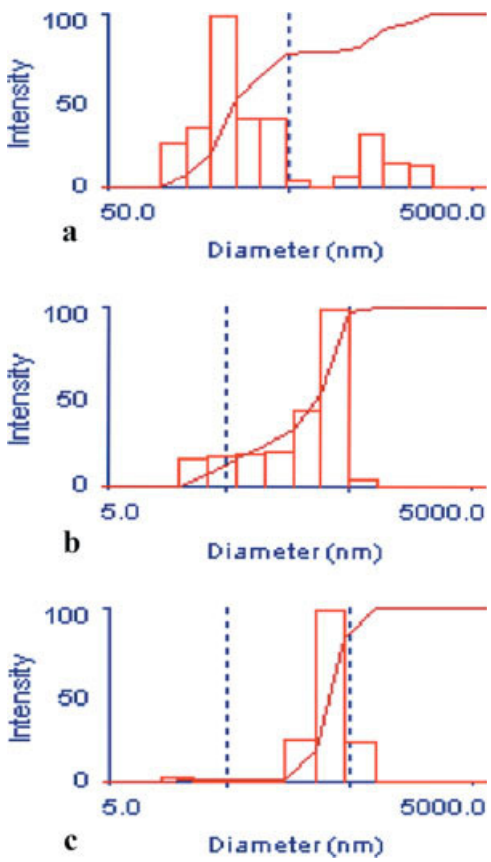

Figure 3. Analysis of particle size and size distribution by dynamic light scattering technique. The histograms show a measure of the relative number of particles (noted as "Intensity" ordinate) with diameters in the graduated diameter ranges (abscissa). Nanoparticles made at different ratios: (a) chitosan:pOP-1 ratio of 5:1; (b) chitosan:pOP-1 ratio of 10:1; and (c) chitosan:pOP-1 ratio of 20:1. [Color figure can be viewed in the online issue, which is available at www.interscience.wiley.com.]

nanoparticles of smallest diameter [Fig. 3(b)] were recorded for the chitosan:pOP-1 nanoparticles with the 10:1 ratio. This was consistent with the ESEM findings (Fig. 2). Nanoparticles prepared with a chitosan:pOP-1 ratio of 10:1 displayed an average diameter of 240 nm with a range of 25–613 nm (Table I). The preparation with the chitosan:pOP-1 ratio of 20:1, however, also appeared to comprise nanoparticles of comparably small size (Table I), with an average of 325 nm and a range of 18–562 nm (Table I). This would suggest that the larger branched particles seen in ESEM [Fig. 2(c)] were aggregate of smaller sized particles. As suggested by ESEM, the light scattering results demonstrated that the particles prepared with a chitosan:pOP-1 ratio of 5:1 were twice the diameter of the nanoparticles with a ratio of 10:1 (Table I). Moreover, light scattering showed that the range of diameters of the nanoparticles with the 5:1 ratio (114–2553 nm), was substantially higher than the range for the 10:1 nanoparticles (Table I).

Charge of the nanoparticles

The zeta potential of original chitosan solution (pH 5.5) was 45.5 ± 1.1 mV. When the chitosan was coupled with the negatively charged pOP-1, the surface charge decreased to approximately one-half this value (Table I). Interestingly, with the increasing chitosan-plasmid weight ratio, the surface charge of the nanoparticles did not change much (Table I); the three nanoparticle preparations decreased to about 20 mV.

Chondrocyte uptake of nanoparticles

Based on an average nanoparticle diameter and a chitosan density of about 0.3 gm/mL, we roughly estimated that the number of nanoparticles added to the chondrocyte monolayer was on the order of 10^{10}. Assuming that the cultures to which the nanoparticles were added contained approximately 100,000 cells, the number of nanoparticles per cell was estimated to be 100,000. The chondrocyte uptake of nanoparticles containing both OP-1 plasmid and FITC was observed by fluorescence microscopy using FITC-labeled chitosan-plasmid nanoparticles [Fig. 4(a)]; as to be expected, no fluorescence was detected in the cultures in which the chitosan nanoparticles alone (without incorporation of FITC) were administered to the cells. The fluorescence images of the experimental cultures in which the FITC-labeled nanoparticles were used [Fig. 4(a)], demonstrated that the nanoparticles had been endocytosed by virtually all of the chondrocytes after 24 h of incubation of the cells with the nanoparticles. This was demonstrated in the microscope by switching between the visible light and ultraviolet sources, in order to view all of the cells and then those fluorescing. In contrast the fluorescence from the chondrocytes treated with FITC solution alone appeared to come principally from the surface of the cells [Fig. 4(b)].

Confocal laser scanning microscopy was used to more clearly observe the intracellular distribution of the chitosan nanoparticles incorporating FITC.

TABLE I
Light Scattering and Zeta Potential Results for Nanoparticles with Chitosan:Plasmid Ratios of 5:1, 10:1, and 20:1

	5:1	10:1	20:1
Light scattering			
Average diameter (nm)	546	240	325
Range (nm)	114–2553	25–613	18–562
Zeta potential (mv)[a]	22.9 ± 2.3	21.4 ± 1.7	24.4 ± 1.0

[a]The zeta potential of the original chitosan solution (pH 5.5) was 45.5 ± 1.1 mv (mean ± standard error of mean).

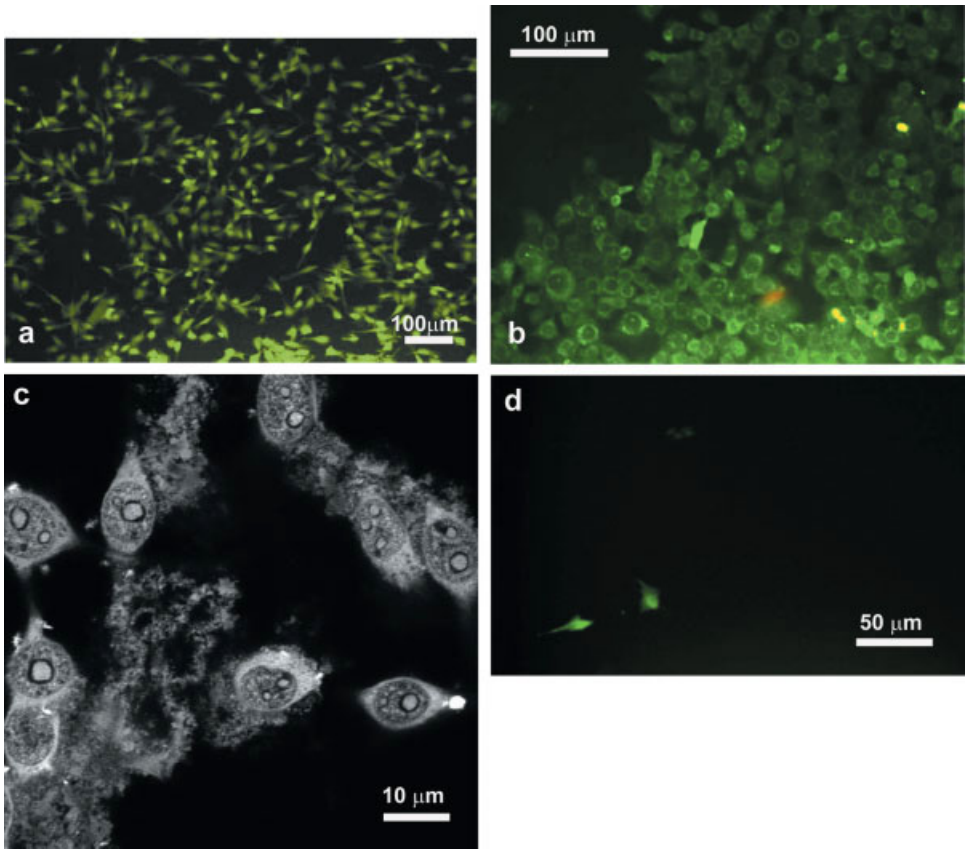

Figure 4. (a) Fluorescence microscopy of chondrocyte uptake of FITC-labeled pOP-1 containing nanoparticles 24 h post incubation. (b) Fluorescence microscopy of chondrocyte uptake of FITC-solution alone 24 h post incubation. (c) Confocal images of FITC-labeled nanoparticles showing intracellular distribution in chondrocytes after 24 h incubation. (d) Fluorescence microscopy of chondrocytes transfected by chitosan nanoparticles containing pEGFP and pOP-1 post 84 h cell culture. [Color figure can be viewed in the online issue, which is available at www.interscience.wiley.com.]

Confocal microscopy was necessary to demonstrate that the FITC-labeled nanoparticles were in the cell and not merely adsorbed onto the cell membrane. This could not be concluded from fluorescence microscopy. The confocal images showed that the FITC was distributed throughout the cytoplasm, and was also taken up into the nucleus of the chondrocytes [Fig. 4(c)].

Control cultures to which the EGFP plasmid was added as a solution (*i.e.*, not incorporated into nanoparticles) did not display fluorescence. In contrast, the results showed EGFP expression in chondrocytes that were exposed to the nanoparticles which contained the EGFP and OP-1 plasmids in the same nanoparticle, indicating the capability of the chitosan nanoparticles to deliver the genes to the cells. Fluorescence microscopy revealed expression of EGFP in chondrocytes after 84 h of transfection [Fig. 4(d)]. Although EGFP expression was achieved using the chitosan nanoparticles as the gene delivery vehicle, chondrocytes transfected with nanoparticles incorporating OP-1 plasmid alone did not show overexpression of OP-1 (by assaying for the protein in the media by ELISA) up to 1 week of culture. The positive controls (cells transfected with the OP-1 plasmid delivered by the GenePorter transfection reagent) displayed OP-1 in the media at day 1 (13.4 $\pm$ 3.3 ng/mL, $n = 3$; mean $\pm$ std. dev.) and on day 3 (6.1 $\pm$ 1.4 ng/mL, $n = 4$), but not in any of the other collection time points (5 and 7 days of culture). Based on the negative controls, there was no constitutive expression of OP-1 by these cells in monolayer (i.e., no OP-1 released by chondrocytes not treated with any transfection reagent or plasmid).

DISCUSSION

The OP-1 plasmid employed in the current study was of relatively large size, estimated to be 12–14 kb. The plasmid has been employed in the commercial production of recombinant human OP-1 by Stryker Biotech (Hopkinton, MA). The reason for the specific structure of the plasmid and the requirements for its large size were outside the scope of the project. A recent study[38] investigating co-transfection of rat calvarial cells with the genes for OP-1 and

insulin-like growth factor (IGF)-1, used a modified form of the pW24 OP-1 plasmid that we used in the current work. In the prior experiment pW24 was digested with the restriction enzyme, Xho1. The OP-1 coding sequence was purified on agarose gels and re-ligated with the cytomegalovirus (CMV) promoter to produce a plasmid, that itself was rather large at 9.1 kb. That genes for critically important growth factors such as OP-1 may be of certain value in plasmids of large size compels the investigation of methodology for incorporating large plasmids into nanoparticles, which themselves may offer unique benefits for selected applications.

It was, therefore, of note in the current study that a plasmid of such a large size could be incorporated into nanoparticles. The advantage of chitosan for this application is that the positive charge of chitosan acted to condense the large negatively charged OP-1 plasmid such that it could be incorporated into nanoparticles. The OP-1 plasmid may be one of the largest plasmids that has ever been coupled with chitosan nanoparticles.

In general, migration of plasmid DNA on a gel can be retarded by the charge and/or molecular configuration and/or formation of complexes. When the stock plasmid was cleaved by restriction enzymes, the linear fragments displayed a characteristic electrophoretic profile. The avidity with which the pOP-1 was incorporated into the chitosan nanoparticles was demonstrated by the fact that free plasmid was evident on the electrophoretic gel only for the nanoparticles formulated with the lowest chitosan-plasmid ratio of 0.5:1. In nanoparticles with higher contents of chitosan, the polymer may have acted to condense the negative plasmid to a greater extent through electrostatic interactions thus resulting in higher affinity incorporation. A chitosan:plasmid weight ratio of at least 1:1 was necessary to complex the plasmid completely. Owing to the large size of the plasmid, this higher amount of chitosan may have been required to condense the pOP-1 enough to form nanoparticles.

Of importance is the finding that incorporation of pOP-1 into nanoparticles with all of the chitosan-plasmid ratios did not affect the structure of the plasmid. The electrophoretic migration of pOP-1 (1) in the digests from the enzymatic breakdown of the nanoparticles, and (2) in the restriction enzyme treated digests, matched the respective pOP-1 controls. These findings indicate that controlled release of pOP-1 from chitosan nanoparticles, that can be regulated, in part, by the chitosan:plasmid ratio, can be accomplished without affecting plasmid integrity, although further studies were still necessary to directly determine the functionality of the plasmid by assessing OP-1 protein expression. It will be interesting in future work to investigate the optimal conditions for preparing nanoparticles for incorporation of plasmids of varying size.

In this study, varying the chitosan:plasmid ratios had a noticeable effect on the morphology and size of the pOP-1-containing nanoparticles. The chitosan:plasmid mass ratio has been investigated by various groups as a important factor in the formulation of chitosan nanoparticles. Prior work has varied the chitosan:plasmid value from 2:1[40,43] to 5:1,[44] and from 0.05:1 to 2.5:1 in experiments incorporating the same plasmid.[41] In the present work, nanoparticles formulated with a chitosan:plasmid ratio of 10:1 were of uniformly small size (less than 250 nm) and spherical shape. This diameter was larger than that of earlier reports of 50–100 nm of chitosan nanoparticles containing the marker gene luciferase.[11] This size difference may be due to the bigger size of the OP-1 plasmid. However, we also found in the present study, that the size and morphology, and apparent state of aggregation, varied dramatically with increased or decreased chitosan:plasmid ratio.

The small uniform spherical nanoparticles prepared with a chitosan:plasmid ratio of 10:1 had a positive charge, which may facilitate the binding of the nanoparticles to the negatively charged cells. The value of the positive charge was comparable to that recorded (23–24 mV at pH 5.0) for plasmid (luciferase)-chitosan complexes, several micrometers in diameter.[10] In the present study the positive charge of the nanoparticles did not change much even with increasing chitosan-plasmid weight ratio. This result was in accordance with the former published data, which exhibited a zeta potential plateau in the presence of excess chitosan.[45] Future work will be required to determine how the size, morphology and charge affect interactions with cells and performance of the nanoparticles as delivery vehicles of plasmid.

One of the findings of interest was the ability of the chitosan nanoparticles to gain entry into adult canine articular chondrocytes. This was demonstrated using chitosan nanoparticles incorporating FITC in addition to the OP-1 plasmid, confirming a recent study incubating rabbit chondrocytes with chitosan particles.[39] The FITC-labeled chitosan nanoparticles, which also contained the OP-1 plasmid, were found in virtually all of the cells after 24 h of incubation with the nanoparticles. The fluorescence appearance of the chondrocytes containing the FITC-labeled chitosan nanoparticles was similar to the fluorescence microscopy of phagocytic macrophages engulfing chitosan-FITC nanoparticles[18] and tumor cell uptake of FITC-labeled chitosan microspheres.[10] Transmission electron microscopy studies demonstrated the mechanism of uptake of chitosan-DNA nanoparticles by HeLa human cervix epitheliod cells to be spontaneous endocytosis[11] with the nanoparticles being collected in invaginations of the plasma membrane. Once inside

the cytoplasm the nanoparticles were found in "small vesicles and large endosomal compartments."[11] Of importance was the finding that other cell types (tumor cells) did not similarly endocytose the same chitosan-DNA nanoparticles[11] indicating that not all cell types are transfected by these nanoparticles. Other prior work using chitosan-luciferase plasmid complexes (microspheres) also considered the mechanism of cell uptake to be endocytosis[10] with the subsequent endosomal release of the plasmid and nuclear transport. Using one type of tumor cell, these processes were found to be affected by the molecular mass of chitosan, plasmid concentration, the stoichiometry of the complex, and serum concentration and pH of the transfection medium.[10]

Confocal microscopy of the chondrocytes containing the FITC-labeled pOP-1-containing chitosan nanoparticles also revealed FITC-related fluorescence in the nucleus of the cells. A similar finding of FITC-related fluorescence in the nucleus of cells has been reported for FITC-labeled chitosan-plasmid complexes, of the order of 5–8 μm in diameter, used to transfect tumor cells.[10] This indicated that the FITC released by the chitosan nanoparticles (in the present study) or from the chitosan microspheres[10] in the cytoplasm had subsequently diffused into the nuclear compartment. However, in the present study there remains the possibility that the nanoparticles had entered the nucleus. This needs to be a topic for future research.

A notable finding of the present work was the expression of EGFP by the chondrocytes treated with nanoparticles incorporating the plasmids of both EGFP and OP-1. Control cultures containing the EGFP plasmid alone did not display fluorescence, indicating the likelihood that expression was the result of EGFP plasmid delivered by the nanoparticles. While the transfection efficiency was low, the very fact that some cells demonstrated the expression of EGFP suggested that the chitosan nanoparticles can gain entry into adult articular chondrocytes and the incorporated EGFP plasmid can gain entry into the nucleus and result in expression of the protein. EGFP was expressed very slowly, however, with chondrocytes beginning to synthesize the protein after 84 h. Based on the other results showing that the nanoparticles gained entry into most of the cells after 24 h, our supposition is that the complex between chitosan and the plasmid was so stable as to only allow a slow release of the plasmid in the cell. Based on this hypothesis, it would be of interest in future studies to prepare nanoparticles with a less positively charged polymer.

For chondrocytes transfected with nanoparticles incorporating pOP-1 alone, overexpression of OP-1 was not detected in the media by our ELISA assays; there may have been small amounts of OP-1 expressed that were below the detection limits of the ELISA assay. The fact that OP-1 expression was detected in cultures transfected with the GenePorter transfection reagent indicates that the OP-1 plasmid used was functional and able to transfect chondrocytes. One explanation for the findings may be that the interaction between OP-1 plasmid and the chitosan nanoparticles resulted in a slower release profile of the plasmid compared to the GenePorter transfection reagent. Overexpression may, therefore, only occur at later time points for nanoparticle-transfected cells. This supposition is supported by the observation that when the GenePorter reagent was used to transfect chondrocytes with the EGFP plasmid, there was earlier and stronger fluorescence compared to cells transfected with the EGFP-chitosan nanoparticles. That fluorescence was detected but no OP-1 was found in the medium in cultures transfected with nanoparticles incorporating the EGFP and OP-1 plasmids, may also indicate the importance of plasmid size on gene transfer to chondrocytes using chitosan nanoparticles. Future work needs to investigate transfection using chitosan nanoparticles with varying plasmid sizes.

CONCLUSIONS

In conclusion, chitosan nanoparticles incorporating plasmid OP-1 can be prepared with a range of diameters and morphologies by adjusting the chitosan:-plasmid ratio. The OP-1 plasmid maintains its structural integrity after incorporation into the chitosan nanoparticle. A chitosan:plasmid weight ratio of 10:1 yields non-aggregating spherical nanoparticles of uniform size less than 250 nm. These particles can gain entry into adult articular chondrocytes and can result in expression of the plasmid carried by the nanoparticles, although expression also seems to be mediated by the size of incorporated plasmid.

The authors appreciate the assistance of Erika Marsillio, Ph.D., for advice regarding the structural integrity of the plasmids, and JianYi Cui and Hao Wang, Ph.D., of the Department of Materials Science and Engineering at the Massachusetts Institute of Technology for assistance with light scattering and the zeta potential measurements. Ximing Xu received support as a Visiting Associate Professor at Harvard Medical School from the Jiangsu Municipal Government and Jiangsu University, Zhenjiang, China. The authors are grateful to Stryker Biotech, Hopkinton, MA, for providing the OP-1 plasmid.

References

1. O'Connor WJ, Botti T, Khan SN, Lane JM. The use of growth factors in cartilage repair. Orthop Clin North Am 2000;31: 399–410.

2. van den Berg WB, van der Kraan PM, Scharstuhl A, van Beuningen HM. Growth factors and cartilage repair. Clin Orthop Relat Res 2001;391(Suppl):S244–S250.
3. Evans CH, Ghivizzani SC, Smith P, Shuler FD, Mi Z, Robbins PD. Using gene therapy to protect and restore cartilage. Clin Orthop 2000;379 Suppl:S214–S219.
4. Cottard V, Valvason C, Falgarone G, Lutomski D, Boissier MC, Bessis N. Immune response against gene therapy vectors: Influence of synovial fluid on adeno-associated virus mediated gene transfer to chondrocytes. J Clin Immunol 2004;24:162–169.
5. Pouton CW, Seymour LW. Key issues in non-viral gene delivery. Adv Drug Deliv Rev 1998;34:3–19.
6. Partridge KA, Oreffo RO. Gene delivery in bone tissue engineering: Progress and prospects using viral and nonviral strategies. Tissue Eng 2004;10:295–307.
7. Trentin D, Hubbell J, Hall H. Non-viral gene delivery for local and controlled DNA release. J Control Release 2005; 102:263–275.
8. Samuel RE, Lee CR, Ghivizzani S, Evans CH, Yannas IV, Olsen BR, Spector M. Delivery of plasmid DNA to articular chondrocytes via novel collagen-glycosaminoglycan matrices. Hum Gene Ther 2002;13:791–802.
9. Behr JP, Demeneix B, Loeffler JP, Perez-Mutul J. Efficient gene transfer into mammalian primary endocrine cells with lipopolyamine-coated DNA. Proc Natl Acad Sci USA 1989;86: 6982–6986.
10. Ishii T, Okahata Y, Sato T. Mechanism of cell transfection with plasmid/chitosan complexes. Biochim Biophys Acta 2001;1514:51–64.
11. Erbacher P, Zou S, Bettinger T, Steffan AM, Remy JS. Chitosan-based vector/DNA complexes for gene delivery: Biophysical characteristics and transfection ability. Pharm Res 1998;15:1332–1339.
12. Sato T, Ishii T, Okahata Y. In vitro gene delivery mediated by chitosan. effect of pH, serum, and molecular mass of chitosan on the transfection efficiency. Biomaterials 2001;22:2075–2080.
13. Leong KW, Mao HQ, Truong-Le VL, Roy K, Walsh SM, August JT. DNA-polycation nanospheres as non-viral gene delivery vehicles. J Control Release 1998;53:183–193.
14. Guliyeva U, Oner F, Ozsoy S, Haziroglu R. Chitosan microparticles containing plasmid DNA as potential oral gene delivery system. Eur J Pharm Biopharm 2006;62:17–25.
15. Bozkir A, Saka OM. Chitosan nanoparticles for plasmid DNA delivery: Effect of chitosan molecular structure on formulation and release characteristics. Drug Deliv 2004;11:107–112.
16. Mansouri S, Cuie Y, Winnik F, Shi Q, Lavigne P, Benderdour M, Beaumont E, Fernandes JC. Characterization of folate-chitosan-DNA nanoparticles for gene therapy. Biomaterials 2006;27:2060–2065.
17. Ozbas-Turan S, Aral C, Kabasakal L, Keyer-Uysal M, Akbuga J. Co-encapsulation of two plasmids in chitosan microspheres as a non-viral gene delivery vehicle. J Pharm Pharm Sci 2003;6:27–32.
18. Chellat F, Grandjean-Laquerriere A, Le Naour R, Fernandes J, Yahia L, Guenounou M, Laurent-Maquin D. Metalloproteinase and cytokine production by THP-1 macrophages following exposure to chitosan-DNA nanoparticles. Biomaterials 2005;26:961–970.
19. Madry H, Cucchiarini M, Stein U, Remberger K, Menger MD, Kohn D, Trippel SB. Sustained transgene expression in cartilage defects in vivo after transplantation of articular chondrocytes modified by lipid-mediated gene transfer in a gel suspension delivery system. J Gene Med 2003;5:502–509.
20. Stove J, Fiedler J, Huch K, Gunther KP, Puhl W, Brenner R. Lipofection of rabbit chondrocytes and long lasting expression of a lacZ reporter system in alginate beads. Osteoarthritis Cartilage 2002;10:212–217.
21. Goomer RS, Deftos LJ, Terkeltaub R, Maris T, Lee MC, Harwood FL, Amiel D. High-efficiency non-viral transfection of primary chondrocytes and perichondrial cells for ex-vivo gene therapy to repair articular cartilage defects. Osteoarthritis Cartilage 2001;9:248–256.
22. Madry H, Kaul G, Cucchiarini M, Stein U, Zurakowski D, Remberger K, Menger MD, Kohn D, Trippel SB. Enhanced repair of articular cartilage defects in vivo by transplanted chondrocytes overexpressing insulin-like growth factor I (IGF-I). Gene Ther 2005;12:1171–1179.
23. Masuda K, Pfister BE, Sah RL, Thonar EJ. Osteogenic protein-1 promotes the formation of tissue-engineered cartilage using the alginate-recovered-chondrocyte method. Osteoarthritis Cartilage 2006;14:384–391.
24. Loeser RF, Pacione CA, Chubinskaya S. The combination of insulin-like growth factor 1 and osteogenic protein 1 promotes increased survival of and matrix synthesis by normal and osteoarthritic human articular chondrocytes. Arthritis Rheum 2003;48:2188–2196.
25. Nishida Y, Knudson CB, Eger W, Kuettner KE, Knudson W. Osteogenic protein 1 stimulates cells-associated matrix assembly by normal human articular chondrocytes: Up-regulation of hyaluronan synthase, CD44, and aggrecan. Arthritis Rheum 2000;43:206–214.
26. Klein-Nulend J, Louwerse RT, Heyligers IC, Wuisman PI, Semeins CM, Goei SW, Burger EH. Osteogenic protein (OP-1, BMP-7) stimuates cartilage differentiation of human and goat perichondrium tissue *in vitro*. J Biomed Mater Res 1998;40: 614–620.
27. Flechtenmacher J, Huch K, Thonar EJ, Mollenhauer JA, Davies SR, Schmid TM, Puhl W, Sampath TK, Aydelotte MB, Kuettner KE. Recombinant human osteogenic protein 1 is a potent stimulator of the synthesis of cartilage proteoglycans and collagens by human articular chondrocytes. Arthritis Rheum 1996;39:1896–1904.
28. Chen P, Vukicevic S, Sampath TK, Luyten FP. Osteogenic protein-1 promotes growth and maturation of chick sternal chondrocytes in serum-free cultures. J Cell Sci 1995;108(Part 1):105–114.
29. Louwerse RT, Heyligers IC, Klein-Nulend J, Sugihara S, van Kampen GP, Semeins CM, Goei SW, de Koning MH, Wuisman PI, Burger EH. Use of recombinant human osteogenic protein-1 for the repair of subchondral defects in articular cartilage in goats. J Biomed Mater Res 2000;49:506–516.
30. Grgic M, Jelic M, Basic V, Basic N, Pecina M, Vukicevic S. Regeneration of articular cartilage defects in rabbits by osteogenic protein-1 (bone morphogenetic protein-7). Acta Med Croatica 1997;51:23–27.
31. Jelic M, Pecina M, Haspl M, Kos J, Taylor K, Maticic D, McCartney J, Yin S, Rueger D, Vukicevic S. Regeneration of articular cartilage chondral defects by osteogenic protein-1 (bone morphogenetic protein-7) in sheep. Growth Factors 2001;19:101–113.
32. Hidaka C, Quitoriano M, Warren RF, Crystal RG. Enhanced matrix synthesis and in vitro formation of cartilage-like tissue by genetically modified chondrocytes expressing BMP-7. J Orthop Res 2001;19:751–758.
33. Hidaka C, Goodrich LR, Chen CT, Warren RF, Crystal RG, Nixon AJ. Acceleration of cartilage repair by genetically modified chondrocytes over expressing bone morphogenetic protein-7. J Orthop Res 2003;21:573–583.
34. Li JZ, Li H, Sasaki T, Holman D, Beres B, Dumont RJ, Pittman DD, Hankins GR, Helm GA. Osteogenic potential of five different recombinant human bone morphogenetic protein adenoviral vectors in the rat. Gene Ther 2003;10:1735–1743.
35. Breitbart AS, Grande DA, Mason JM, Barcia M, James T, Grant RT. Gene-enhanced tissue engineering: Applications for bone healing using cultured periosteal cells transduced

retrovirally with the BMP-7 gene. Ann Plast Surg 1999;42: 488–495.
36. Yang M, Ma QJ, Dang GT, Ma KT, Chen P, Zhou CY. Adeno-associated virus-mediated bone morphogenetic protein-7 gene transfer induces C2C12 cell differentiation into osteoblast lineage cells. Acta Pharmacol Sin 2005;26:963–968.
37. Duan D, Du J, Wang H, Liu Y, Guo X. Expression of rhBMP-7 gene in transduced bone marrow derived stromal cells. Chin Med Sci J 2002;17:157–159.
38. Yeh LC, Lee JC. Co-transfection with the osteogenic protein (OP)-1 gene and the insulin-like growth factor (IGF)-I gene enhanced osteoblastic cell differentiation. Biochim Biophys Acta 2006;1763:57–63.
39. Zhao X, Yu SB, Wu FL, Mao ZB, Yu CL. Transfection of primary chondrocytes using chitosan-pEGFP nanoparticles. J Control Release 2006;112:223–228.
40. Mao HQ, Roy K, Troung-Le VL, Janes KA, Lin KY, Wang Y, August JT, Leong KW. Chitosan-DNA nanoparticles as gene carriers: Synthesis, characterization and transfection efficiency. J Control Release 2001;70:399–421.
41. Corsi K, Chellat F, Yahia L, Fernandes JC. Mesenchymal stem cells, MG63 and HEK293 transfection using chitosan-DNA nanoparticles. Biomaterials 2003;24:1255–1264.
42. Jakob M, Demarteau O, Schafer D, Hintermann B, Dick W, Heberer M, Martin I. Specific growth factors during the expansion and redifferentiation of adult human articular chondrocytes enhance chondrogenesis and cartilaginous tissue formation in vitro. J Cell Biochem 2001;81: 368–377.
43. Sun CJ, Pan SP, Xie QX, Xiao LJ. Preparation of chitosan-plasmid DNA nanoparticles encoding zona pellucida glycoprotein-3alpha and its expression in mouse. Mol Reprod Dev 2004;68:182–188.
44. Li XW, Lee DK, Chan AS, Alpar HO. Sustained expression in mammalian cells with DNA complexed with chitosan nanoparticles. Biochim Biophys Acta 2003;1630: 7–18.
45. Kiang T, Wen J, Lim HW, Leong KW. The effect of the degree of chitosan deacetylation on the efficiency of gene transfection. Biomaterials 2004;25:5293–5301.

Available online at www.sciencedirect.com
ScienceDirect
Acta Biomaterialia 5 (2009) 2371–2384
Acta BIOMATERIALIA
www.elsevier.com/locate/actabiomat

Development of hyaluronic acid-based scaffolds for brain tissue engineering

Tzu-Wei Wang [1], Myron Spector *

Tissue Engineering Laboratories, VA Boston Healthcare System, Mail Stop: 151 Research, 150 S. Huntington Ave., Boston, MA 02130, USA
Department of Orthopaedic Surgery, Brigham and Women's Hospital, Harvard Medical School, Boston, MA 02115, USA

Received 7 November 2008; received in revised form 10 February 2009; accepted 24 March 2009
Available online 1 April 2009

Abstract

Three-dimensional biodegradable porous scaffolds play vital roles in tissue engineering. In this study, a hyaluronic acid–collagen (HA–Coll) sponge with an open porous structure and mechanical behavior comparable to brain tissue was developed. HA–Coll scaffolds with different mixing ratios were prepared by a freeze–drying technique and crosslinked with water-soluble carbodiimide to improve mechanical stability. The pore structure of the samples was evaluated by light and scanning electron microscopy, and the mechanical behavior was analyzed by mechanical compression and tension testing. The degree of crosslinking was determined by the water absorption and trinitrobenzene sulfonic assay, and the HA content was determined by a carbazole assay. The results showed that HA–Coll scaffolds containing an open porous structure with a homogeneous pore size distribution could be fabricated. Certain features of the mechanical properties of HA–Coll scaffolds prepared with a Coll:HA mixing ratio of 1:2, and pure HA sponges, were comparable with brain tissue. Neural stem cells (NSCs) were expanded in number in monolayer culture and then seeded onto the three-dimensional scaffolds in order to investigate the effects of the different types of scaffolds on neurogenic induction of the cells. This study contributes to the understanding of the effects of HA content and crosslink treatment on pore characteristics, and mechanical behavior essential for the design of HA–Coll scaffolds suitable for NSC growth and differentiation for brain tissue engineering.

Keywords: Scaffold; Collagen; Hyaluronic acid; Mechanical properties; Neural stem cell

1. Introduction

One strategy in the formulation of tissue engineering scaffolds is to fabricate analogs of extracellular matrix using collagen (Coll), gelatin, and sulfated and non-sulfated glycosaminoglycans (GAGs) [1,2]. These biocompatible and biodegradable materials are especially favored as scaffolds for the delivery of cultured cells or for three-dimensional (3-D) tissue reconstruction [3,4]. The cells, stimulated by appropriate scaffolds, can remodel the scaffolds and replace them with newly synthesized extracellular matrix [4,5]. It has been well established that the specific interaction of cells with their surrounding extracellular matrix is responsible for promoting and regulating these regeneration processes not only to support tissue ingrowth but also to attract and guide the activity of cells [6].

Coll and hyaluronic acid (HA) are widely used natural polymers for the development of implantable matrices. Type I collagen, a major structural protein of extracellular matrix, supports the growth of a wide variety of tissues, while its structure imparts favorable properties such as mechanical strength [7]. HA (also referred to as hyaluronan), a high molecular weight GAG polymer composed of repeating units of D-glucuronic acid and *n*-acetyl-D-glucosamine, is a ubiquitous biopolymer in the mammalian body and one of the principal components of brain extra-

* Corresponding author. Address: Tissue Engineering Laboratories, VA Boston Healthcare System, Mail Stop: 151 Research, 150 S. Huntington Ave., Boston, MA 02130, USA. Tel.: +1 857 364 6639; fax: +1 857 364 6791.
E-mail address: mspector@rics.bwh.harvard.edu (M. Spector).
[1] Current address: Department of Materials Science and Engineering, National Tsing Hua University, Hsinchu, Taiwan.

1742-7061/$ - see front matter © 2009 Acta Materialia Inc. Published by Elsevier Ltd. All rights reserved.
doi:10.1016/j.actbio.2009.03.033

cellular matrix [8,9]. The favorable attributes of HA have led to the preparation of HA hydrogel biomaterials [10–12], and the combination of HA and Coll as a tissue engineering scaffold [13–15].

A variety of functions have been ascribed to HA, including maintenance of the overall conformation of matrix surrounding cells and the creation of cell-free spaces upon hydration [16]. HA can also activate cell surface receptors that influence intracellular signaling cascades affecting cell behaviors such as growth, migration and differentiation [17]. In the nervous system, HA functions in conjunction with a number of HA-binding proteoglycans as well as with collagen [8]. HA and these hyalectans have been implicated in regulating glial cell and neuron migration, neurite outgrowth and axon pathfinding [18,19].

The objective of this study was to prepare crosslinked HA-type I Coll and HA-type II Coll sponge-like scaffolds using the following mixing ratios and to investigate their physical, chemical, mechanical and morphological characteristics: pure HA, Coll:HA = 2:1 (33% HA), Coll:HA = 1:1 (50% HA), Coll:HA = 1:2 (67% HA) and pure Coll. The ultimate goal of this study is to develop a suitable scaffold as a potential neural stem cell-seeded construct for implantation into a defect in the brain resulting from trauma (e.g. penetrating projectile) or tumor resection. Therefore an additional objective was to study the neurogenic differentiation of neural stem cells (NSCs) seeded into the scaffolds. The reason for the comparative investigation of types I and II collagens for this application is that differences in the properties of the Coll types may affect their association with HA in the composite, thus resulting in scaffolds with different characteristics.

2. Materials and methods

2.1. Materials

Medical-grade types I and II collagens from Geistlich Pharma AG (Wolhusen, Switzerland), and non-sterile sodium hyaluronate (mol. wt. 1.39×10^6 Da) from Genzyme Corp. (Cambridge, MA) were used in the scaffold preparation. The reason we use this molecular weight is that this range is very close to that found in the ECM of brain tissue [20]. We did not choose a low molecular weight due to the associated poor mechanical properties and the difficulty in forming an intact porous structure when culturing with cells for a defined period of time. These low molecular weight scaffolds would become dissociated and most of the HA would be rapidly eluted into the medium. We will try a higher molecular weight HA ($>3 \times 10^6$ Da) in the future since it is proposed that high molecular weight HA can inhibit astrocyte proliferation in vitro and promotes astrocyte quiescence in vivo [21], which would be beneficial when implanting the matrices into brain lesion site for nervous tissue regeneration. JB-4 A monomer solution (Cat. # 0226A-800), JB-4 A catalyst (Benzoyl Peroxide, plasticized, Cat. # 02618-12) and JB-4 B embedding solution (Cat. # 0226B-30) were obtained from Polysciences (Warrington, PA). Aniline blue (Cat. # A-967), glacial acetic acid (Cat. # A A507-500), NaCl (S642, lot # 028434), and ethanol (lot # 100098) were obtained from Fisher Scientific (Pittsburgh, PA). Cytoseal 60 for coverslipping was obtained from Electron Microscopy Sciences (Hatfield, PA; Cat. # 18006). Hydrochloric acid (HCl; 435570, batch # 00659BH), sodium tetraborohydrate (59640, batch # 074K0211), sulfuric acid (320501, batch # 07666PH), growth factors for cell culture, and proteinase-K (P6556, batch # 036K8604) were obtained from Sigma–Aldrich (St. Louis, MO). 1-Ethyl-3-[3-dimethylaminopropyl] carbodiimide hydrochloride (EDAC; E7750, batch # 03K0753), sodium bicarbonate (S5761, batch # 047K0072), carbazole (C5132, batch # 084K0125) and lysine (L5501, batch # 106K2511) were obtained from Sigma. *N*-Hydroxyl succinimide (NHS; 130672, batch # 0672042) was obtained from Aldrich (St. Louis, MO). 2,4,6-Trinitrobenzene sulfonic acid (TNBS) (28997, lot # JB121704) was obtained from Thermo Scientific (Rockford, IL).

2.2. Fabrication of porous 3-D scaffolds

Slurries were prepared containing 1 wt.% type I collagen (Coll I), type II collagen (Coll II) or HA. In brief, Coll I and Coll II were dissolved in hydrochloric acid at pH 3; HA was dissolved in distilled water. Slurries were blended at 15,000 rpm for 2 h (in the cold) to form uniform slurries and break apart larger collagen fragments. After blending, the slurries were centrifuged at 1000 relative centrifugal force (RCF) for 3 min at 4 °C to remove trapped air bubbles. Types I and II Coll and HA slurries were mixed together in order to prepare for fabrication of composite scaffolds. The experiments were divided into the groups with different Coll:HA mixing ratios. For each slurry, approximately 20 ml was poured into a 2.8×0.8 cm metal mold. The molds were then placed into a freeze-dryer being ramped to −40 °C over a 60 min period [22]. The slurry was held at −40 °C for approximately 3 h in order to allow ice crystals to nucleate and anneal. At this time a vacuum was created within the chamber. When the vacuum pressure reached 700 mTorr, the temperature was raised to 0 °C and the sample was left 18 h to allow the ice to sublimate.

A water-soluble carbodiimide was used to chemically crosslink the fabricated porous scaffolds. Discs, 8 mm in diameter, were punched from the 2-mm-thick scaffold sheets using a dermal biopsy punch (Milex, Inc., York, PA). The crosslinking reaction was carried out using EDAC and NHS at a 5:2 molar ratio in 80% ethanol. These reagents form amide bonds between carboxyl groups and amino groups as well as ester bonds between hydroxyl and carboxyl groups, resulting in Coll–Coll crosslinking, and HA–Coll, or HA–HA crosslinking [23–25]. The crosslinking was carried out on a rotator for 4 h at room temperature to ensure infiltration of the crosslinking solution into the scaffold discs. The crosslink protocol was based on our prior work, which showed that the crosslink period should be longer than 2 h [13], and other work, which

showed that an 80% ethanol solution was substantially more effective for EDAC crosslinking of HA than a 95% solution [25], as we previously used [13].

After crosslinking, a disodium hydrogen phosphate solution was used to block the residual EDAC, and the scaffolds were rinsed in distilled water to hydrolyze urea derivatives. The scaffolds were then lyophilized at −40 °C and 300 mTorr overnight.

2.3. Pore size and porosity analysis of scaffolds

For analysis of pore size and porosity, six scaffolds from each group were embedded in a plastic resin, JB-4. The scaffolds were first dehydrated though three 10-min soaks in 100% ethanol. The samples were then equilibrated at 4 °C in a rotator for approximately 18 h in a solution of 50% ethanol and 50% catalyzed JB-4 solution. The catalyzed solution consisted of 0.625 g of JB-4 A catalyst (Benzoyl Peroxide, plasticized) in 50 ml JB-4 A monomer solution. Following equilibration, the scaffolds were soaked in 100% catalyzed JB-4 solution at 4 °C in a rotator for 2 days. The solution was changed every 24 h. After 2 days in 100% catalyzed solution, the samples were ready for embedding. Embedding solution was prepared at a ratio of 25:1 of JB-4 catalyzed solution:JB-4 solution B. Plastic block holders were placed into each well and the molds were placed in 4 °C storage overnight to allow the samples to harden. The blocks were then removed from the mold and allowed to dry at room temperature overnight.

A 4- to 6-μm thick section was cut from each scaffold using a microtome and stained with analine blue to analyze the pore size and porosity of the scaffolds. The aniline blue solution was prepared with 2.5 g of aniline blue, 2 ml of glacial acetic acid and 100 ml of distilled water, then filtered. Sections were cut and placed in a water bath with a few drops of ammonium hydroxide. The sections were then mounted on glass slides and allowed to dry overnight before staining. To stain, the slides were dipped in aniline blue solution for 2 min, then placed in 1% acetic acid solution for 1 min. They were then dipped in 95% alcohol 5–10 times, followed by 5–10 dips in 100% alcohol in order to remove background staining. The slides were coverslipped using cytoseal. Digital Scion Image software (PC version of NIH image, Scion Corporation, Frederick, MD) was used to analyze average pore size for each stained sample. The average pore size was calculated by measuring the size of 30 pores from data obtained from 10 locations from a total of thee samples. The percentage porosity was calculated from six locations from a total of three samples.

2.4. Sponge morphology examination by scanning electron microscopy

Using field-emission scanning electron microscopy (JEOL-5910), crosslinked collagen, HA–Coll and HA sponges were analyzed to examine the morphology and porous structure of the scaffolds. Specimens were dehydrated though a graded series of ethanol solutions, mounted on stubs, and sputter-coated with an ultrathin layer of gold (BioRad, Hercules, CA). The average diameter of the pores was analyzed in an arbitrary zone using a computerized image analyzer.

2.5. Water absorption and apparent density

Six discs of each crosslinked dry sponge (8 mm in diameter) group were weighed and immersed in phosphate-buffered saline (PBS; pH 7.4) at room temperature for 2 h. After removal from saline solution, the excess water was wiped and the samples weighed (wet weight). The samples were then freeze-dried overnight. The dried samples were removed and their masses were recorded. The water uptake ability was then calculated from the following equation:

$$\text{Water absorption} = [(W_w - W_d)/W_d]$$

where W_d is the weight of the dry sponge and W_w is the weight of the wet sponge.

The apparent density of the scaffolds was calculated by dividing the dry weight by the volume of the samples. For comparative purposes, values for the weight of hydrated brain divided by volume were recorded for six cortical rat brain samples from three rats.

2.6. Crosslinking degree determination by trinitrobenzene sulfonic acid assay

A previously reported assay was used to determine the number of non-crosslinked ε-amino groups in the crosslinked HA–Coll scaffolds [26]. In brief, for each group, four scaffolds were chosen at random and each was placed in a solution containing 1 ml of 4% $NaHCO_3$ and 1 ml of 0.5% 2,4,6-trinitrobenzene sulfonic acid. The solutions were heated at 37 °C for 4 h. Thee milliliters of 6 N HCl was added and the solutions were vortexed, then placed in a 65 °C water bath until the entire scaffold was broken down. Five milliliters of distilled water was added to the solution and absorbance was measured at 345 nm. Lysine was used to create a standard curve. Results were obtained by converting absorbance value to moles of ε-amino groups per gram of scaffold by the equation:

$$\frac{\text{moles } \varepsilon\text{-amino groups}}{g \text{ scaffold}} = \frac{2(\text{Absorbance})(0.01\text{L})}{(1.46\times10^4\ \text{L/mole cm})(1\,\text{cm})(10\,\text{mg})}$$

where 1.46×10^4 L/mole cm is the molecular absorptivity of TNBS-labeled lysine, 1 cm is the cell path length and 10 mg is the sample weight. The degree of crosslinking could be obtained from the difference between the absorbance values before and after crosslinking. The equation is as follows:

$$\text{Crosslinking degree } (\%) = \left(1 - \frac{\text{Absorbance of crosslinked sponge}}{\text{Absorbance of non-crosslinked sponge}}\right) \times 100$$

2.7. Hyaluronic acid quantification by carbazole assay

The protocol used was modified from Bitter and Muir [27]. Sodium tetraborahydrate (191 mg) was dissolved in 20 ml of sulfuric acid to make a 0.955 wt.% solution. A carbazole solution of 0.125 wt.% was made by adding 0.0125 g of carbazole to 9.9875 g of ethanol. Three milliliters of sodium tetraborahydrate solution was placed in test tubes and cooled to 4 °C. While in the chamber, 0.5 ml of the HA solution was added to each test tube. The tubes were shaken first gently, then vigorously. The tubes were then heated in boiling water for 10 min and then cooled to room temperature. Carbazole solution (0.1 ml) was then added to each solution with shaking. The carbazole interacts with glucuronic acid to form a complex that can be detected with a spectrophotometer. The tubes were heated again in boiling water for 15 min and then cooled to room temperature. Aliquots of 150 μl of each solution were added to a 96-well plate and absorption was measured at 530 nm on the WALLAC VICTOR© microplate reader (PerkinElmer, Waltham, MA). The standard curve was plotted and used to identify HA concentrations in each scaffold.

2.8. In vitro release of HA from the scaffolds

In order to compare the release profiles of the crosslinked scaffolds with varying amounts of HA, the samples were immersed in PBS for 28 days. Samples of the solution were taken at 1, 3, 7, 14, 21 and 28 days. The cumulative release of HA for each time point was calculated and normalized by the total amount of HA incorporated within the HA–Coll scaffolds. At the end of the 28 day period the samples that could still be handled were recovered and weighed.

2.9. Mechanical property characterization

Unidirectional, unconfined compression ($n = 6$) and tension ($n = 6$) tests were performed on hydrated scaffold samples at a constant strain rate of 0.1% strain s^{-1}. All compression tests were performed perpendicular to the plane of scaffold using 8-mm-diameter cylindrical samples (2 mm thick). In brief, scaffolds were hydrated in PBS before testing. Compression tests were performed using a custom-fabricated mechanical testing device. A 0.25 N tension–compression load cell (Transducer Techniques, Temecula, CA) was attached to the motor platform of a nanoindenter (MicroMaterials LLC, Wrexham, UK). Mechanical tests on hydrated scaffolds were performed at the constant strain rate to a maximum strain of 75% using a 20 N load cell sampling at a frequency of 2 Hz on a Zwick/Poell Z2.5 static materials tester (Zwick GmbH & Co., Ulm, Germany) with integrated testing software (testXpert, Zwick). A flat-faced plunger, the diameter of which was larger than the 8 mm diameter of the samples, was employed for the compression testing. Values for the compressive yield strength and modulus of elasticity were recorded at a strain of 5%.

Pure collagen, pure HA, and one of the HA–Coll composite scaffold groups (Coll:HA = 1:2) were allocated for tension testing. Rectangular scaffold samples (width, 10 mm; length, 30 mm; thickness, 2 mm) were cut using a razor blade. Tension tests were performed using the Zwick/Roell (20 N load cell) sampling at 10 Hz, on samples held vertically using custom clamps. The peak strength and modulus of elasticity at 5% strain were determined.

For compression testing of brain tissue as a comparative control, the cortical tissues of six hemispheres from three rats were trimmed with a biopsy punch or razor blade in the shape comparable to our scaffold specimens. In the compression test ($n = 6$), the samples were of cylindrical shape (8 mm in diameter and 2 mm in thickness), while in tension test ($n = 6$) the specimens were of rectangular shape (30 mm in length, 10 mm in width, 2 mm in thickness).

2.10. Isolation and culture of NSCs in 2-D and in 3-D cultures

Seven young rats (<6 weeks old) were sacrificed with CO_2 and sterilized with 70% isopropyl alcohol solution. The animals were decapitated using a large scissors and the heads sterilized with betadine solution. The skull was opened by a drill to expose the brain, which was removed using a small curved spatula and washed with PBS. Two coronal slices of brain tissue (2 mm thick) just behind the olfactory bulb and the subventricular zone lining the lateral ventricles were cut and isolated. Tissues were minced into small pieces with a scalpel blade, centrifuged and resuspended in the papain at 37 °C for 40 min digestion. The small pieces of brain tissue were centrifuged again to remove supernatant. Three milliliters of ovomucoid solution was added and triturated by fire-polished Pasteur pipettes to homogenize the cell suspension. Finally, cells were resuspended in neurobasal medium with essential supplements and cultured until desired cell densities were achieved. The cells from the seven animals were cultured separately in T-75 flasks until 80% confluence.

In order to investigate the effects of the scaffold type on the support of the NSCs and their subsequent differentiation, NSCs were inoculated on the different types of scaffolds: pure Coll, HA–Coll (Coll:HA = 1:2) and pure HA sponges. The Coll:HA = 1:2 scaffold was selected for cell seeding on the basis of its mechanical behavior which was substantially different from the collagen scaffold. In brief, the neurospheres that formed in the T-75 dishes and the dissociated cells (5×10^5 cells cm^{-2}) were collected and seeded into the scaffolds in induction medium for neuronal maturation: neurobasal medium, supplemented with 2% B27, 1% penicillin/streptomycin/L-glutamine, isobutylmethylxanothine (0.1 mM) heparin (0.5 USP units ml^{-1}), basic fibroblast growth factor (20 ng ml^{-1}) and epidermal growth factor (20 ng ml^{-1}). For further differentiation, retinoic acid (20 μM) and brain-derived neurotrophic factor (50 ng ml^{-1}) were added after 2 days.

For cell seeding onto the 3-D scaffolds, the dry matrix specimens were rinsed with PBS and then incubated in culture medium for 2 h for pre-wetting, followed by air-drying to favor cell attachment. A 100 μl suspension containing 2.5×10^5 passage 2–3 cells and neurospheres was pipetted onto each 8-mm-diameter scaffold ($n = 7$) in agarose-coated wells. After 30 min, medium was added to the cultures to total 0.5 ml. The medium was changed every other day, and cultures were terminated after 2 weeks.

2.11. Immunohistochemistry

The specimens were fixed in 4% paraformaldehyde, and paraffin embedded. After deparaffinization, sections at 4–6 μm thickness were used for immunohistochemistry analysis. In brief, specimens were rehydrated with cold PBS and blocked for 30 min in blocking solution to reduce the non-specific binding. Specimens were then incubated with primary antibodies overnight at 4 °C, washed, and incubated in secondary antibodies for 1 h at room temperature. 4′,6-Diamidino-2-phenylindole (DAPI) was used for nucleus staining. The following primary antibodies were applied for the investigation of neuronal induction: mouse monoclonal anti-Nestin (1:200 dilution; Chemicon); anti-neuronal nuclei (NeuN; 1:200; Chemicon); rabbit monoclonal anti-tubulin β III (Tuj-1; 1:100; Chemicon); and polyclonal anti-major microtubule associated protein (MAP2; 1:500; Chemicon). The following secondary antibodies were applied for conjugation and visualization under fluorescence microscopy: polyclonal donkey anti-mouse IgG-TRITC antibody (Jackson ImmunoResearch Laboratories, West grove, PA) and polyclonal donkey anti-rabbit IgG-FITC antibody (Jackson ImmunoResearch Laboratories, USA). Negative controls were incubated with mouse IgG (Invitrogen) diluted to the same protein concentration instead of the primary antibody.

2.12. Statistical analysis

Results are presented as mean ± standard error of the mean unless otherwise noted. One-, two- and three-way analyses of variance (ANOVA) were used to determine the significance of the effect of select variables on the certain properties of the scaffolds. Post hoc testing was performed using Fisher's protected least squares differences (PLSD) to test the significance of selected group comparisons. Paired *t*-tests were performed to compare individual sets of data. A probability value of 95% ($p < 0.05$) was used to determine significance.

3. Results

3.1. Morphological characterization: pore size and porosity analysis

The interconnecting pore morphology was revealed by scanning electron microscopy (SEM; Fig. 1). The walls of the scaffold displayed a sheet-like appearance in SEM. In some views at higher magnification, fiber-like features were seen in the sheets (Fig. 1B). The pure type I (Fig. 1A) and type II (Fig. 1B) Coll scaffolds were similar in appearance. In comparison to the Coll scaffolds, the sheet-like walls of the pure HA samples were perforated by holes (Fig. 1E). On closer inspection, similar perforation of the sheet-like walls was seen in the Coll samples to which HA was added (Fig. 1B and D). Under the same 1 wt.% concentration of the starting slurry, the structure of the pure HA scaffold was seen to be more compact and denser, when viewed at lower magnification (Fig. 1F) compared to the Coll scaffolds.

Light microscopic examination of sections of the scaffolds (Fig. 2) reflected some of the features observed by SEM. The honeycomb-like structure of the scaffolds was clearly evident. Qualitatively, the type I (Fig. 2A) and type II (Fig. 2E) Coll scaffolds had similar foam morphologies and comparable pore diameters. Increasing the HA content resulted in a noticeable increase in the pore diameter for both the types I and II samples (comparing Fig. 2A–D with Fig. 2E and F). The increase in the HA content of the types I and II Coll samples also appeared to be accompanied by an increase in the number of perforations in the walls of the scaffold, as seen by SEM. The pure HA scaffold (Fig. 2I) had a pore architecture comparable to the type I (Fig. 2A) and type II (Fig. 2E) Coll scaffolds. However, the walls of the HA samples were less uniform in thickness than those of the Coll samples. The extracellular matrix of the brain tissue samples displayed a smaller pore diameter than the biomaterial scaffolds. None of the samples, including the brain samples, demonstrated a noticeable orientation of the pores.

Quantitatively, the type II Coll scaffolds had a slightly larger pore diameter (by about 10%) than the type I samples (Fig. 3A). The pore diameter increased with increasing HA content (Fig. 3A). The samples prepared with a Coll:HA ratio of 1:2 (i.e. with 67% HA) had pore diameters which were about 90% larger than those in the corresponding pure Coll samples. The pore diameter of the HA scaffold was comparable to the type II Coll specimen, and the brain tissue displayed a pore diameter comparable with the type I Coll scaffold (Fig. 3A).

The percentage porosity of the samples, which ranged from 75% to 91%, increased (Table 1) and the apparent densities decreased (Table 1) with increasing HA content. The percentage porosity of the pure Coll and HA scaffolds, and the brain tissue were comparable (Table 1).

Two-way ANOVA of the data from the HA–Coll samples demonstrated statistically significant effects of collagen type (I vs. II; $p = 0.01$; power = 0.73) and the percentage of HA ($p < 0.0001$; power = 1) on the pore diameter. Fisher's PLSD post hoc testing showed that all group comparisons were statistically significant. Two-way ANOVA of the data from the HA–Coll samples demonstrated a statistically significant effect of the percentage of HA in the collagen scaffolds on the percent porosity ($p < 0.0001$; power = 1), but

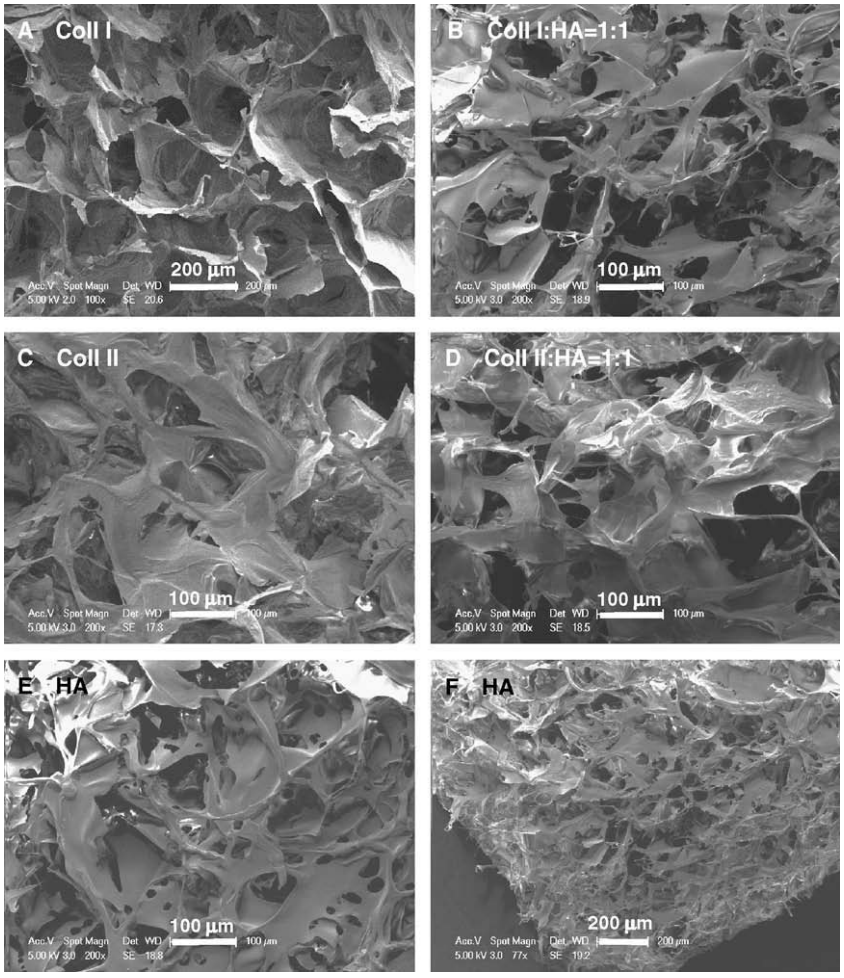

Fig. 1. Scanning electron micrographs of the scaffolds: (A) type I Coll; (B) type I Coll:HA = 1:1; (C) type II Coll; (D) type II Coll:HA = 1:1; (E and F) HA; (F) the appearance structure of the HA–collagen scaffold with lower magnification. Type I collagen, I; hyaluronan, HA; type II collagen, II; type I collagen mixed with hyaluronan in the ratio of 1–1, I_HA = 1:1.

no effect of collagen type ($p = 0.46$; power = 0.1). Fisher's PLSD post hoc testing showed that all group comparisons among samples with different HA contents were statistically significant.

3.2. Degree of crosslinking

Very few ε-amino groups were detected in the pure HA scaffolds before crosslinking (<0.1 mol g^{-1}). The analysis of the various groups of collagen scaffolds indicated a decrease in the number of ε-amino groups with increasing HA content in the non-crosslinked samples, as would be expected because the collagen was the source of the ε-amino groups. The dramatic reduction in the number of ε-amino groups after crosslinking (Fig. 3B) reflected the degree of crosslinking. From this measurement, the degree of crosslinking gradually decreased with the increasing amount of HA, from nearly 90% down to around 50% (Table 1). While the results for the types I and II Coll scaffolds appeared comparable, three-way ANOVA revealed statistically significant effects of collagen type ($p = 0.001$; power = 0.95), as well as of HA content ($p < 0.0001$; power = 1) and crosslinking ($p < 0.0001$; power = 1), on the number of ε-amino groups. Fisher's PLSD post hoc testing demonstrated statistically significant differences in all group comparisons.

3.3. Water absorption

The addition of HA to the collagen scaffolds increased the water uptake capability, because of the hygroscopic nature of HA (Table 1). All the sponges absorbed the water within 30 s and were saturated within 5 min. The pure HA scaffolds displayed a 60-fold increase in weight as a result of water uptake, which was about 50% higher than the HA–Coll samples (Table 1). While there did not appear to be notable effects of collagen type on the water uptake, two-way ANOVA demonstrated the significant effects of collagen type ($p = 0.004$; power = 0.86) as well as HA content ($p < 0.0001$; power = 1) on water absorption. Fisher's

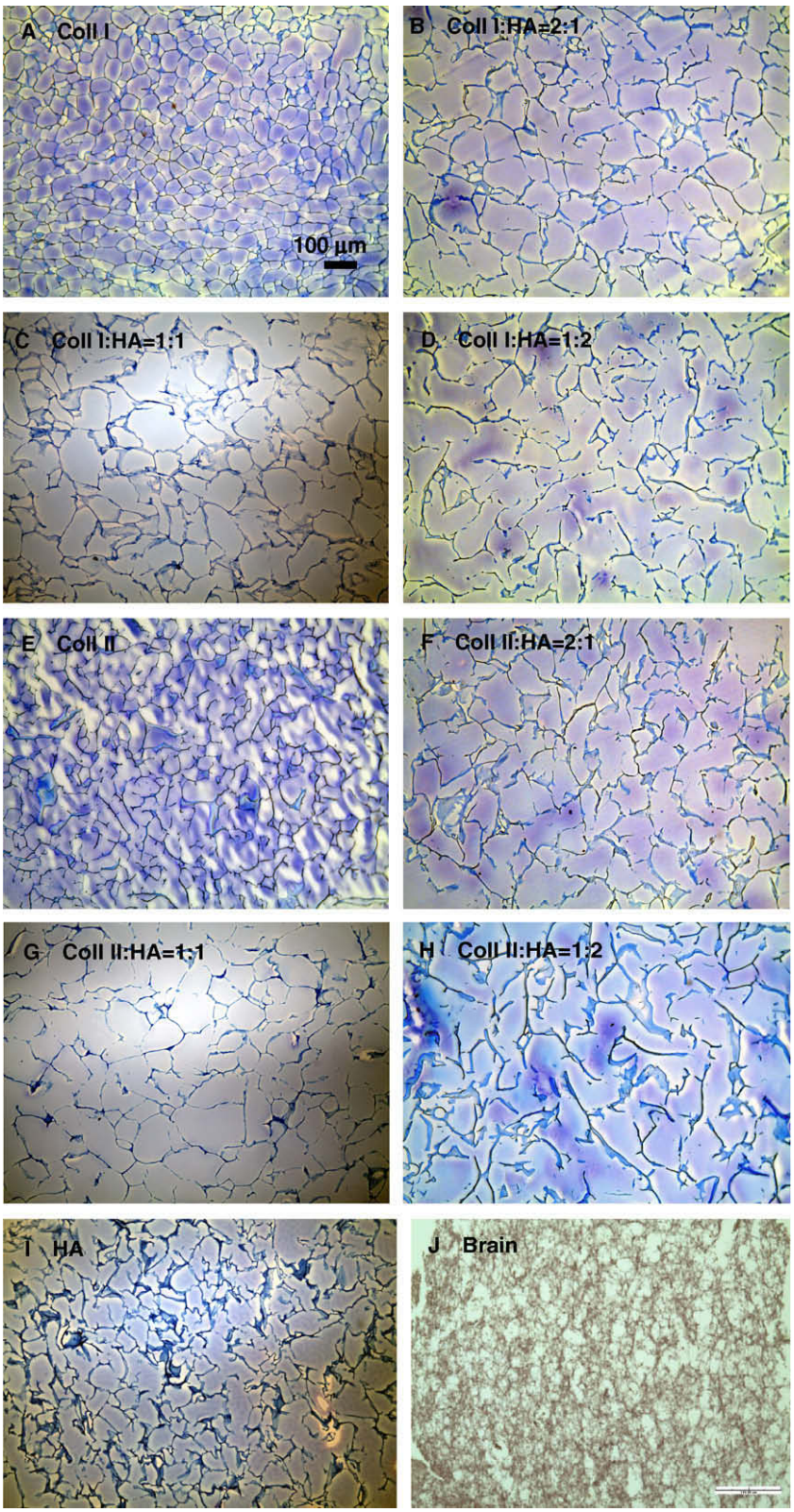

Fig. 2. Light micrographs of sections of the scaffolds with various collagen:HA mixing ratios: (A) type I Coll; (B) type I Coll:HA = 2:1; (C) type I Coll:HA = 1:1; (D) type I Coll:HA = 1:2; (E) type II Coll; (F) type II Coll:HA = 2:1; (G) type II Coll:HA = 1:1; (H) type II Coll:HA = 1:2; (I) HA; (J) brain tissue extracellular matrix. All images were taken at the same magnification (see A).

PLSD post hoc testing revealed statistical significance for all group comparisons.

There were strong inverse linear relationships between the water absorption with the degree of crosslinking for

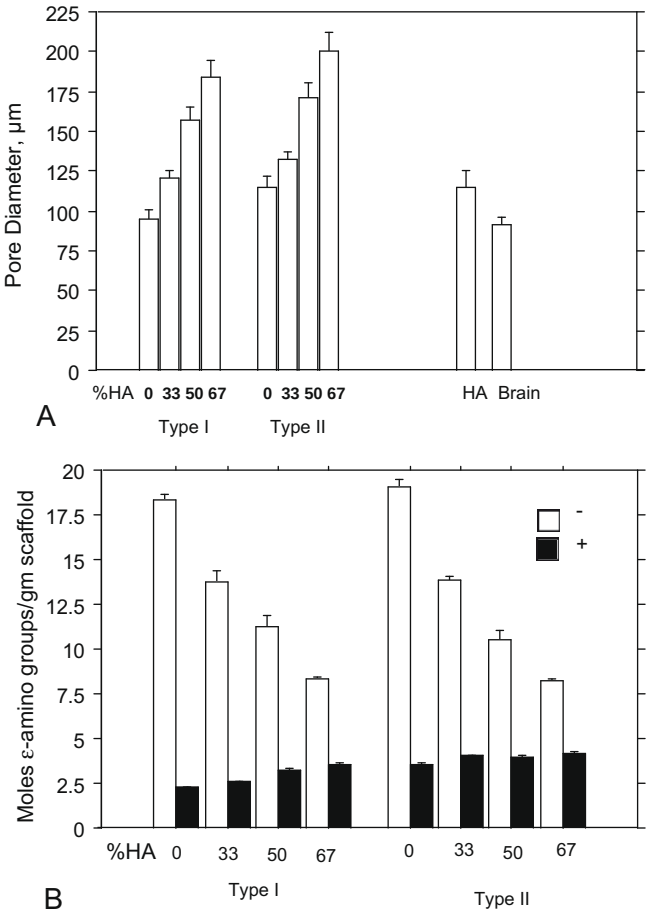

Fig. 3. Graphs showing the effects of collagen type and HA content on: (A) mean pore diameter ($n = 6$); and (B) number of ε-amino groups before (−) and after (+) crosslinking ($n = 4$). Mean ± standard error of the mean.

the types I and II HA–Coll scaffolds: $R^2 = 0.95$ and $R^2 = 0.89$, respectively by linear regression analysis. This was reasonable because in the crosslinking process the hydrophilic functional groups were consumed to react with carbodiimide crosslinking agent.

3.4. In vitro HA release degradation test

The non-crosslinked HA-containing scaffolds were not sufficiently stable to undergo the HA release testing; they disintegrated in the aqueous solution. The HA release from the scaffolds varied among crosslinked scaffolds prepared with different HA:Coll ratios (Fig. 4). In general, three regions of release were observed: an initial burst release in the first few days, followed by a linear region of release for a defined period of time, and finally a second region of linear release for the rest of the time. From the results, crosslinked pure HA scaffolds were not totally degraded until the end of the test period (28 days), while the non-crosslinked HA scaffolds immediately dissolved in PBS. When crosslinked with collagen, most of the HA in the composite HA–collagen scaffolds remained stable without hydrolysis or elution into PBS over 28 days. The higher the collagen content the slower the HA degradation rate, when we compared three different Coll:HA:mixing ratios: Coll:HA = 2:1, Coll:HA = 1:1, Coll:HA = 1:2. After 28 days in PBS, the pure collagen scaffolds and two groups of Coll:HA = 2:1 and Coll:HA = 1:1 remained intact despite the loss of HA. However, the structure of pure HA and the other group of Coll:HA = 1:2 appeared to disintegrate (Fig. 4A and B).

The pure Coll scaffolds showed only minor mass loss in the total period of 4 weeks in solution. In contrast, it was not possible to reliably recover the HA–Coll scaffolds for weight measurement at the end of the 28-day period.

3.5. Unconfined compression and tension test results

The compressive stress–strain curves for the hydrated scaffolds (Fig. 5A and B) displayed the typical characteristics of low-density, open-cell foams [7]. Distinct linear elastic, collapse plateaus and densification regimes were observed in all cases. The linear elastic-collapse plateau transition was typically observed at approximately 5% strain, while densification was not observed until very large

Table 1
Properties of the scaffolds (mean ± SEM).

Sample[a]	% porosity ($n = 6$)	Mean apparent density (g cm^{-3}; $n = 6$)	Degree of crosslinking (%; $n = 4$)	Water absorp., fold inc. (wt) ($n = 6$)	Compression ($n = 6$)		Tension ($n = 6$)	
					Yield strength, 5% strain (Pa)	Modulus, 5% strain (kPa)	Peak strength (Pa)	Modulus, 5% strain (kPa ×10^{-2})
(A) Type I Coll	75 ± 8	0.0335	88 ± 0.4	26.6 ± 0.4[c]	315 ± 16	6.31 ± 0.33	2.7 ± 0.1	90 ± 3
(B) I:HA = 2:1	84 ± 2	0.0311	81 ± 1.1	31.4 ± 0.8	246 ± 8	4.91 ± 0.17	NA	NA
(C) I:HA = 1:1	88 ± 1	0.0276	71 ± 2	34.3 ± 0.3	176 ± 17	3.52 ± 0.35	NA	NA
(D) I:HA = 1:2	91 ± 1	0.027	57 ± 0.6	36.7 ± 0.5	136 ± 29	2.72 ± 0.57	1.0 ± 0.1	13 ± 1
(E) Type II Coll	76 ± 1	0.0322	81 ± 0.4	26.4 ± 0.4	262 ± 41	5.24 ± 0.82	1.4 ± 0.1	81 ± 1
(F) II:HA = 2:1	84 ± 0.4	0.0262	71 ± 0.9	33.1 ± 0.7	136 ± 24	2.72 ± 0.48	NA	NA
(G) II:HA = 1:1	90 ± 2	0.023	62 ± 3	36.3 ± 0.5	116 ± 17	2.32 ± 0.33	NA	NA
(H) II:HA = 1:2	91 ± 1	0.0174	49 ± 0.8	38.2 ± 0.7	93 ± 25	1.86 ± 0.50	1.8 ± 0.1	12 ± 1
(I) HA	80 ± 1	0.0202	17 ± 4	62.6 ± 1	67 ± 10	1.33 ± 0.20	0.23 ± 0.02	8 ± 1
(J) Brain tissue	76 ± 1	0.0252[b]	NA	NA	53 ± 8	1.06 ± 0.17	0.30 ± 0	13 ± 0.4

[a] Letters refer to samples in Figs. 2 and 5.
[b] Value of hydrated cortical samples divided by volume.
[c] 26.6-fold increase in weight.

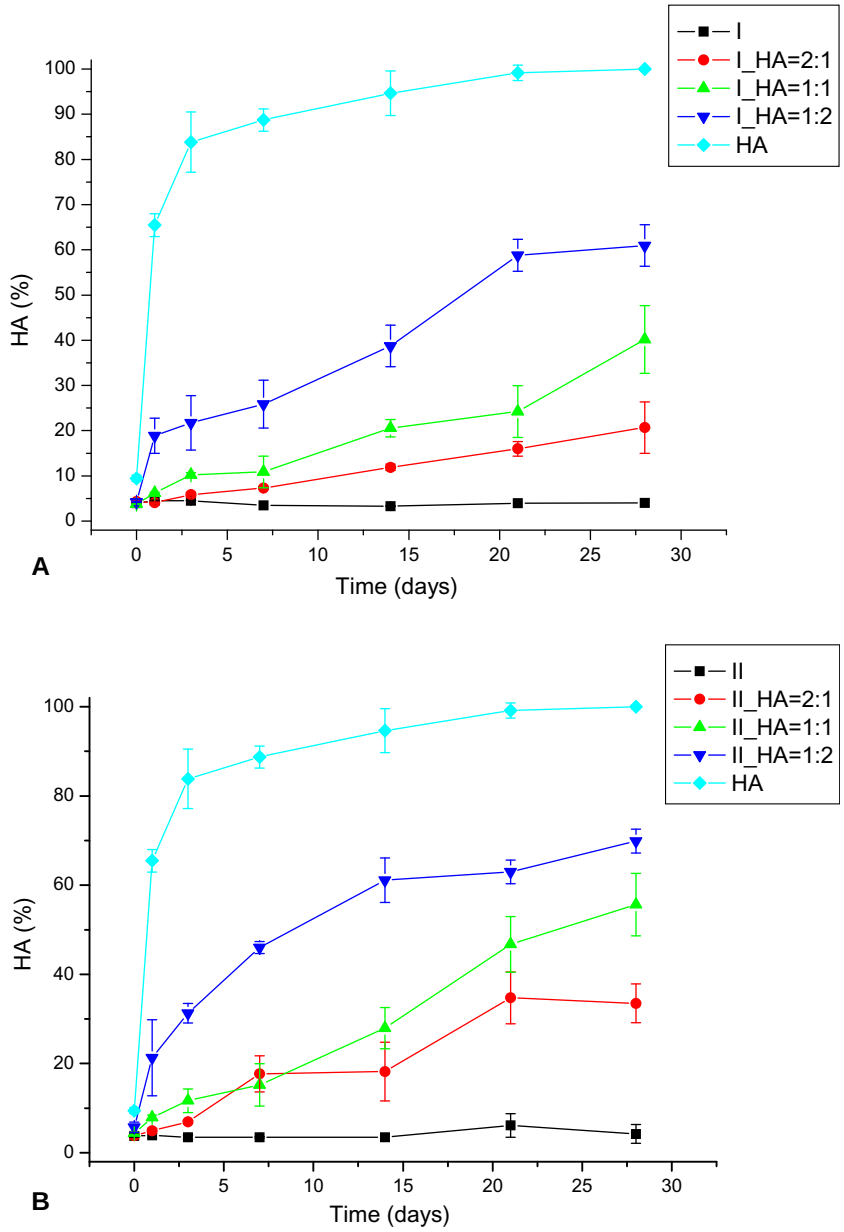

Fig. 4. The accumulated releasing profile of HA with time from crosslinked Coll, HA, and HA–Coll scaffolds with different mixing ratios.

strains >80%. The linear elastic region was mainly controlled by strut bending. Strut buckling and pore collapse occurred in the plateau region, followed by complete pore collapse in the densification region. The pure types I and II Coll scaffolds displayed similar compressive behavior (Fig. 5A and B), with the type II scaffolds displaying about 15% lower strength and modulus (Table 1). Addition of HA to the types I and II Coll scaffolds substantially reduced compressive strength and modulus (Table 1). The values for the HA–Coll scaffolds with Coll:HA = 1:2 were less than 50% of the values for the respective collagen scaffolds. (Table 1). The stress–strain behavior of the brain tissue was most like that of the pure HA scaffold. The compressive modulus of brain tissue (1.24 kPa) fell between the values for the pure crosslinked HA sponge and the Coll:HA = 1:2 group (Table 1; Fig. 5A and B).

Two-way ANOVA showed that there were significant effects of collagen type ($p = 0.0003$; power = 0.98) and HA content ($p < 0.0001$; power = 1) on the 5% off-set compressive yield strength and modulus. There was no statistically significant difference in the compressive strength or modulus of the brain tissue when compared to the pure HA scaffold ($p = 0.33$) albeit with a low power (0.15).

Of note was a strong linear correlation between the compressive modulus with the apparent density for the type I HA–Coll scaffolds, $R^2 = 0.99$, and a modest correlation for the type II HA–Coll scaffolds, $R^2 = 0.76$, by linear regression analysis.

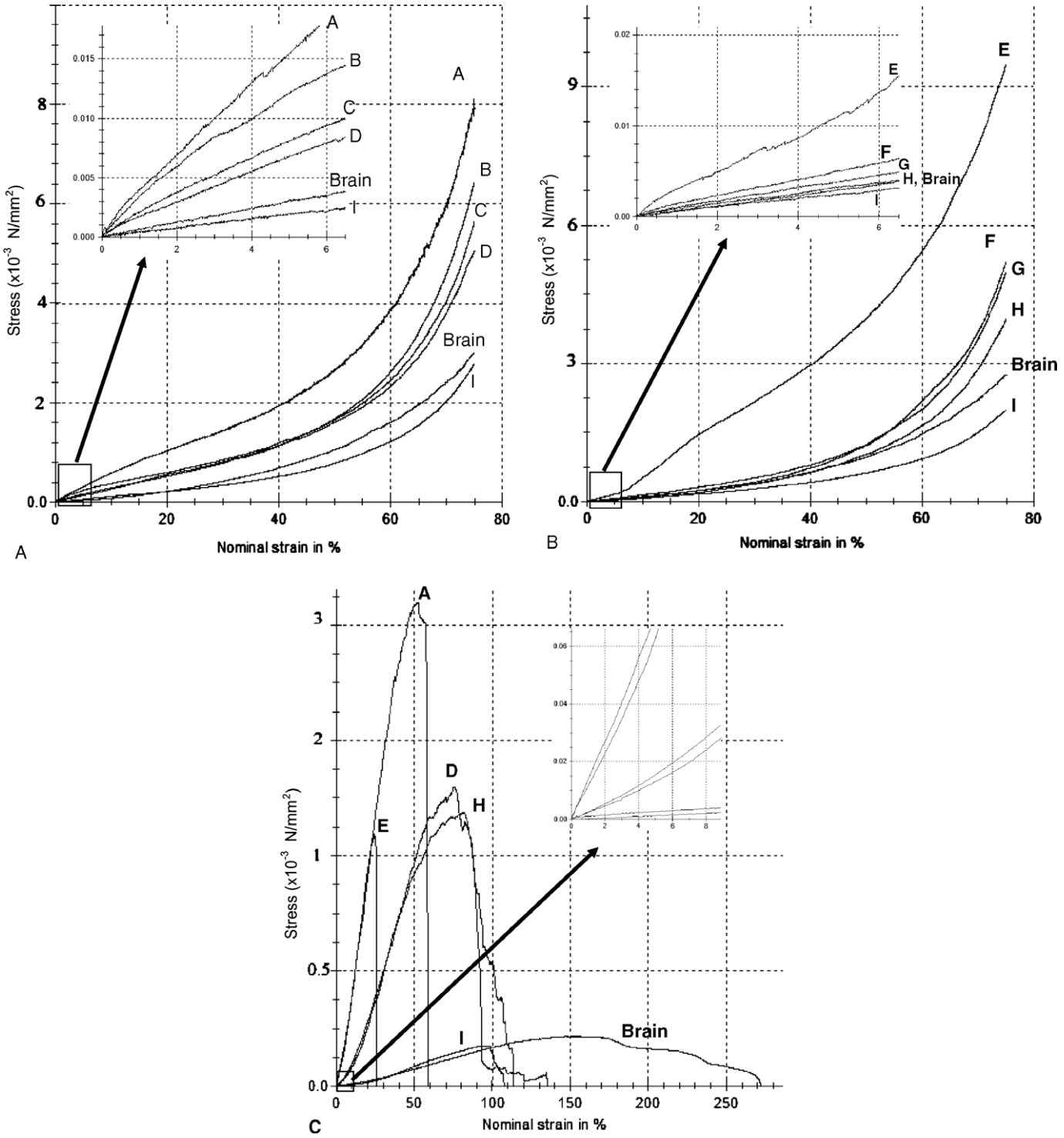

Fig. 5. Stress–strain curves from the mechanical tests of selected scaffolds and brain tissue. (A) Compression tests of pure type I collagen, HA–Coll type I composite, and pure HA scaffolds. (B) Compression tests of pure type II collagen, HA–Coll II composite and pure HA scaffold. (C) Tension test of pure collagen, HA–collagen composite and pure HA scaffold. A, type I Coll; B, type I Coll:HA = 2:1; C, type I Coll:HA = 1:1; D, type I Coll:HA = 1:2; E, type II Coll; F, type II Coll:HA = 2:1; G, type II Coll:HA = 1:1; H, type II Coll:HA = 1:2; I, HA.

The tensile stress–strain curves for the collagen and HA–Coll scaffolds increased to a peak value and then dropped to zero. The behavior for the brain tissue in tension differed from the scaffolds in that the stress decreased gradually to zero after the peak value was reached (Fig. 5C). Moreover, whereas the compression behavior of the types I and II scaffolds was similar, the peak tensile strength of the type I scaffold was about 2-fold higher than for the type II scaffold (Table 1). While addition of HA resulted in a substantial decrease in the peak tensile

strength of the type I collagen scaffolds (by >2.5-fold), the addition of HA to the type II samples slightly increased the peak tensile strength (Table 1). The tensile modulus of elasticity of the type II scaffold was about 10% less than the modulus of the type I scaffold (Table 1). Addition of HA to both the types I and type II scaffolds greatly decreased (by 6- to 7-fold) the tensile modulus of the samples (Table 1).

Two-way ANOVA revealed statistically significant effects of collagen type ($p < 0.0001$; power = 1) and HA content ($p = 0.0005$; power = 0.98) on the peak tensile strength of the samples, and on the tensile modulus at 5% strain ($p = 0.015$; power = 0.73 and $p < 0.0001$; power = 1, respectively). One-way ANOVA of the type II collagen scaffolds showed that the 29% increase in the peak tensile strength with the addition of HA (HA:Coll = 1:2) was statistically significant ($p = 0.0009$; power = 0.99).

3.6. Culture of NSCs in a 2-D environment

The NSCs which were isolated from rat brain tissue and grown on tissue culture dish surfaces assembled to form distinct neurospheres. After 7 days in culture, cells could be found attached to the culture surface, and neurite extensions were observed. Within a few additional days the number of cells attached to the dish and the size of the neurospheres increased. Neural networks including neurite outgrowth and axon extension were also seen. Cone-like morphologies and oval and spindle-shaped long processes consistent with neuronal and glial phenotypes were observed.

3.7. Differentiation and maturation of NSCs in 3-D scaffolds

The cell-seeded HA scaffolds displayed signs of fragmentation at the end of the 2 week culture period. While cells staining for neuronal cell markers could be seen distributed though the Coll, HA–Coll, and HA scaffolds (Fig. 6), the cell distribution was different among the groups. In HA–Coll and HA scaffolds (Fig. 6D and 6G), cells appeared to assemble into clusters displaying the typical features of neurospheres. In contrast, cells in the collagen scaffolds were dispersed sparsely and did not form neurospheres (Fig. 6A). Nestin, a neurospecific intermediate filament protein [28], was prominent in cells in the three different groups of scaffolds. The intensity of expression and density of MAP2, which is used for labeling of dentritic trees of mature neurons, was much higher in the HA–Coll samples than in the HA scaffolds (Fig. 6E and H). In comparison, there was little expression of MAP2 by cells in the Coll scaffolds (Fig. 6B).

The neuron-specific nuclear protein, NeuN, was also expressed prominently surrounding the nuclei in the cells in HA–Coll and HA scaffolds (Fig. 6E and H). Tuj-1 was found exclusively in the neuronal processes in all the groups (Fig. 6C, F,I).

4. Discussion

The results of this study provide a basis for the preparation of HA–Coll scaffolds for neural tissue engineering. While HA is the major extracellular matrix component of adult central nervous system tissues, and collagen a lesser component if even present, there are several potential benefits of an HA–Coll scaffold for neural tissue engineering. The principal benefits of incorporation of collagen in HA scaffolds relate to: (i) the control that it offers over strength, stiffness and degradation rate; and (ii) the fact that collagen may provide ligands for the integrins of neuronal support cells necessary during the regeneration process. Of potential relevance is that prior studies have found that embryonic spinal cord epithelium [29] and chick neural retina tissue [30] synthesize type II collagen, indicating that collagen in addition to HA may play an important role in the formation of select nervous tissues. These findings also underlie the rationale for the ultimate comparison of the performance of types I and II collagens for neural applications.

The findings of the current work demonstrate the effects that the increasing content of HA have on the physical and mechanical properties of the HA–Coll composite scaffolds prepared using the same freeze-drying protocol. This work serves as a guideline for how the processing (viz. freezing) conditions may have to be changed to produce select HA–Coll scaffolds with properties to meet certain design specifications. Including brain tissue as a comparative control in this investigation provided the opportunity to begin to determine how best to prepare an HA–Coll scaffold to match selected physical and mechanical properties of the brain. While the pure HA scaffold came closest to replicating the mechanical behavior of brain tissue, those scaffolds may not ultimately prove to have sufficient handling properties for a tissue engineering approach to treating defects in the brain.

While the effects of increasing HA content on the pore diameter were clear and quantifiable, the effects of HA in increasing the apparent perforations in the walls of the pores, which confirmed the finding in our prior work [13], was less clear. This effect may increase the interconnecting pore diameter distribution which was not measured in this study. Additional work will be required to determine the importance of this effect in the context of the use of the scaffold for tissue engineering.

One of the effects of increasing the HA content on the HA–Coll scaffolds was to interfere with crosslinking (reduced from nearly 90% down to around 50%). This may be explained by the fact that the hydroxyl groups on HA may attach to the carboxyl groups either on HA or collagen, resulting in aliphatic ester bond formation under low water environment [31]. With the consumption of these carboxyl groups, the amino groups on collagen may not have enough binding sites with carboxyl to form covalent linkage, thus resulting in the low degree of crosslinking as determined by the TNBS assay.

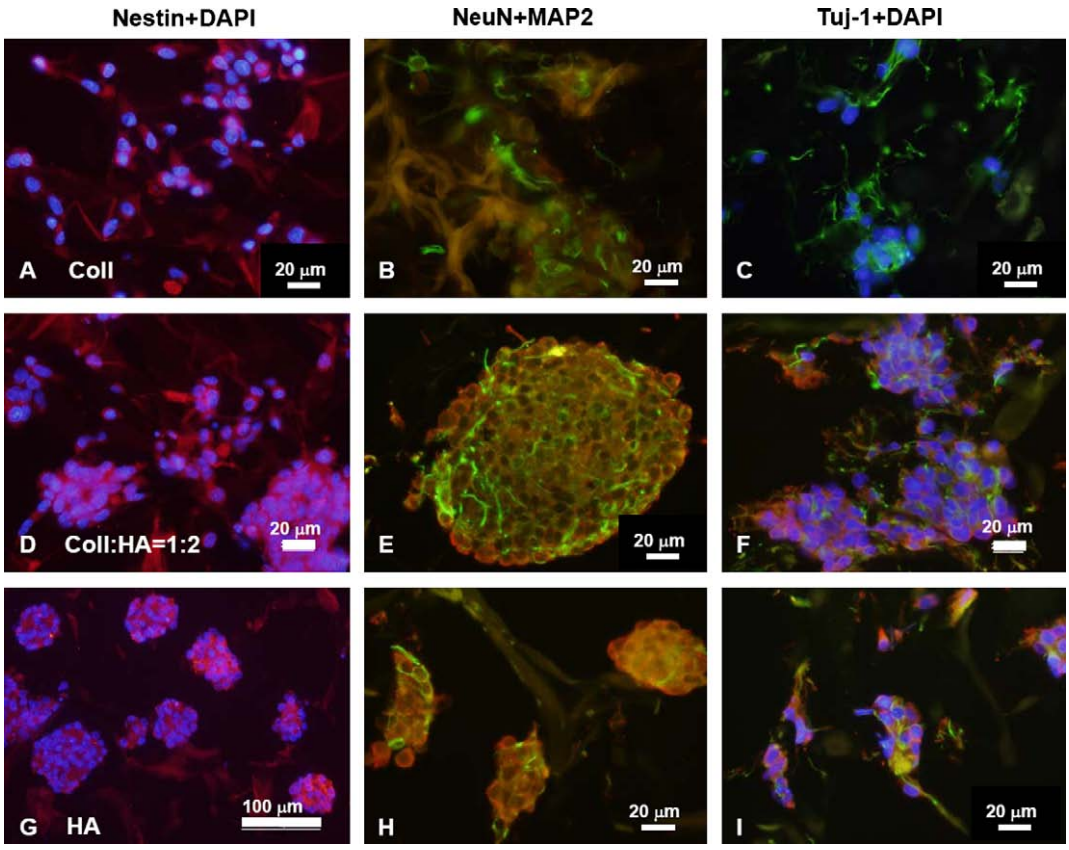

Fig. 6. Immunochemistry of NSCs grown in scaffolds in neurogenic medium, 2 weeks after seeding. The nucleus was stained blue with DAPI. Neurospecific intermediate filament protein (Nestin) and neuron-specific nuclear protein (NeuN) are in red, and tubulin β III (Tuj-1) and major microtubule associated protein (MAP2) are in green. (A–C) type I Coll scaffold; (D–F) HA-type I Coll scaffold with Coll:HA = 1:2; and (G–I) HA scaffold. (For interpretation of the references to color in this figure legend, the reader is referred to the web version of this paper.)

The EDAC crosslinking of HA is enabled by the intermolecular formation of ester bonds between the hydroxyl and carboxyl groups [11] in this GAG molecule. EDAC seems to mediate acid anhydride formation between two carboxyl groups belonging to the same or different GAG molecules. The resultant acid anhydride may readily react with a hydroxyl group of GAGs to yield an ester bond, which functions as a crosslink of HA molecules. Since the acid anhydride formed is very unstable at room temperature in aqueous environments, it will be hydrolyzed back to the original carboxyl groups unless any nucleophilic groups, such as hydroxyl, quickly encounter the acid anhydride. This high degree of instability may explain why our method by means of sponge immersion in EDAC was not so effective for crosslinking pure HA. Future studies need to investigate the crosslinking of HA molecules though an amide bond which is more resistant to hydrolysis than an ester bond. For example, L-lysine might be added to the HA solution in order to facilitate EDAC crosslinking [32].

The minor mass loss of the pure Coll scaffolds in the 4 week period may be explained by the fact that most of the carboxyl and amino groups on the Coll scaffolds likely reacted with the EDAC crosslinking agent during the crosslink reaction process, resulting in covalent amide bond formation which can strongly resist hydrolysis in aqueous environment. There was a substantial stabilization of HA in the scaffolds by the Coll, as shown in the release experiments, and which was documented in our prior studies [13,33]. Whereas the pure HA scaffolds lost about 90% of their HA content within the first 5 days, 40% of the HA was still retained in the Coll:HA = 1:2 scaffolds after 4 weeks. There were no remarkable differences noted in the retention of HA in the types I and II Coll scaffolds. Because type II Coll is the principal collagen type in hyaline cartilages which have high HA contents, one might have expected a greater retention of HA in the type II Coll scaffolds compared to the type I Coll samples. A limitation in the HA release experiments was that the amount of HA released into the PBS was divided by the amount of HA originally incorporated into the scaffolds. However, there is a possibility that some of this HA leached into the 80% ethanol solution used for the EDAC crosslinking, before the crosslinking reaction occurred.

The most notable difference between the types I and II Coll scaffolds in this study was related to the mechanical behavior. The type I Coll scaffolds were 20% higher in compressive yield strength and 93% higher in peak tensile strength. The mean value of the compressive modulus of the type I Coll samples (6.3 kPa) fell within the range of

values previously reported for collagen–GAG scaffolds of comparable pore characteristics crosslinked with EDAC [7]. Addition of HA to the Coll scaffolds provided the methodology to vary the compressive and tensile moduli (and stiffness) over wide ranges.

A notable finding of the present study was high linear correlation between compressive modulus and apparent density for the Coll and HA–Coll scaffolds, as was found in prior studies of porous collagen scaffolds [7], deviating from the squared dependence predicted by open cell foam theory [34]. In our study, the reason why the dependence of modulus on density did not follow foam theory is likely that the mechanical properties of the struts comprising the scaffolds of varying density changed with the Coll:HA ratio. Future studies of the relationships among the mechanical and physical properties and composition for HA–Coll materials will be of value to perform.

The mechanical testing of brain tissue in the present study was carried out using the same methods that were used for the scaffolds, in order to generate comparative data. Several prior studies of the mechanical properties of brain tissue have employed an array of test methods that recognized the viscoelastic behavior of the tissue, its high water content, and heterogeneity [35–38]. The compressive modulus of our HA–Coll composite matrices was around 1–2 kPa, which paralleled that of brain tissue (0.1–1 kPa) as reported in other studies [39].

Recent studies have demonstrated that substrate elasticity can guide lineage specification and phenotype commitment of mesenchymal stem cells [39], with substrates having a modulus of about 1 kPa favoring neurogenic differentiation. Other studies have shown that neuronal and glial cells responses are also favored by growth on soft gels [40]. These prior studies investigating the effects of the mechanical environment on neurogenesis were conducted on 2-D substrates. Our preliminary investigation of the behavior of NSCs in Coll and HA–Coll scaffolds demonstrated that the cells were capable of being induced to differentiate into neuronal cells in the 3-D environment. The most noticeable difference in the behavior of the cells in the various scaffolds was their formation of neurosphere-like structures in the more compliant HA and HA–Coll matrices, whereas the cells appeared to stay dispersed in the stiffer type II Coll scaffolds. Moreover, the neuronal cells in the Coll were not labeled as prominently for MAP2 indicating a less mature neuronal phenotype. These findings, which suggest that the HA and HA–Coll scaffolds were more preferable to NSCs, warrant additional study.

The observation that the stiffness of the 3-D scaffold may affect the aggregation of cells is consistent with studies of another cell type that demonstrated that compliant collagen scaffolds enabled the cell-mediated contraction of scaffolds and condensation of chondrocytes required for chondrogenesis [4,41]. This condensation and chondrogenesis was not seen, or greatly delayed, in scaffolds of higher stiffness.

5. Conclusions

Complexing HA with types I and II Coll enables the fabrication of scaffolds with a range of physical and mechanical properties suitable for neural tissue engineering applications, involving the treatment of defects in the brain. The compressive modulus increases linearly with the apparent density of the specimens. HA and HA–Coll scaffolds, which parallel certain mechanical behaviors of brain tissue, favor the differentiation of NSCs to neuronal cells in vitro.

Acknowledgements

Funding for this work was provided by the Department of Veterans Affairs and the Department of Defense. M.S. is a Veterans Affairs Research Career Scientist.

References

[1] Ellis DL, Yannas IV. Recent advances in tissue synthesis in vivo by use of collagen–glycosaminoglycan copolymers. Biomaterials 1996;17:291–9.
[2] Hutmacher DW. Scaffold design and fabrication technologies for engineering tissues – state of the art and future perspectives. J Biomater Sci Polym Ed 2001;12(1):107–24.
[3] Wang TW, Wu HC, Huang YC, Sun JS, Lin FH. Biomimetic bilayered gelatin–chondroitin 6 sulfate–hyaluronic acid biopolymer as a scaffold for skin equivalent tissue engineering. Artif Organs 2006;30(3):141–9.
[4] Vickers SM, Squitieri LS, Spector M. Effects of cross-linking type II collagen–GAG scaffolds on chondrogenesis in vitro: dynamic pore reduction promotes cartilage formation. Tissue Eng 2006;12(5):1345–55.
[5] Wang TW, Sun JS, Wu HC, Tsuang YH, Wang WH, Lin FH. The effect of gelatin–chondroitin sulfate–hyaluronic acid skin substitute on wound healing in SCID mice. Biomaterials 2006;27(33):5689–97.
[6] Ninomiya Y, Olsen BR, Ooyama T, editorsExtracellular matrix–cell interaction: molecules to diseases. Basel Switzerland: Karger; 1998.
[7] Harley BA, Leung JH, Silva EC, Gibson LJ. Mechanical characterization of collagen–glycosaminoglycan scaffolds. Acta Biomater 2007;3(4):463–74.
[8] Bignami A, Hosley M, Dahl D. Hyaluronic acid and hyaluronic acid-binding proteins in brain extracellular matrix. Anat Embryol 1993;188:419–33.
[9] Yasuhara O, Akiyama H, McGeer EG, McGeer PL. Immunohistochemical localization of hyaluronic acid in rat and human brain. Brain Res 1994;635(1–2):269–82.
[10] Rehakova M, Bakos D, Vizarova K, Soldan M, Jurickova M. Properties of collagen and hyaluronic acid composite materials and their modification by chemical crosslinking. J Biomed Mater Res 1996;30(3):369–72.
[11] Segura T, Anderson BC, Chung PH, Webber RE, Shull KR, Shea LD. Crosslinked hyaluronic acid hydrogels: a strategy to functionalize and pattern. Biomaterials 2005;26(4):359–71.
[12] Morra M. Engineering of biomaterials surfaces by hyaluronan. Biomacromolecules 2005;6(3):1205–23.
[13] Tang S, Vickers SM, Hsu HP, Spector M. Fabrication and characterization of porous hyaluronic acid–collagen composite scaffolds. J Biomed Mater Res 2007;82(2):323–35.
[14] Park SN, Lee HJ, Lee KH, Suh H. Biological characterization of EDC-crosslinked collagen–hyaluronic acid matrix in dermal tissue restoration. Biomaterials 2003;24(9):1631–41.

[15] Liu LS, Thompson AY, Heidaran MA, Poser JW, Spiro RC. An osteoconductive collagen/hyaluronate matrix for bone regeneration. Biomaterials 1999;20(12):1097–108.
[16] Price RD, Myers S, Leigh IM, Navsaria HA. The role of hyaluronic acid in wound healing: assessment of clinical evidence. Am J Clin Dermatol 2005;6(6):393–402.
[17] Bourguignon LY, Gilad E, Peyrollier K, Brightman A, Swanson RA. Hyaluronan–CD44 interaction stimulates Rac1 signaling and PKN gamma kinase activation leading to cytoskeleton function and cell migration in astrocytes. J Neurochem 2007;101(4):1002–17.
[18] Bandtlow CE, Zimmermann DR. Proteoglycans in the developing brain: new conceptual insights for old proteins. Physiol Rev 2000;80(4):1267–90.
[19] Sherman LS, Struve JN, Rangwala R, Wallingford NM, Tuohy TM, Kuntz Ct. Hyaluronate-based extracellular matrix: keeping glia in their place. Glia 2002;38(2):93–102.
[20] Margolis RU, Margolis RK, Chang LB, Preti C. Glycosaminoglycans of brain during development. Biochemistry 1975;14(1):85–8.
[21] Sherman LS, Struve JN, Rangwala R, Wallingford NM, Tuohy TM, Kuntz C 4th. Hyaluronate-based extracellular matrix: keeping glia in their place. GLIA 2002; 38(2):93–102.
[22] O'Brien FJ, Harley BA, Yannas IV, Gibson L. Influence of freezing rate on pore structure in freeze-dried collagen–GAG scaffolds. Biomaterials 2004;25(6):1077–86.
[23] Olde Damink LH, Dijkstra PJ, van Luyn MJ, van Wachem PB, Nieuwenhuis P, Feijen J. Cross-linking of dermal sheep collagen using a water-soluble carbodiimide. Biomaterials 1996;17(8): 765–73.
[24] Park SN, Park JC, Kim HO, Song MJ, Suh H. Characterization of porous collagen/hyaluronic acid scaffold modified by l-ethyl-3-(3-dimethylaminopropyl)carbodiimide cross-linking. Biomaterials 2002;23(4):1205–12.
[25] Tomihata K, Ikada Y. Crosslinking of hyaluronic acid with water-soluble carbodiimide. J Biomed Mater Res 1997;37(2):243–51.
[26] Ofner 3rd CM, Bubnis WA. Chemical and swelling evaluations of amino group crosslinking in gelatin and modified gelatin matrices. Pharm Res 1996;13(12):1821–7.
[27] Bitter T, Muir HM. A modified uronic acid carbazole reaction. Anal Biochem 1962;4:330–4.
[28] Gotz M, Huttner WB. The cell biology of neurogenesis. Nat Rev Mol Cell Biol 2005;6(10):777–88.
[29] Trelstad RL, Kang AH, Cohen AM, Hay ED. Collagen synthesis in vitro by embryonic spinal cord epithelium. Science 1973;179(70):295–7.
[30] Smith Jr GN, Linsenmayer TF, Newsome DA. Synthesis of type II collagen in vitro by embryonic chick neural retina tissue. Proc Natl Acad Sci USA 1976;73(12):4420–3.
[31] Hermanson GT. Bioconjugate techniques. San Diego, CA: Academic Press; 1996.
[32] Tian WM, Hou SP, Ma J, Zhang CL, Xu QY, Lee IS, et al. Hyaluronic Acid–poly-D-lysine-based three-dimensional hydrogel for traumatic brain injury. Tissue Eng 2005;11(3–4):513–25.
[33] Tang S, Spector M. Incorporation of hyaluronic acid into collagen scaffolds for the control of chondrocyte-mediated contraction and chondrogenesis. Biomed Mater Mater Tissue Eng Regen Med 2007:S135–41.
[34] Gibson LJ, Ashby MF. Cellular solids: structure and properties. Cambridge: Cambridge University Press; 1997.
[35] Gefen A, Gefen N, Zhu Q, Raghupathi R, Margulies SS. Age-dependent changes in material properties of the brain and braincase of the rat. J Neurotrauma 2003;20(11):1163–77.
[36] Gefen A, Margulies SS. Are in vivo and in situ brain tissues mechanically similar? J Biomech 2004;37(9):1339–52.
[37] Prange MT, Margulies SS. Regional, directional, and age-dependent properties of the brain undergoing large deformation. J Biomech Eng 2002;124(2):244–52.
[38] Coats B, Margulies SS. Material properties of porcine parietal cortex. J Biomech 2006;39(13):2521–5.
[39] Engler AJ, Sen S, Sweeney HL, Discher DE. Matrix elasticity directs stem cell lineage specification. Cell 2006;126(4):677–89.
[40] Georges PC, Miller WJ, Meaney DF, Sawyer ES, Janmey PA. Matrices with compliance comparable to that of brain tissue select neuronal over glial growth in mixed cortical cultures. Biophys J 2006;90(8):3012–8.
[41] Pfeiffer E, Vickers SM, Frank E, Grodzinsky AJ, Spector M. The effects of glycosaminoglycan content on the compressive modulus of cartilage engineered in type II collagen scaffolds. Osteoarthitis Cartilage 2008;16:1237–44.

ADVANCED FUNCTIONAL MATERIALS
www.afm-journal.de

Novel Magnetic Hydroxyapatite Nanoparticles as Non-Viral Vectors for the Glial Cell Line-Derived Neurotrophic Factor Gene

By *Hsi-Chin Wu, Tzu-Wei Wang, Martha C. Bohn, Feng-Huei Lin,** and *Myron Spector**

Nanoparticles (NPs) of synthetic hydroxyapatite (Hap) and natural bone mineral (NBM) are rendered magnetic by treatment with iron ions using a wet-chemical process. The magnetic NPs (mNPs), which are about 300 nm in diameter, display superparamagnetic properties in a superconducting quantum interference device, with a saturation magnetization of about 30 emu g^{-1}. X-ray diffraction and transmission electron microscopy reveal that the magnetic properties of the NPs are the result of the hetero-epitaxial growth of magnetite on the Hap and NBM crystallites. The mNPs display a high binding affinity for plasmid DNA in contrast to magnetite NPs which do not bind the plasmid well. The mHap and mNBM NPs result in substantial increases in the transfection of rat marrow-derived mesenchymal stem cells with the gene for glial cell line-derived neurotrophic factor (GDNF), with magnetofection compared to transfection in the absence of a magnet. The amount of GDNF recovered in the medium approaches therapeutic levels despite the small amount of plasmid delivered by the NPs.

1. Introduction

While the concept of nanoparticle (NP) drug delivery is not new,[1,2] technological advances have accelerated recent development of NPs as delivery vehicles for a wide array of therapeutic agents. NPs have undergone investigation for myriad applications—including treatment of tumors by delivery of anticancer agents,[3–6] and treatment of focal degenerative conditions and enhancement of tissue repair/regeneration through delivery of select proteins and their encoding genes[7–10] and regulating RNA.[9] Challenges in employing NPs for the delivery of therapeutic agents include their targeting of, and their retention at, a specific site. Directing blood-borne NPs to sites in the brain is further complicated by the blood–brain barrier.[11–13] One recent development which holds the promise of meeting these challenges, so that the potential of NP drug and gene delivery can be realized, is the magnetic control of the particles.[13–15]

Superparamagnetic NPs (mNPs), which can be attracted to and maintained at a precise location by an external magnet, have been of recent interest for numerous applications. This approach has the potential for targeting anticancer drugs to a tumor,[16,17] and is of particular interest for the treatment of brain tumors which are difficult to access.[13,18] Other studies have investigated mNPs for the site-specific delivery of genes and the enhancement of transfection. The term magnetofection was coined to describe the action of a magnetic force on gene vectors combined with magnetic particles.[15] These magnetic vectors have been exclusively based

[*] Prof. M. Spector, H.-C. Wu, T.-W. Wang
Tissue Engineering Laboratories
VA Boston Healthcare System
150 S. Huntington Ave.
Boston, MA, 02130 (USA)
E-mail: mspector@rics.bwh.harvard.edu
Prof. M. Spector, T.-W. Wang
Department of Orthopaedic Surgery
Brigham and Women's Hospital
Harvard Medical School
75 Francis St.
Boston, MA, 02115 (USA)
F.-H. Lin, H.-C. Wu
Institute of Biomedical Engineering
National Taiwan University
No. 1, Sec. 1, Jen-Ai Rd., Jongjheng District
Taipei City 100 (Taiwan)
E-mail: double@ntu.edu.tw
H.-C. Wu
Division of Medical Sciences Visiting Fellows Program
Harvard Medical School
260 Longwood Ave.
Boston, MA, 02115 (USA)
T.-W. Wang
Department of Materials Sciences and Engineering
National Tsing Hua University
No. 101, Section 2, Kuang-Fu Road
Hsinchu 30013 (Taiwan)
M. C. Bohn
Children's Memorial Research Center
Northwestern University
2430 N. Halsted
Chicago, IL 60614 (USA)

DOI: 10.1002/adfm.200901108

Final page numbers not assigned

on iron oxide, for which there has been some concern related to cytotoxicity.[19]

Prompted by the need to develop safe and effective magnetic NPs, our prior preliminary work[20] introduced well-controlled, wet-chemical methods for producing magnetic calcium phosphate, viz., hydroxyapatite (Hap), NPs for an array of biomedical applications. Hap, $Ca_{10}(PO_4)_6(OH)_2$, which is stable at neutral pH, is the principal form of calcium phosphate in the body—the mineral constituent of hard tissues. Hap is commended as a biomaterial based on its biocompatibility and biodegradability,[21] and has been used as a delivery vehicle for proteins[22] and genes.[23,24]

The objective of the present study was to extend our methodology[20] to produce magnetic synthetic Hap (mHap) NPs and magnetic natural bone mineral (mNBM) NPs as non-viral vectors for the plasmid DNA (pDNA) encoding a potent neurotrophic growth factor, glial cell line-derived neurotrophic factor (GDNF). The comparison of Hap and NBM was based on the fact that the crystallites of NBM are calcium-deficient carbonate apatite,[25–27] which may display different binding affinities for pDNA and possess other properties favorable for this application. Specific aims were to investigate the structure and properties of the mNPs and the temporal expression of GDNF by rat marrow stromal cells (also referred to as mesenchymal stem cells, MSCs) transfected in vitro by the mNPs under the action of a magnet.

GDNF is one of several neurotrophic factors which regulate many critical aspects of the ontogeny of neurons, such as the number of neurons in a given population, neurite branching and synaptogenesis, adult synaptic plasticity, and maturation of electrophysiological properties.[28] GDNF was first purified and described in 1993 as a growth factor promoting the survival of the embryonic dopaminergic neurons of the midbrain,[29,30] and later it was shown that GDNF is a trophic factor for spinal motoneurons[31] and central noradrenergic neurons.[32] GDNF gene delivery has been reported to be able to reverse age-related loss of dopamine neurons in the monkey brain and to prevent loss of dopamine neurons in rat and monkey models of Parkinson's disease, as well as lost of motoneurons in a mouse model of amyotrophic lateral sclerosis (ALS).[33–37] GDNF protein, when infused directly into brains of Parkinson's disease patients, has led to controversial outcomes related to disease progression.[38,39]

MSCs were selected for the in vitro study because endogenous stem/progenitor cells may be the targets for mNP non-viral vectors administered systemically and attracted to the brain by an external magnet. MSCs are also of interest for applications in which such cells, transfected ex vivo, might be used in cell therapy; mHap and mNBN NP magnetofection could be used for safe and effective transfection in vitro.

2. Results

2.1. Size of the Nanoparticles

The averaged particle size measurements of the NPs determined from dynamic light scattering (DLS) are indicated in Table 1. The iron-containing NPs were of smaller diameter than that of non-iron-containing groups, and the magnetite particles were substantially smaller than the calcium phosphate NPs. The difference in the recorded size of the NPs with and without iron may have been due to the greater dispersion (i.e., lower tendency to aggregate) of the mNPs due to charge repulsion associated with their greater number of negative surface charges as shown by zeta potential measurements (presented below). The aggregation of the NPs confounded scanning electron microscopy (SEM) identification of the morphology and size of individual NPs.

Table 1. Average particle size of the NPs as determined from DLS.

Particle	Average particle size [nm]
mHap	290
mNBM	294
Hap	579
NBM	559
Magnetite	109

2.2. Magnetic Properties of the Nanoparticles

The Hap and NBM NPs appeared as whitish powders. After addition of the iron ions and treatment with NH_4OH, the powder became black (Fig. 1a). The mHap and mNBM NPs were rapidly attracted by a magnet (Fig. 1a). Virtually all of the particles followed the movement of the magnet and could be extracted from suspensions using the magnet, leaving a clear solution (Fig. 1a). No such behavior was displayed by the Hap and NBM.

Superconducting quantum interference device (SQUID) analysis demonstrated the magnetization behavior versus applied magnetic field for the mHap and mNBM NPs (Fig. 1b). The saturation magnetization levels of the mHap and mNBM NPs were comparable at 28.7 and 29.6 emu g^{-1} in 5000 Oe of magnetic field, respectively. The absence of a hysteresis loop with reversal of the magnetic field indicated that there was no magnetic energy loss and was consistent with superparamagnetic behavior.

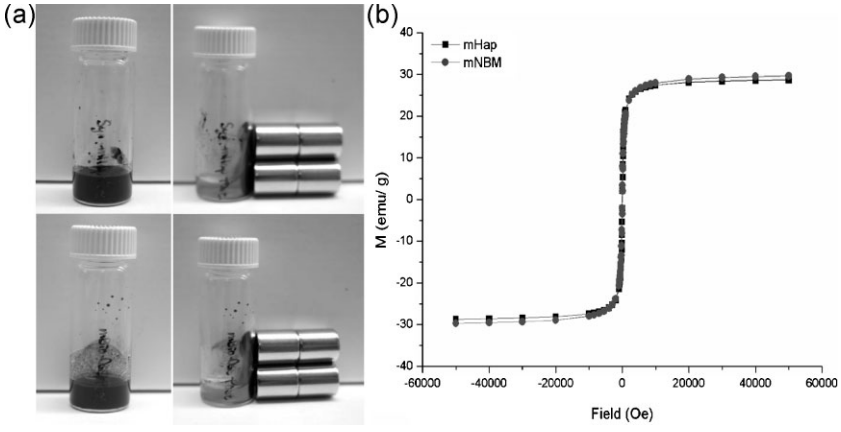

Figure 1. a) Photographs of the (top left) mHap and (bottom left) mNBM particles, in aqueous suspension, demonstrating their black color. Virtually all of the particles are attracted to the magnet (right panels), with the aqueous solution now appearing clear, as the particles are up against the side of the vial. b) The magnetization (*M*) loop from the SQUID analysis of mHap (square) and mNBM (circular) NPs measured at 300 K. The applied field is shown on the *x*-axis.

2.3. Crystalline Structure of the Nanoparticles

X-ray diffraction (XRD) confirmed the hydroxyapatite structure of the crystallites comprising the Hap (Fig. 2a) and NBM (Fig. 2c) NPs. The diffraction peaks from the NBM were broader than those from the Hap sample, indicating a smaller crystallite size in the NBM NPs. The size of the apatite crystallites along the *c* crystallographic axis (001 peak at $2\theta = 26^\circ$ in Fig. 2a and c) was estimated from line broadening to be 30 nm for NBM and 53 nm for Hap. These dimensions did not change significantly after the addition of the iron ions: 31 nm for mNBM (Fig. 2d) and 56 nm for mHap (Fig. 2b). The NBM pattern also displayed a greater percentage of noncrystalline material reflected in the higher background diffraction, particularly at higher diffraction angles. However, the calculation of the percent crystallinity from the XRD patterns yielded comparable values (~90%), with only a slight increase to 94% (mNBM) and 95% (mHap) after addition of the iron ions.

The locations and relative intensities of the hydroxyapatite diffraction peaks in the XRD patterns of mHap (Fig. 2b) and mNBM (Fig. 2d) were similar to those of the Hap and NBM samples indicating that the apatite structure of the NPs was maintained, with no noticeable alteration of the apatitic crystalline structure as a result of the addition of the iron ions. The hydroxyapatite peaks in the XRD patterns from mHap (Fig. 2b) and mNBM (Fig. 2d) samples, however, displayed decreased intensity compared to the patterns of the respective nonmagnetized Hap and NBM NPs. Of note in the XRD patterns from the mHap and mNBM NPs, compared to the nonmagnetic samples, were the pronounced additional peaks at the 2θ values of 30.1° and 35.4°. These were identified as magnetite from the Joint Committee on Powder Diffraction Standards (JCPDS) card #19-0629 (Fig. 2).

The lattice parameters for the mNBM samples increased slightly as result of addition of the iron ions, while there was no apparent difference between the lattice constants for the Hap and mHap crystallites.

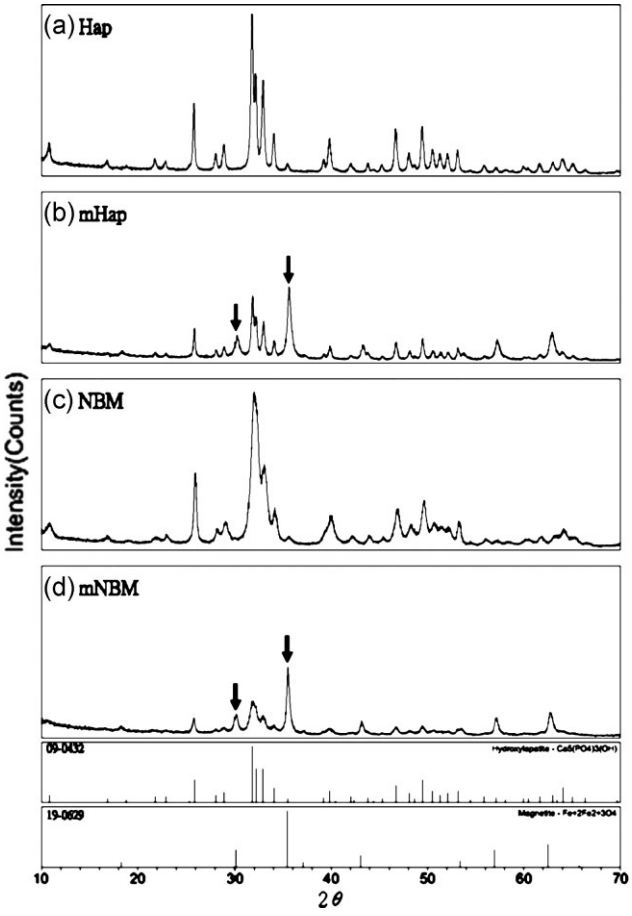

Figure 2. The X-ray diffraction patterns of a) Hap, b) mHap, c) NBM, and d) mNBM. The identity of the peaks was based on reference profiles in the JCPDS for hydroxyapatite [card #09-0432; $Ca_5(PO_4)(OH)$] and magnetite [card #19-0629; Fe_3O_4]. The arrows in the mHap and mNBM patterns show the magnetite peaks.

2.4. Chemical Content and Ultrastructure of the Nanoparticles

The calcium:phosphorus molar ratios determined from inductively coupled plasma–optical emission spectroscopy (ICP-OES) analysis of the Hap and NBM were 1.77 and 1.78. There was no Fe detected in the Hap and NBM. After the addition of iron for the synthesis of the mHap and mNBM, there was only a slight drop in the calcium:phosphorus ratio for the mHap and mNBM to 1.77 and 1.77, respectively, indicating that most of the iron had not been substituted for calcium. The Ca:P:Fe ratios of the mHap and mNBM NPs were comparable.

Transmission electron microscopy (TEM) revealed the clusters of crystallites making up the Hap and NBM NPs which were from about 200–400 nm in diameter (Fig. 3a–d). The crystallites making up the Hap NPs appeared in TEM in rod- and lath-like morphologies, 50–100 nm long by about 25 nm wide (Fig. 3a). In some views, the crystallites displayed small electron-lucent holes, consistent in appearance with electron-beam damage. The crystallites making up the NBM NPs (Fig. 3b) generally appeared shorter (about 30 nm in length), and they were noticeably thinner (about 10 nm in width) than the Hap crystallites. In some cases the NBM crystallites displayed an electron-dense needle-like appearance (Fig. 3b) which was likely due to the lath-like crystallites being viewed on edge. The ultrastructural findings for the NBM crystallites were consistent with prior TEM and high-resolution SEM studies of the crystallites from anorganic bovine bone.[40]

Of note was the additional presence of small irregularly shaped discs, less than 10 nm in diameter, in the samples of the iron-containing mHap and mNBM NPs (Fig. 3c,d). These features were generally found superimposed on the Hap and NBM crystallites and could be distinguished based on their electron-dense silhouettes. Occasionally, there appeared to be clusters of these small discs, but it was not possible to determine if these features were the result of aggregation of the discs or their association with an underlying Hap or NBM crystallite. The respective crystallite sizes and morphologies of the Hap and NBM crystallites in the mHap (Fig. 3c) and mNBM (Fig. 3d) samples appeared to be comparable with the sizes and morphologies of the crystallites in the samples which did not contain iron (Fig. 3a,b). The presence of the disc-like features, however, often obscured the morphology of the Hap and NBM crystallites. In some views, it appeared that there were more of the disc-like features in the mNBM NPs than in the Hap NPs, but this was not quantified.

The Fourier images from high-resolution TEM of the mHap demonstrated planes with a spacing (0.346 nm) that corresponded with the *c*-axis of Hap, in the direction of the long axis of the crystallite (Fig. 3e). Other features in the high-resolution TEM demonstrated Fourier images with an interplanar spacing (0.482 nm) corresponding to magnetite (Fig. 3f).

Selected area electron diffraction (Fig. 3g) demonstrated the presence of magnetite along with Hap in the mHap samples, consistent with the XRD findings. It was possible to find spots in the diffraction pattern from one of the principal orthogonal axes of magnetite aligned along the same direction (i.e., diameter) as the *c*-axis of Hap (note the * and § in Fig. 3g). This was consistent with a coordinated alignment of the magnetite and Hap crystallites.

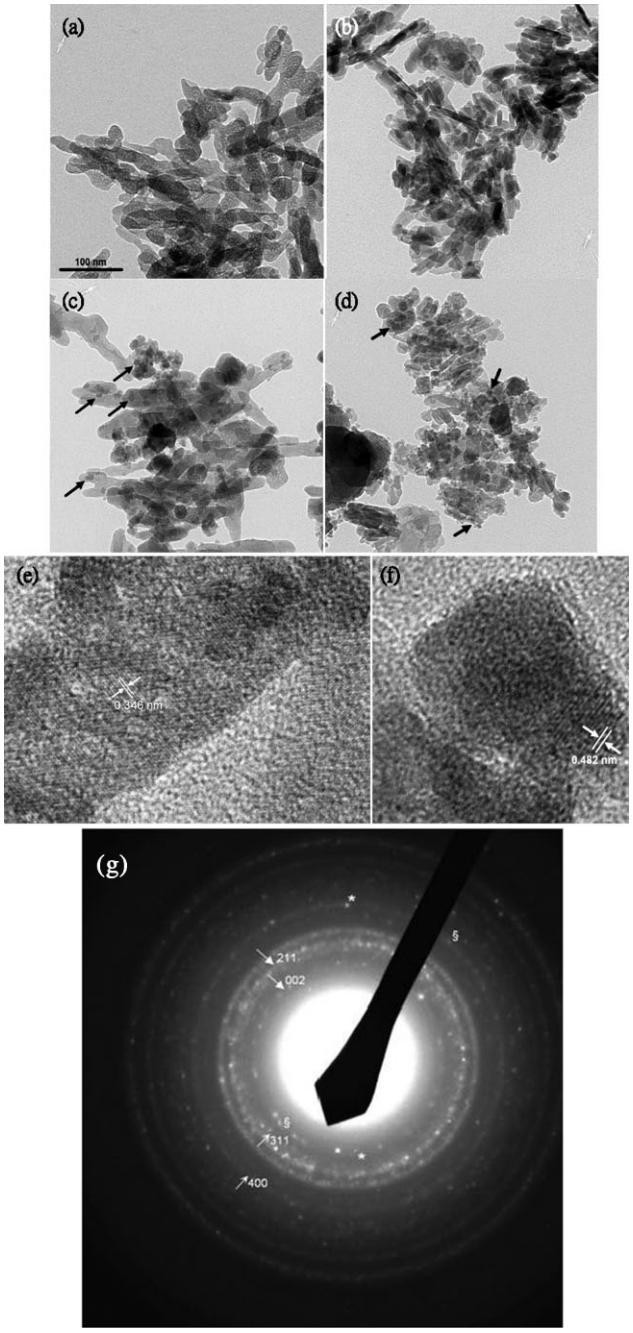

Figure 3. TEM images of a) Hap, b) NBM, c) mHap, and d) mNBM taken at the same magnification. The arrows show the magnetite crystallites in the c) mHap and d) NBM samples. e,f) High-resolution TEM images of a mHAP sample showing interplanar spacings corresponding to e) Hap and f) magnetite. g) Selected area electron diffraction pattern of mHap taken from a region comparable to that in (c). The arrows point out the 002 and 211 reflections from Hap and the 311 and 400 reflections from magnetite. The asterisk (*) and (§) show spots from the *c*-axis (002) of Hap aligned with one of the orthogonal directions of magnetite, consistent with hetero-epitaxial growth.

2.5. pDNA Binding to the Nanoparticles

The Hap NPs adsorbed virtually all of the pDNA from its solutions at the highest NP:pDNA (by weight, wt.) ratio (Table 2). In comparison, about 90% of the pDNA was bound by the NBM NPs at the highest NP:pDNA (by wt.) ratio. As might have been expected, the percentage of pDNA bound by the samples increased with the ratio of NP:pDNA. Two-factor analysis of variance (ANOVA) revealed a significant effect of NP type ($p = 0.0029$; power = 0.94) and NP:pDNA wt. ratio ($p = 0.0003$; power = 0.99) on the amount of plasmid bound to the nonmagnetic NPs. Because the contribution of the iron to the weight of the mNPs could not be established, direct comparison of the binding results for the nonmagnetic and magnetic samples could not be made in such away as to account for differences in particle number and surface area. However, we estimated that the highest NP:pDNA wt. ratio for the mNPs would be comparable with the highest NP:pDNA wt. ratio for the nonmagnetic NPs. Based on this comparison, the percentage of pDNA bound by the Hap and NBM NPs remained about the same after addition of the iron ions to form the magnetic NPs (Table 2). In contrast, the magnetite samples displayed poor affinity for binding pDNA, compared to the Hap and NBM NPs despite the fact that the small size of the magnetite crystallites would have indicated that the number of magnetite particles and their surface area would have been far greater than the mHap and mNBM. Two-factor ANOVA for the mHap and mNBM plasmid binding revealed no significant effect of particle type on plasmid binding ($p = 0.17$) albeit with a low power (0.26), and a significant effect of wt. ratio ($p < 0.001$; power = 0.99).

The pGFP-GDNF (where pGFP is plasmid humanized green fluorescent protein) had specific sequence sites that were cut by the Not I and Xho I restriction enzymes. After this enzymatic digestion, the pGFP-GDNF was degraded completely. The lanes in

Table 2. Percentage of GFP-GDNP pDNA binding to the nanoparticles. Mean ± (standard deviation) $n = 3$.

	NP:pDNA (by wt.)		
	1600/1.5	800/1.5	400/1.5
Hap	97 ± 5	84 ± 13	69 ± 5
NBM	87 ± 11	63 ± 7	43 ± 18
	Iron-Containing NP:pDNA (by wt.)		
	500/1.5	250/1.5	125/1.5
mHap	99 ± 1	46 ± 7	19 ± 4
mNBM	85 ± 6	61 ± 7	7 ± 6
Magnetite	8 ± 2	4 ± 2	0

Table 3. Zeta potential of the NPs.

	Zeta Potential, mV (average of 5 readings, $n = 1$)				
	Hap	mHap	NBM	mNBM	Magnetite
NPs	−10.6	−18.2	−7.0	−18.8	−54.4
pDNA-NPs	−67.7	−53.5	−45.6	−54.3	−50.4

the electrophoretic gels containing the enzyme-treated magnetic and nonmagnetic Hap and NBM NPs to which DNA was bound did not display the bands of the degradation products from the enzyme-treated plasmid, indicating that the enzymes were not able to cleave the plasmid bound to the NPs.

2.6. Zeta Potential

Zeta potential measurements (Table 3) demonstrated that the surface charges of the Hap and NBM NPs were substantially less than that of magnetite. Addition of iron ions to the NPs resulted in more strongly negative charges on the mNPs. Binding of pDNA to the NPs greatly increased the negative charge. Addition of pDNA to the magnetite NPs had no notable effect on its negative charge. However, the poor binding affinity of pDNA for magnetite complicates interpretation of this result. The pDNA-NP complexes appeared to display enough of a surface charge to prevent aggregation of the NPs.

2.7. Transfection Efficiency

Examination of the cultures did not reveal noticeable differences in the number of cells among the various groups. Virtually all of the cells undergoing magnetofection with mHap and mNBM expressed GFP (Fig. 4). In comparison, it was estimated that 60–70% of the cells transfected without magnetofection displayed the green fluorescence reflective of GFP expression. Also of note was the presence of particulate deposits in the cytoplasm of the cells (Fig. 4), consistent in appearance with the NPs. These particles were not seen in the cultures without the NPs.

2.8. Transmission Electron Microscopy of Endocytosis of the Nanoparticles

At the end of the transfection period, TEM of the MSCs treated with the mHap and mNBM and the application of the magnet revealed their endocytosis of the mNPs (Fig. 5a) and the containment of the NPs in phagosomes (Fig. 5b). No such electron-dense features consistent in appearance with the NPs were seen in the TEM images of control cultures. Phagosomes containing numerous NPs, occasionally located in close proximity to the nucleus (Fig. 5c), could be seen at 24 (Fig. 5c,d) and 48 h (Fig. 5e) post-transfection. In some cases the NPs did not appear to be contained within membrane-bound structures within the cell (Fig. 5d).

2.9. GDNF Expression and Effects of Magnetofection

No GDNF was detected in the medium from the nontransfected MSC control cultures. All of the mNP groups demonstrated overexpression and secretion of GDNF at each of the collection periods (Fig. 6). For all of the groups, the rate of production of GDNF decreased after 7 days. For the cultures that were not exposed to

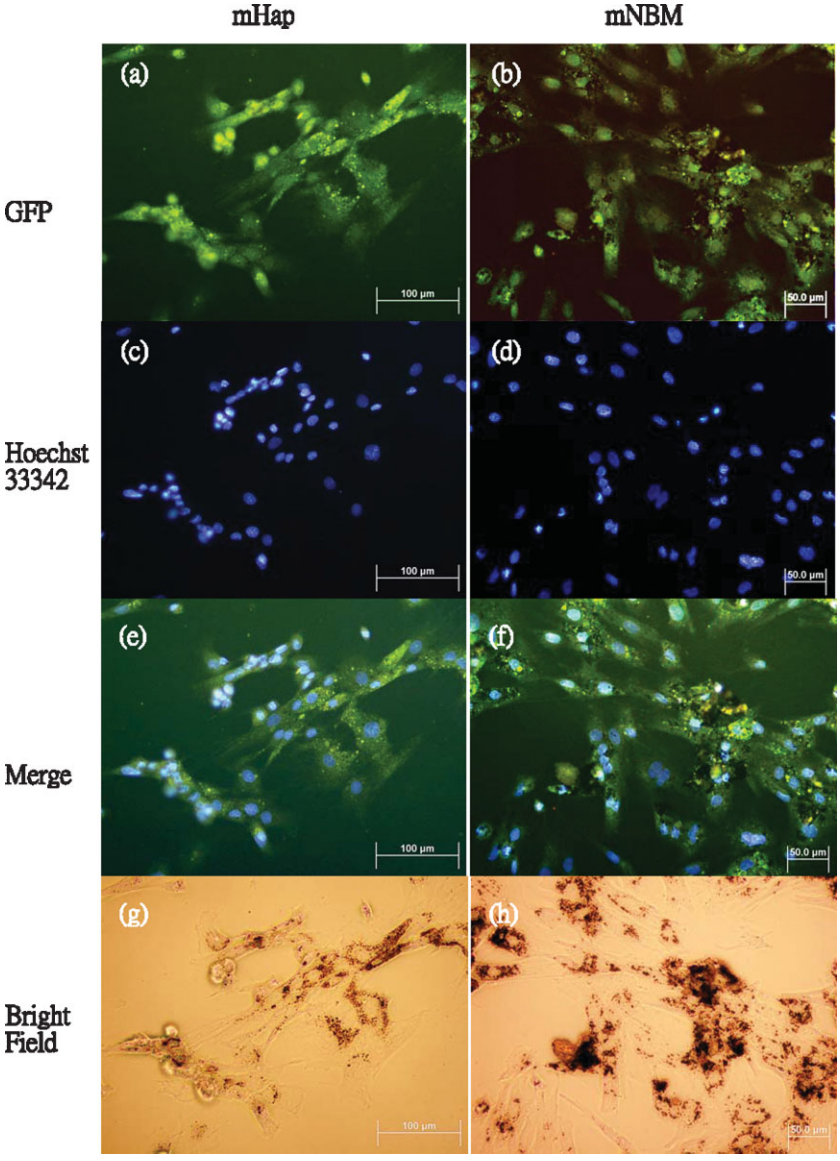

Figure 4. Images of the same fields of view for MSC cultures transfected by pGFP-GDNF mHap (a, c, e, g) and pGFP-GDNF mNBM (b, d, f, h) 6 days post-magnetofection. a–b) Fluorescence images of cultures showing GFP and c–d) cultures stained with Hoechst 33342 nuclear stain. e–f) Merged images for the GFP and nuclear stains and g–h) bright-field images.

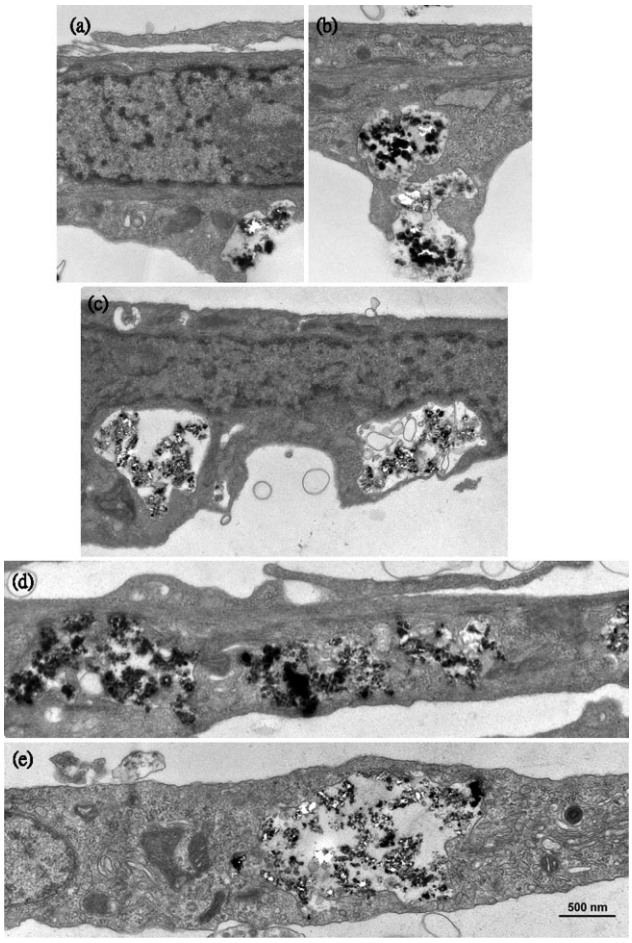

Figure 5. TEM images of MSC cultures treated with mHap NPs and the application of a magnet: a–b) 4, c–d) 24, and e) 48 h after the beginning of the 4-h transfection period.

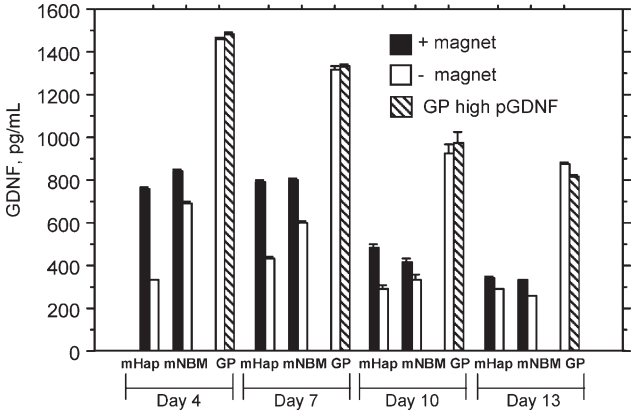

Figure 6. The GDNF in the medium of cultures of MSCs transfected by mHap and mNBM, with and without application of the magnet. Also shown are the GP controls run at the same dose of pGDNF per well (0.625 μg pDNA/well; white bar) and a higher dose (2 μg pDNA/well). Mean ± (standard error of mean); $n = 5$.

magnetofection, the mNBM NPs resulted in substantially higher GDNF expression at the 3-day collection periods ending on days 4 and 7: twofold at 4 days and 37% at 7 days. Of note was that the 15-min application of the magnet significantly increased the expression of GDNF for both mHap and mNBM. For mHap, magnetofection increased GDNF levels: 2.3 times at 4 days, 82% increase at 7 days, and 65% increase at 10 days. For mNBM, the magnetofection had the effect of increasing GDNF by 23% at 4 days, 33% at 7 days, and 22% at 10 days. There was no notable difference in the GDNF expression under the influence of magnetofection for the mHap versus the mNBM NPs at any of the collection periods. The levels of expression in the mNP groups undergoing magnetofection were about 50% of the values measured in the cultures treated with the lipid transfection reagent (Fig. 6). There was no noticeable difference in the GDNF expression in the GenePORTER (GP) groups with the two pGDNF levels (0.625 versus 2 μg/well; Fig. 6).

Three-factor ANOVA revealed the significance of the effects of NP type ($p < 0.0001$; power = 1), magnetofection ($p < 0.0001$; power = 1), and collection period ($p < 0.0001$; power = 1) on the concentration of GDNF in the medium. Fisher's protected least squares differences (PLSD) post-hoc testing demonstrated that the differences in GDNF levels between mHap and mNBM, and between groups with and without magnetofection, were highly significant. All of the collection period comparisons were highly significant except for the comparison of the data from days 4 and 7, which was not significant. One-factor ANOVA of the GDNF data at the 4-day and 7-day periods separately revealed that the GDNF levels for the mNBM NPs with ($p = 0.0002$; power = 1) and without ($p < 0.0001$; power = 1) magnetofection were statistically significantly higher than the respective values for the mHap NPs. For the 3-day collection ending on day 7, only the difference between the mNBM and mHap NPs without magnetofection was statistically significant ($p < 0.0001$; power = 1). Two-factor ANOVA of the GP data demonstrated that there was a significant effect of collection period ($p < 0.0001$; power = 1), but no effect of pGDNF concentration ($p = 0.57$; power = 0.09) on GDNF expression.

The accumulated amount of GDNF for the cultures treated with pGDNF-mNBM NPs without application of the magnetic field, calculated by summing the amounts of GDNF from each of the collection periods, reached about 1.9 ± 0.04 ng mL^{-1} (mean ± standard deviation). This value was 40% higher than that from the cultures treated with the mHap NPs. Application of the magnetic field increased the accumulated GDNF concentration in the mHap cultures from 1.4 ± 0.02 to 2.4 ± 0.07 ng mL^{-1}, for an increase of 70% and in the mNBM cultures from 1.9 ± 0.04 to 2.4 ± 0.06 ng mL^{-1} (26% increase). Two-factor ANOVA revealed significant effects of NP type ($p < 0.0001$; power = 1) and application of the magnet ($p < 0.0001$; power = 1) on the accumulated GDNF. Separate one-factor ANOVA for the data without application of the magnet showed that the difference in GDNF for the mHap and mNBM groups was highly significant ($p < 0.0001$; power = 1). There was no statistically significant difference in the GDNF levels for the mHap and mNBM cultures to which the magnet was applied ($p = 0.7$).

2.10. Lactate Dehydrogenase Cytotoxicity Assay

The lactate dehydrogenase (LDH) assay negative control values from runs on days 1 and 3 were comparable: 0.57 ± 0.02 and

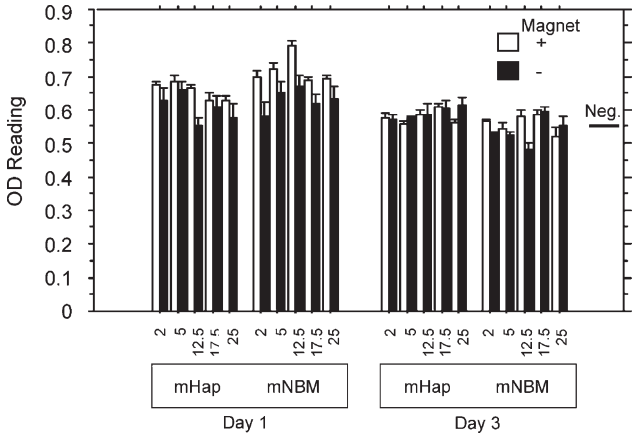

Figure 7. Optical density readings for the LDH assay for cytotoxicity for cultures with and without application of a magnet (mean ± standard error of mean; $n = 5$). The particle doses are in units of mg iron cm^{-2}. The negative control value that is shown is 0.55 ± 0.01 ($n = 10$); the positive control value was 1.1 ± 0.02.

0.54 ± 0.01, respectively. The positive control values from runs on days 1 and 3 were also comparable, and twice the negative control values: 1.13 ± 0.03 and 1.10 ± 0.03. The optical density (OD) readings for the experimental groups after days 1 and 3 were generally comparable, and close to the negative control value (Fig. 7). There were no notable effects of particle type and particle dose on the LDH results, and no difference between groups with and without the magnet. It appeared that there was slightly less LDH released after 3 days compared to the 1-day findings.

Four-factor ANOVA, including all data except for the controls, revealed no significant effects of the particle type ($p = 0.55$; power = 0.09) and dose ($p = 0.29$; power = 0.38) on the LDH release, but there were significant effects of time ($p < 0.0001$; power = 1) and the application of the magnetic field ($p < 0.0001$; power = 1), even though the differences among groups were small. In analyzing the data from days 1 and 3 separately, 3-factor ANOVA demonstrated significant effects of particle type ($p = 0.0003$; power = 0.98), dose ($p = 0.045$; power = 0.7), and application of the magnet ($p < 0.0001$; power = 1) on the LDH release, again even though the differences among groups were small. Three-factor ANOVA of the 3-day data showed significant effects of particle type ($p < 0.0001$; power = 0.99) and dose ($p = 0.002$; power = 0.95), but no effect of the magnet ($p = 0.44$; power = 0.12) on the OD measurements. Combining the results for all doses with the results for the groups with and without the magnet and including the positive and negative controls, 2-factor ANOVA showed that there were significant effects of particle type ($p < 0.0001$; power = 1) and time ($p < 0.0001$; power = 1) on the LDH release. Fisher's PLSD revealed statistically significant differences between the particle groups and the negative controls, even though the particle groups were only slightly higher than the negative controls.

3. Discussion

The notable findings of this work were that NPs comprising synthetic Hap and NBM crystallites could be modified to be made superparamagnetic and that these mNPs displayed enhanced gene transfection when used as non-viral vectors under the action of a magnetic field. Magnetofection resulted in an approximate twofold increase in gene expression through 7 days post-transfection for the mHap NPs. The percentage increase in GDNF expression resulting from the 15-min period under the influence of the magnetic filed was not as high for the mNBM NPs, but significant at the first three collection periods (from 20–30% higher than nonmagnet controls). The enhanced transfection under the action of the magnet may have been due to the effects of: 1) magnetic localization and retention of the NPs at the cell surface; 2) facilitated endocytosis or other process of passage of the NPs through the cell membrane; and/or 3) enhanced release of the plasmid intracellularly. Considering the fact that the magnet was applied for only the first 15-min period that the cells were exposed to the pGDNF-mNP complexes, the first and perhaps second of the above possibilities would seem the most likely explanations for the enhanced transection. Also of note was that the LDH assay showed that there was no cytotoxicity of the mNPs. Additional studies will be required to address the mechanism by which magnetofection enhances gene expression.

The transfection enabled by the nonmagnetic Hap and NBM NPs was not assessed in this study. The binding assays demonstrated that there was comparable adsorption of plasmid DNA on the magnetic and nonmagnetic NPs suggesting that the transfection to be expected of the nonmagnetic Hap and NBM would be comparable to the mHap and mNBM, without magnetofection.

Prior publications have reviewed the benefits of NPs as delivery vehicles for plasmid DNA,[8,9] and the potential benefits of magnetofection[8,41] in: 1) facilitating the entry of the NPs into cells; 2) targeting NPs to selected sites in vivo; and 3) retaining NPs at selected sites. The NPs most often used for magnetofection have been iron oxides: magnetite and maghemite. Prior approaches have been to modify these magnetic NPs to overcome their undesirable properties and to impart specific functionality. This is the first report of the functionality of magnetically modified calcium phosphate NPs, which have certain inherently desirable traits for magnetofection.

Magnetofection, an outgrowth of the magnetic targeting of drugs,[42,43] has several potential benefits for gene delivery using viral and non-viral vectors,[15] including enhancement of the action of vectors up to several hundred times and acceleration of the gene transfection or transduction process. Magnetic-enhanced gene transfection methods are somewhat disadvantaged when reliant on the use of inorganic superparamagnetic NPs such as iron oxides, especially with respect to safety concerns. Iron oxides appear to be well tolerated in some biological assays,[44] but other studies have demonstrated their toxic effect on cells,[19] including their disruption of cytoskeleton organization.[45] Moreover, while iron oxide particles (primarily magnetite and maghemite) have been reported in human brain tissue,[46] it has been proposed[47] that their presence may be associated with senile plaques and tau filaments found in brain tissue affected by neurodegenerative diseases.[48] In addition to the uncertainties regarding the safety profile of iron oxides, as demonstrated in the present study iron oxide particles have a poor binding affinity for DNA. This compelled the development of mNPs to replace iron oxide or at least reduce its amount in mNPs used for magnetofection. The poor binding of DNA by the magnetite NPs in this study obviated the inclusion of a magnetite magnetofection control group. Future

work needs to more fully characterize the DNA binding by magnetite using a range of particle sizes and investigate the associated magnetofection.

While there are questions concerning the intrinsic biocompatibility of magnetic metallic NPs, calcium phosphate NPs are widely commended as non-viral vectors based on their DNA binding affinity, protection of pDNA from enzymatic degradation, favorable safety profile, and biodegradability.[49,50] Of interest in the current experiments was the difference in the GDNF tranfection resulting from the synthetic mHap and natural mNBM NP vectors in cultures without application of the magnet during the transfection period. The mNBM yielded a 40% higher GDNF level, even though there did not appear to be a notable difference in: 1) the transfection efficiency (from the GFP expression); 2) the amount of pDNA bound to each type of NP; and 3) the protective effect of the NP in shielding the DNA from enzymatic degradation. While the ICP-OES did not demonstrate a difference in the Ca:P stoichiometry of the two calcium phosphates, NBM has previously been shown to be a calcium-deficient carbonate apatite.[25–27] This compositional difference along with the difference in crystallite size and shape may have resulted in a more favorable release of the pGDNF intracellularly and facilitated transport into the nucleus. This difference in transfection, between mNBM and mHap NPs, was overcome by the application of the magnetic field.

This is an extension of the first preliminary report[20] of the magnetization of calcium phosphate crystallites comprising NPs. In the present work, preformed Hap and NBM NPs were treated with a solution of iron chloride followed by NH_4OH at 80 °C. The calcium phosphates were rendered superparamagnetic as the result of the formation of magnetite crystallites on the individual Hap and NBM crystallites. The fact that virtually all of the mHap and mNBM NPs were attracted to a magnet indicated that magnetite formed on virtually all of the NPs; the mHap and mNBM products were not simple mixtures of the calcium phosphate NPs and magnetite crystallites. The change in color from white to black of the mHap and mNBM powder was consistent with the presence of magnetite demonstrated by XRD. Also of note was the comparison of the SQUID saturation magnetization values of $\approx$30 emu g^{-1} for the mHap and mNBM NPs with the value of $\approx$40 emu g^{-1} reported in a prior study for magnetite.[51] The absence of hysteresis in the curve of magnetization versus external magnetic field for mHap and mNBM demonstrated that the NPs had no remanence and coercivity,[52] reflecting the fact that there was no long-range magnetic dipole–dipole interactions among the particles, and thus indicated superparamagnetic behavior. That the magnetization of mHap and mNBM NPs did not saturate at 50 KOe was also consistent with superparamagnetic behavior.

The initial goal of the current study was to attempt to replace iron oxide for magnetofection with calcium phosphate NPs rendered magnetic by the addition of iron ions. Instead of achieving this goal, we produced calcium phosphate NPs with adherent magnetite crystallites. While falling short of our objective, the mHap and mNBM NPs do provide improved pDNA binding and the benefits of the properties of the Hap and NBM, and importantly reduce the amount of iron oxide that would be introduced into the body.

TEM revealed crystallites consistent in size with magnetite ($\approx$9 nm in diameter[51]) on the surfaces of the plate-like Hap and NBM crystallites. Prior studies have demonstrated that apatite plates result from the preferential growth in the *a*–*c* crystallographic plane.[40,53] The cubic magnetite crystallites with their *a* lattice parameter of 0.84 nm thus appeared to grow from the plane of apatite with rectangular symmetry, with *a* and *c* lattice dimensions of 0.94 and 0.69 nm, respectively. This may be a case of hetero-epitaxy in which one crystalline phase, in this case magnetite, grows from the surface of a crystal of different composition,[54] i.e., apatite. For hetero-epitaxy to occur the mismatch in the lattice parameters of the two crystals at the interfacial plane should be 15% or less.[54] In the present case, the mismatch in the magnetite and apatite lattice parameters are 12% (Hap *a* axis versus magnetite *a* axis) and 18% (Hap *c* axis versus magnetite *c* axis), close to the normally accepted criterion for hetero-epitaxy. Of note is how close the 100 interplanar spacings are for the Hap and magnetite: 0.82 versus 0.84 nm, respectively. It was also interesting to find spots in the selected area electron diffraction pattern of mHap that corresponded with the principal orthogonal axis of magnetite aligned in the same direction as the *c*-axis of Hap, also consistent with hetero-epitaxy.

The two-week accumulated levels of GDNF of about 2 ng mL^{-1} in the magnetofection cultures with the mHap and mNBM NPs containing as little as 0.6 μg plasmid/well in 24-well plates compared with values of approximately twice that value for the same amount of plasmid incorporated into a commercially available lipid transfection reagent. Of importance is that the level of GDNF expression by rat MSCs following magnetofection was high enough to result in GDNF concentrations which were found to be close to therapeutic concentrations in previous in vitro investigations: 1 ng mL^{-1} increased by nearly 100% the number of trigeminal ganglion sensory neurons in culture at 5 days post-plating;[55] and 10 ng mL^{-1} nearly doubled dopamine neuron survival and reduced the rate of apoptosis from 6 to 3% in human embryonic dopamine neurons cultures.[56] Future in vivo studies will be necessary to determine if magnetofection using magnetized calcium phosphate NPs will be capable of inducing expression of therapeutic GDNF doses locally.

While lipid transfection agents may result in higher expression levels in vitro, there remain concerns regarding their safety profile.[8,57] Moreover, an unfavorable ''serum effect'' on DNA-lipid transfection, which has been well documented,[58,59] explains the dramatic reduction in transfection in vivo, compared to in vitro transfection of cells with lipolpex in serum-free medium.[58] In comparison, calcium phosphate NP non-viral vectors have been shown to have ''appreciable serum tolerability''[60] and to enhance transfection when administered in vivo.[61] It will be helpful in future studies to evaluate the in vitro transfection efficiencies of the mHap and mNBM NPs in the presence of increasing amounts of serum supplementing the medium. Such results will be important in providing an indication of the potential effectiveness of the non-viral vectors in vivo.

4. Conclusions

Synthetic Hap and NBM crystallites can be rendered magnetic by the hetero-epitaxial growth of magnetite, and these mHap and mNBM NPs result in elevated transfection of MSCs in vitro under the action of a magnet. Superparamagnetic Hap and NBM NPs have the potential to serve as non-viral vectors for the delivery of

genes to select sites in the brain. When the mNPs are injected systemically, application of an external magnet may facilitate the movement of particles across the blood–brain barrier.[13] For both systemic administration of the mNPs and direct injection into the brain, the mNPs may be retained at a selected site by a magnet, and the action of the magnet may also facilitate transfection in vivo. mHap and mNBM NPs can also serve as safe and effective non-viral vectors for the transfection of cells ex vivo using magnetofection, for subsequent cell therapy.

5. Experimental

Preparation of Synthetic Hydroxyapatite Nanoparticles, and Magnetic Hydroxyapatite and Natural Bone Mineral Nanoparticles: Hap crystallites were prepared by the precipitation method previously described [20]. In brief, orthophosphoric acid solution was added into dispersed calcium hydroxide suspension at a rate of 1.5 mL min^{-1} and aged for 20 h. The entire process was carried out at 80 °C in a hot water bath. The final Ca:P ratio was 1.67 to match the stoichiometric ratio in Hap. The pH value was adjusted to 8 by the addition of NH_4OH during the precipitation process. The term, ''nanoparticles,'' was adopted to describe the crystallite aggregates, which were from tens to hundreds of nanometers in diameter.

Iron(II) chloride solution was added to the dispersed suspensions of the Hap and NBM (anorganic bovine bone, Geistlich Biomaterials, Wolhusen, Switzerland) NPs, at a rate of 1.5 mL min^{-1}. The pH value was again adjusted to 8 by adding NH_4OH at 80 °C, and the suspension aged for another 10 h at 80 °C. Subsequently, the precipitates were washed with deionized water three times. Finally, the aqueous suspensions were freeze-dried to form a dispersible powder. As a control, magnetite was precipitated from the iron chloride solution by adjusting the pH to 8 using NH_4OH at 80 °C, and the suspension aged for another 10 h at 80 °C.

Composition, Structure, and Magnetic Properties of the Nano- particles: The calcium, phosphorous, and iron content of the NPs ($n = 3$) was determined by ICP-OES (ACTIVA, HORIBA Jobin Yvon Inc., Edison, NJ). The crystalline structure of the NPs was analyzed using XRD (Rigaku RU300, Rigaku, Inc., The Woodlands, TX) in the range from 10 to 70° 2θ (using a Cu Kα source). The identity of the peaks in the XRD patterns was determined by comparison with the reference profiles in the JCPDS. The lattice constants and size of the crystallites making up the NPs was calculated from the XRD data using Jade software (Jade Software Corp., Atlanta, GA).

The morphology of the NPs was observed by SEM. Hap and NBM NPs were deposited from solutions with various NP concentrations onto glass slides and allowed to air dry. The slides were mounted on SEM stubs and coated with gold palladium, and examined in a scanning electron microscope (JEOL JSM-5910, JEOL Ltd., Tokyo, Japan). For ultrastructural studies, NP samples were deposited on carbon-coated copper grids from aqueous solution and air-dried. The grids were examined by TEM (JEOL 200CX, JEOL Ltd.). Selected area electron diffraction was also performed. The lattice fringes (Fourier images) of mHap NPs were examined using a high-resolution transmission electron microscope (JEOL 2011, JEOL Ltd., Tokyo, Japan).

The particle size of the NPs was determined from DLS measurements using an argon laser light scattering system at the wavelength of 514 nm (BI-200SM, Brookhaven Instruments Corporation, Holtsville, NY). DLS utilizes time-dependent fluctuation in the scattering intensity of NPs undergoing Brownian motion to determine the size distribution profile of the NPs in water. In brief, NPs were suspended homogeneously in water in a cuvette. The measurement was detected by a photodetector at 90° scattering angle. The averaged particle sizes were obtained by repeating the measurements five times ($n = 5$).

The magnetic properties of the mNPs were analyzed by a SQUID (Quantum Design MPMS-5S, Quantum Design, SanDiego, CA) in an applied magnetic field of ± 50 kOe (Oersted units of magnetic energy) at 300 K (room temperature). The SQUID is a magnetometer able to measure small magnetic fields. The mass magnetization is defined as the magnetic moment per total mass of sample (in electromagnetic units, emu, per gram) measured as the samples are exposed to a changing magnetic field.

Preparation of Plasmid DNA–Nanoparticle Transfection Complexes: The plasmid encoding rat GDNF (pGDNF) was obtained from Children's Memorial Hospital, Chicago, IL. This is an adeno-associated viral shuttle plasmid containing a bicistronic expression cassette of rat GDNF and humanized GFP genes joined by an internal ribosome entry site under the control of a cytomegalovirus promoter and flanked by inverted terminal repeats. The pDNA was amplified in competent Escherichia coli (DH5 from Invitrogen, Carlsbad, CA) and isolated from the bacteria using the Mega QIAfilterTM Plasmid kit (Qiagen, Valenica, CA).

The pDNA was mixed into a dispersion of the nonmagnetic and magnetic Hap and NBM NPs, and magnetite NPs, at 3 different weight ratios ($n = 3$), and incubated for 15 min in order to allow DNA to bind to NPs to form pDNA-NP transfection complexes. The mNPs were removed from the suspension by attraction to a neodymium iron boron magnet (LifeSep MX, Dexter Magnetic Technologies Inc., Chelmsford, MA). The suspensions of nonmagnetic Hap and NBM complexes incorporating the pDNA were separated by centrifugation. The sediment was washed with Tris–EDTA buffer twice. The supernatant of the dispersions was analyzed by agarose gel (0.8%) electrophoresis, and the amount of DNA remaining in the supernatant was quantified using TotolLab software (Nonlinear Dynamics, Durham, NC). This DNA remaining in the solution was subtracted from the initial amount for the calculation of the percentage of pDNA bound to the NPs.

In order to determine if the complexation of the pDNA to the NPs had a protective effect against the action of restriction enzymes, samples of the pDNA complexes with the magnetic and nonmagnetic Hap and NBM NPs, prepared as described above, were treated by restriction enzyme (Not I and Xho I) digestion for 1 h. Samples of pDNA-magnetite were also treated. The pDNA-NP complexes were suspended in NEBuffer 3 (New England Biolabs, Ipswich, MA) containing bovine serum albumin (BSA; New England Biolabs) and treated with restriction enzymes (Not I and Xho I; New England Biolabs) for 1 h digestion at 37 °C. The enzyme-treated complexes were loaded into the wells of the agarose gel electrophoresis apparatus, along with a ladder and nontreated and restriction enzyme-treated pGFP-GDNF plasmid.

Zeta-Potential: Measurements of the zeta potential of the NPs were obtained using the ZetaPALS apparatus (Brookhaven Instruments Corporation, Holtsville, NY) which utilizes phase analysis light scattering to determine the electrophoretic mobility of charged, colloidal suspensions. In brief, equal volumes of pDNA (25 μg mL^{-1}) and magnetic NPs (1 mg iron mL^{-1}) were incubated together for 15 min to form a transfection complex (400:1 wt. ratio). For the nonmagnetic NPs, 40 μg mL^{-1} of pDNA was added to a suspension of 1.6 mg mL^{-1} of the NPs (400:1 wt. ratio).

NPs in aqueous solution (1.5 mL; with or without pDNA; $n = 1$) were suspended in the cuvette for analysis. An average value for the zeta potential was obtained from five automatically repeated measurements. The zeta potential measurement can be affected by the stability of the particles in suspension. Electrostatic repulsion of adjacent particles reduces the tendency for aggregation. The more negative or positive the zeta potential, the greater the electrical stabilization of NPs in the solution.

Cell Culture and Transfection: Rat MSCs were harvested from both the femurs and tibiae of 6 young Lewis rats (<6 weeks old) as previously described [62]. The cells from the 6 rats were cultured separately throughout the experiment. A cell suspension was filtered through a 40-μm cell strainer, centrifuged at 1500 rpm for 10 min, resuspended in phosphate buffered saline (PBS), and then centrifuged a second time at 1500 rpm for 10 min. Cells were resuspended in ''expansion medium'' containing low-glucose Dulbecco's modified Eagle medium (lg-DMEM; GIBCO, Cat#11885-084, Carlsbad, CA), 20% fetal bovine serum (FBS; Hyclone Technologies, Logan, UT), and 1% penicillin/streptomycin. Primary cells (passage 0; P0) were plated onto 75-cm^2 flasks and incubated at 37 °C and 5% carbon dioxide. Nonadherent cells were removed at the medium change after 48 h. At approximately 90% confluence, cells were detached, resuspended, and subcultured to P1 before being frozen at −80 °C. Upon thawing, cells were plated in 150-cm^2 flasks at 5000 cells/cm^2 and grown in the expansion medium. Rat MSCs similarly prepared in

our laboratory have been induced to differentiate into neuronal cells expressing β-tubulin, nestin, and glial fibrillary acidic protein and into chondrocytes, in neurogenic and chondrogenic media, respectively.

Transfection with Magnetic Nanoparticles: For transfection, equal volumes of pDNA (25 μg mL^{-1}) and magnetic NPs (1 mg iron mL^{-1}) were mixed together and allowed to set for 15 min to form transfection complexes. 3.2×10^4 MSCs of P 2–4 were cultured in 24-well (2 cm^2) culture plates and grown in 1 mL of expansion medium. After 24 h of culture, the medium in the wells was replaced with 250 μL serum-free medium containing the transfection complexes (0.625 μg pDNA/well), for the 4-h transfection period. Magnetofection was performed by applying a magnetic field during the first 15-min stage of the 4-h transfection period. A neodymium iron boron magnet (LifeSep 96F; force density 5.6 T^2 m^{-1} and field gradient 32.5 T m^{-1}; Dexter Magnetic Technologies Inc.) was placed under the culture dish. After the 4-h transfection period, 250 μL of expansion medium was added to each well, and the dishes incubated for an additional 24 h. The supernatant was then replaced with fresh expansion medium.

In other cultures, the transfection complex (0.625 μg pDNA/well) was incubated with MSCs (6.5×10^4 cells/well) in 4 chamber slides (Nunc Lab-Tek II Chamber Slide System, Thermo Fisher Scientific, Rochester, NY) for the investigation of transfection efficiency under fluorescence microscopy. Six days after transfection, the expression of GFP in the groups with the mHap and mNBM complexes was visualized by fluorescence microscopy. The percentage of cells expressing GFP, i.e., transfected, was obtained by dividing the number of fluorescent cells by the total number of cells revealed by nuclear staining with Hoechst 33342 dye (H1399, Invitrogen, Carlsbad, CA). Bright field microscopy images of the same regions were also taken to reveal the total number of cells in the field of view.

Selected mHap and mNBM cultures undergoing magnetofection, and MSC control cultures with no NPs, were prepared for TEM. MSCs were grown in 6-cm diameter (22 cm^2) culture dishes (BD Falcon, Cat. # 353002, Franklin, Lakes, NJ). The dishes were seeded with 5×10^5 cells/dish, and 0.55 mg mHap and mNBM NPs containing 10 μg pDNA/dish, were added to the dishes. Magnetofection was carried out under the same conditions described above. The cultures were terminated: 1) immediately after the 4-h transfection period, 2) 24 h after the start of the transfection period, and 3) 48 h after the start of the transfection period.

Transfection with a Lipid Transfection Reagent: A commercially available lipid transfection reagent was employed as a control for comparison with the mNPs: GenePORTER 2 transfection assay (Genlantis, Inc., San Diego, CA) containing polyvalent, cationic lipids. The GenePORTER 2 lipid film was hydrated by 1.5 mL hydration buffer at room temperature, and vortexed for 10 s. 1 μg pDNA was diluted by 25 μL of the ''DNA diluent B'' in the GenePORTER 2 kit, and mixed well by pipetting for 5 min at room temperature. Then, the diluted DNA was added into the same volume of GenePORTER 2 reagent (3.5 μL) diluted with serum-free medium, and the mixture was allowed to stand for 5 min at room temperature. MSCs (3.2×10^4, P2–P4) cells were cultured in 24-well (2 cm^2) culture plates and grown in 1 mL of expansion medium. After 24 h of culture, the medium in the wells was replaced with 250 μL serum-free medium containing the transfection complexes at one of two doses (0.625 and 2 μg pDNA/well; $n = 5$). After the 4-h transfection period, 250 μL of expansion medium was added to each well, and the dishes incubated for 24 h. The supernatant was then replaced with fresh expansion medium.

Evaluation of GDNF in the Culture Medium: Twenty-four hours post-transfection, the culture medium was refreshed, and the medium collected every 3 days thereafter at medium changes on (at days 4, 7, 10, and 13; $n = 5$) for enzyme-linked immunosorbent assay (ELISA, Human GDNF DuoSet, R&D Systems, Minneapolis, MN). In brief, the diluted capture antibody was incubated in 96-well microplates overnight. The nonspecific blocking was then reacted for 1.5 h, and the aliquot of medium added into microplate wells for 2 h. The recombinant human GDNF was serially diluted as a positive control in order to determine the appropriate detection range. Medium from the group of cells without transfection was used as the negative control. The biotinylated goat anti-human GDNF was incubated 2 h for detection and then conjugated with streptavidin-HRP for 20 min. All reactions were performed at room temperature. Tetramethylbenzidine (TEB) solution was used for staining. The reaction was stopped by the addition of 2 N sulfuric acid. The results were measured at the wavelength of 450 nm by spectrophotometer (PerkinElmer Wallac 1420 Victor 2; Perkin Elmer Life Sciences, Waltham, MA).

Transmission Electron Microscopy of Transfected Cells: The cells in culture were fixed in 2.5% glutaraldehyde and 3% paraformaldehyde with 5% sucrose in 0.1 M sodium cacodylate buffer (pH 7.4), and postfixed in 1% osmium in veronal-acetate buffer. The tissue was stained in block overnight with 0.5% uranyl acetate in veronal–acetate buffer (pH 6.0), and then dehydrated and embedded in Spurrs resin. Blocks were sectioned with a Leica ultracut UCT ultramicrotome with a Diatome knife. Sections were stained with 2% uranyl acetate, and lead citrate.

Lactate Dehydrogenase Cytotoxicity Assay: A LDH assay was used to evaluate cell damage (i.e., cytotoxicity) induced by the mNPs. LDH is a stable cytosolic enzyme from mitochondria that is released from the cell when it is lyzed. Each well of a 96-well culture plate was seeded with 10^4 MSCs. The cells were cultured in expansion medium (200 μL/well). After 24 h of culture, the medium in the wells was replaced with serum-free medium (100 μL/well) containing mHap and mNBM NPs at the following ''doses'' ($n = 5$) for the 4-h period incubation period, with or without an applied magnetic field during the first 15 min: 0.64, 1.6, 4, 5.6, and 8 μg iron/well (corresponding to 2, 5, 12.5, 17.5, and 25 μg iron/cm^2, respectively). After 4 h, 100 μL of expansion medium was added to each well, and the cells incubated for an additional 24 h period. The supernatant was then replaced with fresh expansion medium. The cultures were terminated after 1 and 3 days ($n = 5$). LDH was measured by a commercial assay kit (CytoTox 96 Non-Radioactive Cytotoxicity Assay, Promega, Madison, WI).

In the assay, LDH released in the cultures was measured with the 30-min coupled enzymatic assay. LDH catalyzes the conversion of metabolized lactate to pyruvate in the presence of nicotinamide adenine dinucleotide (NAD). The nicotinamide adenine dinucleotide hydrate (NADH) which is formed reduces the tetrazolium salt to a formazan product (red in color). The intensity of the red color from the formazan product is proportional to the number of lysed cells. In brief, 50 μL of medium was transferred to a new enzymatic assay plate with 50 μL of LDH substrate solution. Then, 50 μL of a ''stop solution'' was added to each well in the plate, and the OD values read in a spectrophotometer (PerkinElmer Wallac 1420 Victor 2; Perkin Elmer Life Sciences, Waltham, MA) at a wavelength of 490 nm. The positive control ($n = 5$) was the maximum absorption value of cells incubated with medium containing 1% Triton X-100 (T8787, Sigma–Aldrich, St. Louis, MO); the negative control ($n = 5$) was the mean spontaneous absorption of cells incubated with medium. The positive and negative control assays were performed along with the experimental groups both on days 1 and 3.

Statistical Analysis: All data are expressed as mean ± standard error of the mean unless otherwise indicated. The significance of the effect of selected parameters on the outcome variables was analyzed by multifactor analysis of variance (ANOVA). Group comparisons were made by Fisher's PLSD. Statistical significance was accepted at a level of $p < 0.05$.

Acknowledgements

Funding for this work was provided by the Department of Veterans Affairs and the Department of Defense. H.C. Wu also acknowledges the graduate student study abroad program (GSSAP) of the National Science Council of Taiwan and a scholarship from the College of Engineering of the National Taiwan University. M. Spector is a Veterans Affairs Research Career Scientist. The technical assistance of Alix Weaver is gratefully acknowledged.

Received: June 23, 2009
Published online:

[1] J. Kreuter, *Pharm. Acta Helv.* **1978**, *53*, 33.
[2] J. J. Marty, R. C. Oppenheim, P. Speiser, *Pharm. Acta Helv.* **1978**, *53*, 17.
[3] M. G. Cascone, L. Lazzeri, C. Carmignani, Z. Zhu, *J. Mater. Sci.* **2002**, *13*, 523.

[4] S. Parveen, S. K. Sahoo, *J. Drug Targeting* **2008**, *16*, 108.
[5] F. Alexis, J. W. Rhee, J. P. Richie, A. F. Radovic-Moreno, R. Langer, O. C. Farokhzad, *Urol. Oncol.* **2008**, *26*, 74.
[6] K. Cho, X. Wang, S. Nie, Z. G. Chen, D. M. Shin, *Clin. Cancer Res.* **2008**, *14*, 1310.
[7] V. Vijayanathan, T. Thomas, T. J. Thomas, *Biochemistry* **2002**, *41*, 14085.
[8] A. Ragusa, I. Garcia, S. Penades, *IEEE Trans. Nanobiosci.* **2007**, *6*, 319.
[9] V. Sokolova, M. Epple, *Angew. Chem. Int. Ed.* **2008**, *47*, 1382.
[10] H. Cohen, R. J. Levy, J. Gao, I. Fishbein, V. Kousaev, S. Sosnowski, S. Slomkowski, G. Golomb, *Gene Ther.* **2000**, *7*, 1896.
[11] W. H. De Jong, P. J. Borm, *Int. J. Nanomed.* **2008**, *3*, 133.
[12] G. Tosi, L. Costantino, B. Ruozi, F. Forni, M. A. Vandelli, *Exp. Opin. Drug Delivery* **2008**, *5*, 155.
[13] B. Chertok, B. A. Moffat, A. E. David, F. Yu, C. Bergemann, B. D. Ross, V. C. Yang, *Biomaterials* **2008**, *29*, 487.
[14] J. D. Duran, J. L. Arias, V. Gallardo, A. V. Delgado, *J. Pharm. Sci.* **2008**, *97*, 2948.
[15] F. Scherer, M. Anton, U. Schillinger, J. Henke, C. Bergemann, A. Kruger, B. Gansbacher, C. Plank, *Gene Ther.* **2002**, *9*, 102.
[16] K. J. Widder, R. M. Morris, G. A. Poore, D. P. Howard, A. E. Senyei, *Eur. J. Cancer Clin. Oncol.* **1983**, *19*, 135.
[17] C. Alexiou, R. Jurgons, R. J. Schmid, C. Bergemann, J. Henke, W. Erhardt, E. Huenges, F. Parak, *J. Drug Targeting* **2003**, *11*, 139.
[18] G. R. Reddy, M. S. Bhojani, P. McConville, J. Moody, B. A. Moffat, D. E. Hall, G. Kim, Y. E. Koo, M. J. Woolliscroft, J. V. Sugai, T. D. Johnson, M. A. Philbert, R. Kopelman, A. Rehemtulla, B. D. Ross, *Clin. Cancer Res.* **2006**, *12*, 6677.
[19] N. Lewinski, V. Colvin, R. Drezek, *Small* **2008**, *4*, 26.
[20] H. C. Wu, T. W. Wang, J. S. Sun, W. H. Wang, F. H. Lin, *Nanotechnology* **2007**, *18*, 9.
[21] P. N. Kumta, C. Sfeir, D. H. Lee, D. Olton, D. Choi, *Acta Biomater.* **2005**, *1*, 65.
[22] T. Matsumoto, M. Okazaki, M. Inoue, S. Yamaguchi, T. Kusunose, T. Toyonaga, Y. Hamada, J. Takahashi, *Biomaterials* **2004**, *25*, 3807.
[23] D. Olton, J. Li, M. E. Wilson, T. Rogers, J. Close, L. Huang, P. N. Kumta, C. Sfeir, *Biomaterials* **2007**, *28*, 1267.
[24] S. H. Zhu, B. Y. Huang, K. C. Zhou, S. P. Huang, F. Liu, Y. M. Li, G. Xue, Z. G. Long, *J. Nanopart. Res.* **2004**, *6*, 307.
[25] R. Legros, N. Balmain, G. Bonel, *Calcified Tissue Int.* **1987**, *41*, 137.
[26] J. L. Holden, J. G. Clement, P. P. Phakey, *J. Bone Miner. Res.* **1995**, *10*, 1400.
[27] S. V. Dorozhkin, M. Epple, *Angew. Chem. Int. Ed.* **2002**, *41*, 3130.
[28] H. Sariola, M. Saarma, *J. Cell Sci.* **2003**, *116*, 3855.
[29] L. F. Lin, D. H. Doherty, J. D. Lile, S. Bektesh, F. Collins, *Science* **1993**, *260*, 1130.
[30] J. Engele, D. Schubert, M. C. Bohn, *J. Neurosci. Res.* **1991**, *30*, 359.
[31] C. E. Henderson, H. S. Phillips, R. A. Pollock, A. M. Davies, C. Lemeulle, M. Armanini, L. Simmons, B. Moffet, R. A. Vandlen, L. C. Simpson, *Science* **1994**, *266*, 1062.
[32] E. Arenas, M. Trupp, P. Akerud, C. F. Ibanez, *Neuron* **1995**, *15*, 1465.
[33] J. H. Kordower, M. E. Emborg, J. Bloch, S. Y. Ma, Y. Chu, L. Leventhal, J. McBride, E. Y. Chen, S. Palfi, B. Z. Roitberg, W. D. Brown, J. E. Holden, R. Pyzalski, M. D. Taylor, P. Carvey, Z. Ling, D. Trono, P. Hantraye, N. Deglon, P. Aebischer, *Science* **2000**, *290*, 767.
[34] D. L. Choi-Lundberg, Q. Lin, Y. N. Chang, Y. L. Chiang, C. M. Hay, H. Mohajeri, B. L. Davidson, M. C. Bohn, *Science* **1997**, *275*, 838.
[35] D. Kirik, B. Georgievska, A. Bjorklund, *Nat. Neurosci.* **2004**, *7*, 105.
[36] M. H. Mohajeri, D. A. Figlewicz, M. C. Bohn, *Human Gene Therapy* **1999**, *10*, 1853.
[37] L. J. Wang, Y. Y. Lu, S. Muramatsu, K. Ikeguchi, K. Fujimoto, T. Okada, H. Mizukami, T. Matsushita, Y. Hanazono, A. Kume, T. Nagatsu, K. Ozawa, I. Nakano, *J. Neurosci.* **2002**, *22*, 6920.
[38] A. E. Lang, S. Gill, N. K. Patel, A. Lozano, J. G. Nutt, R. Penn, D. J. Brooks, G. Hotton, E. Moro, P. Heywood, M. A. Brodsky, K. Burchiel, P. Kelly, A. Dalvi, B. Scott, M. Stacy, D. Turner, V. G. Wooten, W. J. Elias, E. R. Laws, V. Dhawan, A. J. Stoessl, J. Matcham, R. J. Coffey, M. Traub, *Ann. Neurol.* **2006**, *59*, 459.
[39] J. T. Slevin, D. M. Gash, C. D. Smith, G. A. Gerhardt, R. Kryscio, H. Chebrolu, A. Walton, R. Wagner, A. B. Young, *Neurosurg. Focus* **2006**, *20*, E1.
[40] V. Benezra Rosen, L. W. Hobbs, M. Spector, *Biomaterials* **2001**, *23*, 921.
[41] C. Plank, U. Schillinger, F. Scherer, C. Bergemann, J. S. Remy, F. Krotz, M. Anton, J. Lausier, J. Rosenecker, *Biol. Chem.* **2003**, *384*, 737.
[42] K. J. Widder, A. E. Senyel, G. D. Scarpelli, *Proc. Soc. Exper. Biol. Med. Soc. Exper. Biol. Med.* **1978**, *158*, 141.
[43] A. S. Lubbe, C. Bergemann, W. Huhnt, T. Fricke, H. Riess, J. W. Brock, D. Huhn, *Cancer Res.* **1996**, *56*, 4694.
[44] S. M. Hussain, K. L. Hess, J. M. Gearhart, K. T. Geiss, J. J. Schlager, *Toxicol. in Vitro* **2005**, *19*, 975.
[45] A. K. Gupta, M. Gupta, *Biomaterials* **2005**, *26*, 1565.
[46] J. L. Kirschvink, A. Kobayashi-Kirschvink, B. J. Woodford, *Proc. Natl. Acad. Sci. USA* **1992**, *89*, 7683.
[47] J. Dobson, *FEBS Lett.* **2001**, *496*, 1.
[48] D. Hautot, Q. A. Pankhurst, N. Khan, J. Dobson, *Proc. Biol. Sci.* **2003**, *270* (Suppl. 1), S62.
[49] S. Bisht, G. Bhakta, S. Mitra, A. Maitra, *Int. J. Pharm.* **2005**, *288*, 157.
[50] A. Maitra, *Expert. Rev. Mol. Diagn.* **2005**, *5*, 893.
[51] F. Y. Cheng, C. H. Su, Y. S. Yang, C. S. Yeh, C. Y. Tsai, C. L. Wu, M. T. Wu, D. B. Shieh, *Biomaterials* **2005**, *26*, 729.
[52] U. Jeong, X. W. Teng, Y. Wang, H. Yang, Y. N. Xia, *Adv. Mater.* **2007**, *19*, 33.
[53] M. Spector, *J. Microsc.* **1975**, *103*, 55.
[54] R. J. Stokes, D. F. Evans, *Fundamentals of Interfacial Engineering*, Wiley-VCH, Weinheim, Germany **1996**.
[55] T. J. Price, M. D. Louria, D. Candelario-Soto, G. O. Dussor, N. A. Jeske, A. M. Patwardhan, A. Diogenes, A. A. Trott, K. M. Hargreaves, C. M. Flores, *BMC Neurosci.* **2005**, *6*, 4.
[56] E. D. Clarkson, W. M. Zawada, C. R. Freed, *Cell Tissue Res.* **1997**, *289*, 207.
[57] C. R. Dass, *J. Pharm. Pharmacol.* **2002**, *54*, 593.
[58] S. Li, L. Huang, *Gene Ther.* **2000**, *7*, 31.
[59] G. Nchinda, K. Uberla, O. Zschornig, *BMC Biotechnol.* **2002**, *2*, 12.
[60] Y. Kakizawa, S. Furukawa, A. Ishii, K. Kataoka, *J. Controlled Release* **2006**, *111*, 368.
[61] I. Roy, S. Mitra, A. Maitra, S. Mozumdar, *Int. J. Pharm.* **2003**, *250*, 25.
[62] C. Bolliet, M. C. Bohn, M. Spector, *Tissue Eng.* **2008**, *14*, 207.